Fragile topology protected by inversion symmetry: Diagnosis, bulk-boundary correspondence, and Wilson loop

Yoonseok Hwang, Junyeong Ahn, and Bohm-Jung Yang[*]

Department of Physics and Astronomy, Seoul National University, Seoul 08826, Korea;
Center for Correlated Electron Systems, Institute for Basic Science (IBS), Seoul 08826, Korea;
and Center for Theoretical Physics (CTP), Seoul National University, Seoul 08826, Korea

We study the bulk and boundary properties of fragile topological insulators (TIs) protected by inversion symmetry, mostly focusing on the class A of the Altland-Zirnbauer classification. First, we propose an efficient method for diagnosing fragile band topology by using the symmetry data in momentum space. Using this method, we show that among all the possible parity configurations of inversion-symmetric insulators, at least 17% of them have fragile topology in two dimensions while fragile TIs are less than 3% in three dimensions. Second, we study the bulk-boundary correspondence of fragile TIs protected by inversion symmetry. In particular, we generalize the notion of d-dimensional (dD) kth-order TIs, which is normally defined for $0 < k \leqslant d$, to the cases with $k > d$, and show that they all have fragile topology. In terms of the Dirac Hamiltonian, a dD kth-order TI has $(k-1)$ boundary mass terms. We show that a minimal fragile TI with the filling anomaly can be considered as the dD $(d+1)$th-order TI, and all the other dD kth-order TIs with $k > (d+1)$ can be constructed by stacking dD $(d+1)$th-order TIs. Although dD $(d+1)$th-order TIs have no in-gap states, the boundary mass terms carry an odd winding number along the boundary, which induces localized charges on the boundary at the positions where the boundary mass terms change abruptly. In the cases with $k > (d+1)$, we show that the net parity of the system with boundaries can distinguish topological insulators and trivial insulators. Also, by studying the Wilson loop and nested Wilson loop spectra, we show that all the spectral windings of the Wilson loop and nested Wilson loop should be unwound to resolve the Wannier obstruction of fragile TIs. By counting the minimal number of bands required to unwind the spectral winding of the Wilson loop and nested Wilson loop, we determine the minimal number of bands to resolve the Wannier obstruction, which is consistent with the prediction from our diagnosis method of fragile topology. Finally, we show that a $(d+1)$D $(k-1)$th-order TI can be obtained by an adiabatic pumping of dD kth-order TI, which generalizes the previous study of the 2D third-order TI.

I. INTRODUCTION

Understanding the role of crystalline symmetries in the topological properties of materials is a central topic in recent studies of condensed matter. Soon after the discovery of topological insulators protected by time-reversal symmetry [1,2], topological insulators (TIs) and topological superconductors (TSCs) have been systematically classified into 10-fold Altland-Zirnbauer (AZ) classes [3], based on nonspatial symmetries including time-reversal, particle-hole, and chiral symmetries [4–6]. In this classification, TIs are characterized by nontrivial topological invariants and have a Wannier obstruction that is stable against adding trivial bands. Also d-dimensional (dD) TIs possess stable gapless states at the $(d-1)$D boundaries, which is called the bulk-boundary correspondence.

On the other hand, the topological properties of crystalline solids can also be protected by space-group symmetries, which are realized in topological crystalline insulators (TCIs) [7,8]. Compared to the TIs and TSCs classified based on 10-fold AZ classes, TCIs have extremely rich structures because of the large variety of crystalline symmetries forming 230 space groups and 1651 magnetic space groups [9–15]. For instance, recent studies of TCIs have revealed two intriguing properties that are absent in the 10-fold classification of TIs and TSCs, that is, the fragile topology and the higher-order bulk-boundary correspondence.

Fragile topology is one interesting characteristic of some TCIs discovered in recent theoretical studies [16–27]. In general, TCIs are not adiabatically deformable to atomic insulators without breaking symmetries, that is, they have an obstruction to constructing exponentially localized symmetric Wannier states [28–30]. However, the Wannier obstruction of fragile TIs can be resolved by adding appropriately chosen trivial bands. This property of fragile TIs is clearly distinct from the properties of TCIs with stable topology whose band topology is not affected by additional trivial bands. Because of this, TCIs with stable topology can be classified by K theory [9,31–35], where the equivalence class of insulators is examined when adding trivial bands are allowed. This, at the same time, implies that K theory is not an appropriate tool to study fragile TIs. In general, two different approaches can be considered to examine the Wannier obstruction of fragile

_____
[*]bjyang@snu.ac.kr

205126-1

TIs. One is to investigate the symmetry representation of exponentially localized Wannier states [16,21–24,26,27], and the other is to study the winding pattern of the Wilson loop spectrum [17–20,23,26,27]. While both approaches have been applied successfully to characterize the fragile topology of some specific models, the general characterization of fragile TIs based on them has not been achieved yet.

Another intriguing property of some TCIs is that they do not follow the conventional bulk-boundary correspondence. Recently, it has been found that some TCIs have gapless states only in some subspace of the boundary such as hinges or corners [26,36–61]. In general, dD topological phases with gapless states in $(d − k)$D boundaries are called dD kth-order topological phases. In particular, when $1 < k \leqslant d$, they are called higher-order topological phases and their bulk-boundary correspondence has recently been well established [43,44,46,52].

On the other hand, the nature of boundary states of fragile TIs is not clearly understood yet. It is generally expected that the bulk-boundary correspondence of fragile TIs belongs to a rather trivial category. This is because fragile TIs cannot have a peculiar spectral feature at the boundary distinct from that of atomic insulators since the boundary energy spectrum is insensitive to adding trivial bands below the bulk gap. This is also consistent with the fact that topological phases without gapless boundary states are either fragile topological or atomic [24,52]. Nevertheless, some characteristic boundary features of fragile TIs have been reported [20,48]. For instance, it was shown that, in a two-dimensional (2D) fragile TI protected by inversion symmetry, fractional corner charges appear at the boundary when the geometry of the system preserves inversion symmetry [20,48]. Moreover, many atomic insulators protected by rotation symmetry were shown to host fractional corner charges in 2D, which is similar to the case of 2D second-order TIs [36,37,40,45,60,61]. The origin of corner charges in fragile topological and atomic insulators has been attributed to the filling anomaly [60], which denotes an obstruction to fulfill the electron filling for charge neutrality when the relevant crystalline symmetry is preserved [20,40,48,60,61]. To understand the generic boundary properties of fragile TIs and atomic insulators, it is highly desirable to establish their bulk-boundary correspondence beyond that of stable topological insulators.

In this work, we fully characterize the bulk and boundary properties of fragile TIs protected by inversion symmetry. First, we establish the bulk-boundary correspondence of fragile TIs protected by inversion symmetry. For this purpose, we generalize the notion of the dD kth-order TIs to the cases with $k > d$, and show that the dD $(d + 1)$th-order TIs have fragile topology and exhibit the filling anomaly with the associated boundary charge accumulation. On the other hand, dD kth-order TIs with $k > d + 1$ have a featureless boundary even though they have fragile topology. Second, we propose an efficient scheme to diagnose fragile band topology by using the symmetry data in momentum space. Using this method, we show that among all the possible parity configurations of inversion-symmetric insulators, at least 17% of them have fragile topology in 2D while only 3% are fragile TIs in 3D. Finally, we show that the fragile topology of dD kth-order TI with $k > d$ is manifested in the relative winding of the

Wilson loop and nested Wilson loop spectra. Here, we mainly focus on the class A of AZ classification that does not have time-reversal, particle-hole, chiral symmetries. However, we anticipate that the idea we propose here can be generalized to other AZ classes. In particular, the Dirac Hamiltonians of generalized higher-order topological phases are discussed in Appendix E.

To generalize the notion of the higher-order topology to the cases with $k > d$, we use the Dirac Hamiltonian approach that has been developed recently to understand the higher-order topology with $1 < k \leqslant d$ [44]. In Ref. [44], it is shown that when a Dirac Hamiltonian has $(k − 1)$ mass terms odd under inversion in addition to the mass term even under inversion, the Dirac Hamiltonian describes a kth-order topological phase. The mass term even under inversion is the bulk mass term $\mathcal{M}$ while the other mass terms odd under inversion are boundary mass terms $m_{a,\boldsymbol{r}}$ ($a = 1, \ldots, k − 1$). Then, the energy gap at the boundary $E_g = 2\sqrt{\sum_{a=1}^{k-1} m_{a,\boldsymbol{r}}^2}$ vanishes in the $(d − k)$D subspace of the boundary because the boundary mass terms vanish there due to the constraint $m_{a,\boldsymbol{r}} = −m_{a,−\boldsymbol{r}}$ imposed by inversion symmetry.

Using the Dirac Hamiltonian formalism, it is straightforward to extend the notion of higher-order topology to the cases with $k > d$ [51,57,59]. For instance, dD $(d + 1)$th-order TIs have d boundary mass terms, so the boundary is fully gapped in general. In this case, even though the boundary is gapped, inversion symmetry requires that the $(d + 1)$ mass terms, including d boundary mass terms and the bulk mass term, form a skyrmionlike structure in real space, and have an odd winding number along the boundary. In Refs. [57,59], it was shown that 3D fourth-order Dirac Hamiltonian in $\mathbb{R}^3$ is equivalent to a bound state at the origin. However, the relevant bulk-boundary correspondence was not discussed. In this paper, we show that the winding number of boundary mass terms gives rise to the filling anomaly using the Goldstone-Wilczek formula [62]. A related idea has already been proposed for $d = 2$ in Ref. [20] but our theory is generally valid in arbitrary spatial dimensions. We also clarify the spatial location of extra charge accumulation or depletion. According to the Goldstone-Wilczek formula, since the extra charge density is determined by the mass winding density, the extra charges are localized in the region where the mass terms change rapidly. Since the bulk mass term changes rapidly at the boundary, the induced charges are naturally located at the boundary. The actual location of the extra charge is the position on the boundary where the boundary mass terms vary abruptly. Because of this reason, when the geometry of the system has sharp corners, the extra charges appear there. On the other hand, when the geometry of the system has only smooth boundary, the extra charges are spread over the whole boundary, as confirmed by numerical calculations.

Under the periodic boundary condition in which the fragile band topology is defined, dD $(d + 1)$th-order TIs can be constructed in the following way. We start from an insulator with $2^{d−1}$ occupied bands in which all the occupied bands have positive parities at all inversion-invariant momenta. Let us call such an insulator as a trivial-parity insulator. Then, replacing all the positive-parity states at an odd number of inversion-invariant momenta by negative-parity

states gives a dD $(d+1)$th-order TI. In particular, when a dD $(d+1)$th-order TI has negative-parity states only at a single inversion-invariant momentum, the transition between the trivial-parity insulator and the dD $(d+1)$th-order TI can naturally be described by a Dirac Hamiltonian. In this construction, dD kth-order TIs with $k > d$ have the fragile band topology. In particular, a minimal fragile TI with the filling anomaly can be considered as a dD $(d+1)$th-order TI. One can construct a dD kth-order TI with $k > (d+1)$ by stacking dD $(d+1)$th-order TIs. In general, a dD kth-order TI with $k > (d+1)$ does not have any nontrivial feature at the boundary although it has fragile topology. Nevertheless, we show that the trivial-parity insulator and dD kth-order TI can be distinguished by the net parity $\mathcal{I} = N_- - N_+$ [14,63,64] of a finite-size system with open boundary, defined by the difference between the number of occupied states with odd parity N_- and the number of occupied states with even parity N_+. In fact, the net parity $\mathcal{I}$ defined for the given geometry of the finite-size system is identical to one of bulk topological invariants for inversion-symmetric fragile TIs and atomic insulators. This is consistent with the layer construction proposed in Refs. [52,56,58,63,64].

The properties of fragile TIs discussed above are rigorously confirmed by analyzing the symmetry data, that is, the inversion parities at inversion-invariant momenta in the Brillouin zone. In fact, in recent studies, it is found that parities can be organized in the form of symmetry indicators that distinguish stable topological phases from fragile topological or atomic insulators [11]. However, this method cannot analyze fragile TIs. Here, we establish a simple criterion that can be used to distinguish fragile TIs from atomic insulators efficiently. Using this method, we estimate the number of the parity configurations corresponding to inversion-symmetric stable TIs, fragile TIs, and atomic insulators, respectively, in both 2D and 3D.

To investigate the fragile topology further, we systematically examine how many trivial bands are required to turn a fragile TI to an atomic insulator. Using our criterion for fragile topology, we show that for the dD $(d+1)$th-order TI which has 2^{d-1} occupied bands, $(2^{d-1} - 1)$ bands are needed to trivialize the fragile topology. We explain why $(2^{d-1} - 1)$ bands are necessary for trivialization by using the Wilson loop method. The idea is that all the spectral winding of Wilson loops [65–67] and (generalized) nested Wilson loops [36,37] have to be unwound to completely resolve the Wannier obstruction in fragile topological phases. Explicitly, we show that the total number of bands needed to trivialize the dD $(d+1)$th-order TIs can be decomposed into $2^{d-1} - 1 = 2^{d-2} + 2^{d-3} + \cdots + 1$, where 2^{d-2-l} is the number of bands needed to remove the spectral winding of the lth nested Wilson loop ($l = 0, 1, 2, \dots$). Here, the zeroth nested Wilson loop denotes the conventional Wilson loop. We also generalize this idea to dD kth-order TIs with $k > (d+1)$ which also have fragile topology.

The rest of this paper is organized as follows. We start Sec. II with the Su-Schrieffer-Heeger (SSH) model in order to introduce the concepts of dD $(d+1)$th-order TIs and its higher-order generalizations. Although there is no fragile TI in one dimension because there is no Wannier obstruction in one dimension [30,66,68,69], all the ideas related with the

bulk-boundary correspondence can be generalized straightforwardly to higher dimensions. In Sec. III, we introduce the Dirac Hamiltonians of dD kth-order TIs for arbitrary d and k. Then, we show that the d boundary mass terms of dD $(d+1)$th-order TI have a nontrivial winding number on the boundary in the presence of inversion symmetry. The winding number of boundary mass terms is directly connected to the induced current which dictates the nontrivial charge accumulation at the boundary. In Sec. IV, we construct a mapping between a parity configuration in the Brillouin zone and the inversion-symmetric Wannier states. With the mapping, we obtain $(2^d + 1)$ invariants for the class A inversion-symmetric insulators in d dimensions. From this, we develop an efficient method for diagnosing the atomic, fragile topological, and stable topological phases and classify all the possible parity configurations in two and three dimensions. Also, we introduce the net parity of a finite-size system with open boundary and the condition for the presence of the filling anomaly. In Sec. V, we demonstrate our theoretical prediction through numerical calculations of tight-binding models with open boundary condition. In Sec. VI, we show that fragile topological phases protected by inversion symmetry are characterized by the relative winding [66] in the (nested) Wilson loop spectrum, which is fragile against adding trivial bands. Using the 3D fourth-order TI as a concrete example, we count the number of trivial bands needed to unwind the relative winding in the Wilson loop and the nested Wilson loop spectra and show that this matches with the result expected from our diagnosis method. Then, we generalize this counting to the case of dD kth-order TIs. In Sec. VII, we study the general pumping process of inversion-symmetric insulators. Specifically, we construct $(d+1)$D $(k-1)$th-order TI by a pumping of dD kth-order TI, which generalizes the result in Ref. [20] for $d = 2$ and $k = 3$. Finally, we conclude in Sec. VIII.

II. SYMMETRY DATA AND GENERALIZED HIGHER-ORDER TOPOLOGY IN ONE DIMENSION

Here we introduce the notion of the generalized higher-order topology in one-dimensional (1D) systems by considering the Su-Schrieffer-Heeger (SSH) model [70] and its multiple copies. Let us note that the meaning of "topological phases" is a bit subtle in 1D since only atomic and obstructed atomic insulators [10] exist in 1D [30,66,68,69], in contrast to higher-dimensional systems where topological phases mean the phases with either fragile or stable band topology. For convenience, however, here we use the term "topological phases" to denote the obstructed atomic insulators in 1D systems.

A. Second-order topology in 1D

Let us begin with the 1D SSH model Hamiltonian with inversion symmetry,

$$H_{\text{SSH}}(k) = \sin k \, \sigma_x + (t + \cos k) \, \sigma_z, \tag{1}$$

which is invariant under inversion symmetry $I = \sigma_z$ as well as chiral symmetry $S = \sigma_y$, that is,

$$I H_{\text{SSH}}(k) I^{-1} = H_{\text{SSH}}(-k), \quad S H_{\text{SSH}}(k) S^{-1} = -H_{\text{SSH}}(k). \tag{2}$$

TABLE I. The parity of the occupied state at inversion-invariant momenta of inversion-symmetric atomic insulators. s and p denote the even- and odd-parity states, respectively. A and B are Wyckoff positions of 1D inversion-symmetric lattices shown in Fig. 1(a).

Orbital	$k = 0$	$k = \pi$
$s(A)$	$+$	$+$
$p(A)$	$-$	$-$
$s(B)$	$+$	$-$
$p(B)$	$-$	$+$

The energy spectrum is given by $E(k) = \pm\sqrt{\sin^2 k + (t + \cos k)^2}$, which is gapped when $|t| \neq 1$. When $t = 1$ ($t = -1$), the band gap closes at $k = \pi$ ($k = 0$).

The insulating phases are distinguished by a topological invariant, which is nothing but the winding number of the two-component vector $(t + \cos k, \sin k)$ around the origin $(0,0)$, so that the insulating phase is topological when $|t| < 1$ while it is trivial when $|t| > 1$.

The topological and trivial insulators can also be distinguished by the parity configuration of occupied states at inversion-invariant momenta. In the trivial phase, the parity of the occupied band at $k = 0$ (p_0) and that at $k = \pi$ (p_π) is $(p_0, p_\pi) = (-, -)$ when $t > 1$ while $(p_0, p_\pi) = (+, +)$ when $t < -1$. In the topological phase with $|t| < 1$, $(p_0, p_\pi) = (-, +)$. Table I shows the parity configurations of atomic insulators with inversion symmetry, which shows that the parity configuration of the topological insulator is equivalent to that of the atomic insulator with a p orbital at the Wyckoff position B. On the other hand, the parity configuration of the trivial insulator is equivalent to that of the atomic insulator with a s (p) orbital at the Wyckoff position A when $t < -1$ ($t > 1$) [see Fig. 1(b)].

To examine the surface states, let us construct a heterostructure composed of a topological insulator in the region with $|x| < L/2$ and trivial insulators on the sides with $|x| > L/2$. Such a heterostructure can also be described by
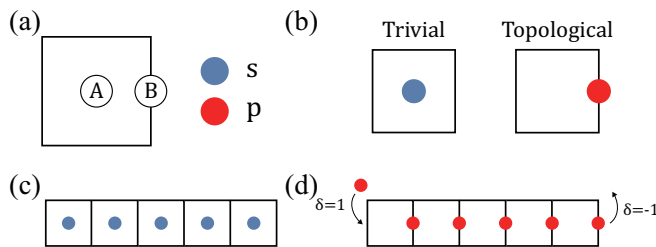

FIG. 1. The Wannier center of 1D SSH model and filling anomaly. (a) Wyckoff positions A and B of a 1D inversion-symmetric lattice. s and p orbitals are denoted by the blue and red circles, respectively. (b) The parity configurations of trivial and topological phases are equivalent to those of the atomic insulators $s(A)$ and $p(B)$, respectively. (c) A finite-size trivial insulator with open boundaries, which is inversion symmetric. (d) A finite-size topological phase with open boundaries cannot be made inversion symmetric. In order to have inversion-symmetric ground state, one extra electron must be added ($\delta = 1$) or removed ($\delta = -1$) to the half-filled system, which is called the filling anomaly [60].
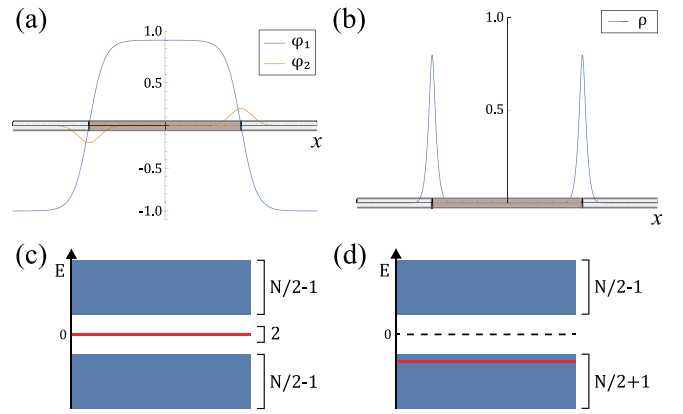

FIG. 2. Mass profiles of the 1D SSH model and the relevant charge density and energy spectrum. (a) A heterostructure composed of a 1D topological insulator at $|x| < L/2$ sandwiched by trivial insulators at $|x| > L/2$. The domain walls between the trivial and topological insulators described in Eqs. (3) and (4) are implemented by using $\varphi_1(x) = -1 - \tanh(\frac{x - L/2}{l_1}) + \tanh(\frac{x + L/2}{l_1})$ and $\varphi_2(x) = 0.2(\exp[-(\frac{x - L/2}{l_2})^2] - \exp[-(\frac{x + L/2}{l_2})^2])$. $l_1 = l_2 = \frac{L}{10}$ are used. The domain of the topological insulator is depicted by a brown rod. Two ends of the rod are located at $x = \pm\frac{L}{2}$. (b) The accumulated charge density ρ when the second mass term $\varphi_2(x)$ is added. $\rho(x)$ is localized only in the region where the bulk mass $\varphi_1(x)$ changes its sign. (c) The energy spectrum of $\mathcal{H}_{(1,1)}$ in Eq. (3). Two zero-energy states localized at domain walls are degenerate due to inversion symmetry. (d) The energy spectrum of $\mathcal{H}_{(1,2)}$ in Eq. (4) with the boundary mass term $\varphi_2(x)$ that breaks chiral symmetry but preserves inversion symmetry. The pair of domain wall states are merged into the bulk spectrum. There is a single hole in the valence band at half-filling indicating the filling anomaly.

the Hamiltonian in Eq. (1) when t depends on the spatial coordinate x. For simplicity, we assume that $-1 < t(x) < 1$ for $|x| < L/2$ and $t(x) < -1$ for $|x| > L/2$. Since the band gap closes at $k = 0$ at the critical point with $t = -1$, one can consider the following low-energy Dirac Hamiltonian:

$$\mathcal{H}_{(1,1)} = k\sigma_x + \varphi_1(x)\sigma_z, \qquad (3)$$

where $\varphi_1(x) \equiv 1 + t(x)$ that plays the role of a bulk mass term. Then, $\varphi_1(x) > 0$ for $|x| < L/2$ and $\varphi_1(x) < 0$ for $|x| > L/2$. $\varphi_1(x) = \varphi_1(-x)$ due to inversion symmetry. Let us note that the symbol $\mathcal{H}_{(d,k)}$ indicates the dD Dirac Hamiltonian with k anticommuting mass terms.

When the length L is sufficiently large, there are two zero-energy states at two edges (or two domain walls), where the bulk mass term $\varphi_1(x)$ changes its sign [see Fig. 2(c)]. Because of inversion symmetry, the two edge states should be either occupied or unoccupied simultaneously. Thus, an inversion-symmetric ground state cannot satisfy the exact half-filling condition, which is described in Figs. 1(c) and 1(d). This phenomenon is known as the *filling anomaly* [60].

Let us now break chiral symmetry by adding an inversion-symmetric second mass term $\varphi_2(x)$ to $\mathcal{H}_{(1,1)}$, which gives

$$\mathcal{H}_{(1,2)} = k\sigma_x + \varphi_1(x)\sigma_z + \varphi_2(x)\sigma_y, \qquad (4)$$

where $\varphi_2(x) = -\varphi_2(-x)$. We assume that $\varphi_2(x)$ is finite only around the domain wall and call this type of mass term as "boundary" mass terms. The Dirac Hamiltonian with $(k - 1)$

boundary mass terms describes a kth-order topological insulator. In this respect, $\mathcal{H}_{(1,2)}$ means the Dirac Hamiltonian of 1D second-order TI. We generalize the notion of dD kth-order TI for arbitrary k in Sec. III A.

The boundary mass term φ_2 makes the energy of the edges states shifted from zero. However, since inversion symmetry is maintained, the two edge states are still degenerate, and thus the filling anomaly remains. In particular, the profile of φ_2 depicted in Fig. 2(a) lowers the energy of the edge states. When the edge states are occupied simultaneously, the system has one extra charge relative to the half-filling, and the resulting phase is said to have the filling anomaly with $\delta = 1$ [see Fig. 2(d)].

The extra charge density accumulated at a domain wall shown in Fig. 2(b) is given by the Goldstone-Wilczek formula [62]

$$\rho(x) = \frac{1}{2\pi} \epsilon^{ab} \frac{\varphi_a \partial_x \varphi_b}{\varphi^2} = \frac{1}{2\pi} \partial_x \tan^{-1}\left(\frac{\varphi_2}{\varphi_1}\right). \quad (5)$$

It is worth noting that Eq. (5) shows that the extra charge is accumulated mostly at the domain wall, even when the edge spectrum merges into the bulk spectrum. This is because the bulk mass term φ_1 varies only near the domain wall where the accumulated charge density is located. This property is shared by any dD $(d + 1)$th-order inversion-symmetric TI as shown in Sec. III C.

The total amount of the extra charge $Q = \int dx \, \rho(x)$ is given by the winding number of (φ_1, φ_2). Note that we can compactify R^1 to S^1 since $(\varphi_1, \varphi_2) \to (-1, 0)$ at $x \to \pm\infty$, and thus the integer winding number can be defined. The boundary conditions on φ_1 and φ_2 imposed by inversion symmetry constrain Q to be 1. This result is consistent with the picture based on the shifting of the energy level of the edge states by adding φ_2. When the bulk mass term $\varphi_1(x)$ changes its sign near each domain wall, $\tan^{-1}\left(\frac{\varphi_2}{\varphi_1}\right)$ is abruptly changed by π. Therefore, a half-integral charge should be accumulated at each domain wall.

B. Third- and fourth-order topologies

The idea of higher-order topology can be generalized further even to the cases with $k > (d + 1)$. To illustrate the idea, let us first consider two copies of the SSH model. The relevant Hamiltonian is obtained by doubling $H_{\text{SSH}}(k)$ in an inversion-symmetric way as

$$H(k) = \tau_x \otimes H_{\text{SSH}}(k) = \sin k \, \tau_x \sigma_x + (t + \cos k) \, \tau_x \sigma_z. \quad (6)$$

The corresponding Dirac Hamiltonian linearized near $k = 0$ is

$$\mathcal{H} = k \, \tau_x \sigma_x + \varphi_1(x) \, \tau_x \sigma_z, \quad (7)$$

where $\varphi_1(x) > 0$ for $|x| < L/2$ and $\varphi_1(x) < 0$ for $|x| > L/2$, which again describes a heterostructure with two domain walls at $x = \pm L/2$. The Hamiltonian $\mathcal{H}$ is invariant under inversion symmetry $I = \tau_x \sigma_z$ and chiral symmetry $S = \tau_z \sigma_0$. When chiral symmetry $S = \tau_z \sigma_0$ is preserved, two boundary mass terms $\varphi_2(x) \tau_x \sigma_y$ and $\varphi_3(x) \tau_y \sigma_0$ are allowed. Adding them to $\mathcal{H}$ gives

$$\mathcal{H}_{(1,3)} = k \, \tau_x \sigma_x + \varphi_1(x) \, \tau_x \sigma_z + \varphi_2(x) \, \tau_x \sigma_y + \varphi_3(x) \, \tau_y \sigma_0, \quad (8)$$
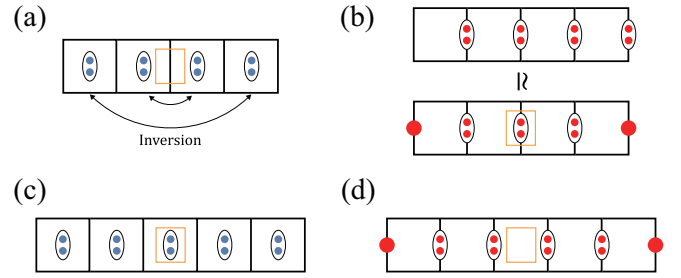

FIG. 3. The Wannier centers of 1D third- and fourth-order TIs and net parities. (a) Two copies of trivial insulators of a finite-size with even N_{cell}. All unit cells form inversion-symmetric pairs giving an equal number of even-parity and odd-parity states, and thus $\mathcal{I} = 0$. (b) Two copies of trivial insulators of a finite size with even N_{cell}. The upper configuration is rearranged into the lower one which is inversion symmetric. All p orbitals except the two at the center within the orange box form the equal number of bonding and antibonding states, and thus $\mathcal{I} = 2$. (c) Similar to (a) but with odd N_{cell}. All s orbitals except the two at the center form inversion-symmetric pairs, and thus $\mathcal{I} = -2$. (d) Similar to (b) but with odd N_{cell}. All orbitals form inversion-symmetric pairs, and thus $\mathcal{I} = 0$. In all cases, $\mathcal{I} \equiv N_- - N_+$ is determined by the difference in the number of p and s orbitals at the center within the orange box.

where $\varphi_{2,3}(x) = -\varphi_{2,3}(-x)$. The resulting Dirac Hamiltonian describes a 1D third-order TI belonging to class AIII.

There is one remaining boundary mass term $\varphi_4(x) \tau_z \sigma_0$ that breaks S but keeps I. By adding this term to $\mathcal{H}_{(1,3)}$, we obtain the following Dirac Hamiltonian:

$$\mathcal{H}_{(1,4)} = k \, \tau_x \sigma_x + \varphi_1(x) \, \tau_x \sigma_z + \varphi_2(x) \, \tau_x \sigma_y$$
$$+ \varphi_3(x) \, \tau_y \sigma_0 + \varphi_4(x) \, \tau_z \sigma_0, \quad (9)$$

which describes a 1D fourth-order TI belonging to class A.

For both $\mathcal{H}_{(1,3)}$ and $\mathcal{H}_{(1,4)}$, there are neither the filling anomaly nor zero-energy states. However, the relative topology between the trivial and topological phases can still be revealed by real-space wave function.

To demonstrate the idea, let us consider a finite-size doubled SSH model composed of N_{cell} unit cells in which the total number of energy eigenstates is $4N_{\text{cell}}$. In the case of a trivial insulator, two s orbitals are located at the center of each unit cell, whereas, in the case of a topological insulator, two p orbitals are located at a boundary of each unit cell. We first consider a trivial insulator with an even integer N_{cell} shown in Fig. 3(a). Since a unit cell is related with another unit cell via inversion symmetry, their bonding and antibonding combinations generate equal number of even- and odd-parity states. That is, $N_+ = N_- = N_{\text{cell}}$ where N_+ (N_-) denotes the number of occupied bands with even (odd) parity. Similarly, when N_{cell} is odd as shown in Fig. 3(c), all the unit cells except the one at the center form inversion-symmetric pairs, and contribute equally to N_+ and N_-. However, the central unit cell containing two s orbitals at the inversion center contributes 2 only to N_+, which leads to $N_+ = N_{\text{cell}} + 1$ and $N_- = N_{\text{cell}} - 1$.

Similar analysis can be done for topological insulators. Since there is no filling anomaly, a finite-size doubled SSH model can have inversion-symmetric atomic configurations as shown in Figs. 3(b) and 3(d). In contrast to the trivial insulator

TABLE II. The relation between N_+, N_-, N_{cell}, and $\mathcal{I}$ for doubled SSH models of finite size, which corresponds to the 1D third and fourth-order topological insulators described by $\mathcal{H}_{(1,3)}$ and $\mathcal{H}_{(1,4)}$.

N_{cell}	Phase	N_+	N_-	$\mathcal{I}$
Even	Trivial	N_{cell}	N_{cell}	0
	Topological	$N_{\text{cell}} - 1$	$N_{\text{cell}} + 1$	2
Odd	Trivial	$N_{\text{cell}} + 1$	$N_{\text{cell}} - 1$	-2
	Topological	N_{cell}	N_{cell}	0

TABLE III. The relation between N_+, N_-, $N_\pm$, and $\mathcal{I}$ for the 1D second-order TI described by $\mathcal{H}_{(1,2)}$ when the extra charge δ is added due to the filling anomaly.

N_{cell}	Phase	N_+	N_-	$\mathcal{I}$
Even	Trivial	N_{cell}	N_{cell}	0
	Topological	$\frac{1}{2}(N_{\text{cell}} + \delta - 1)$	$\frac{1}{2}(N_{\text{cell}} + \delta + 1)$	1
Odd	Trivial	$\frac{1}{2}(N_{\text{cell}} + 1)$	$\frac{1}{2}(N_{\text{cell}} - 1)$	-1
	Topological	$\frac{1}{2}(N_{\text{cell}} + \delta)$	$\frac{1}{2}(N_{\text{cell}} + \delta)$	0

in which orbitals are located at the center of each unit cell, the orbitals of a topological insulator are located at the edges of each unit cell. When N_{cell} is even, p orbitals at an edge are related with other p orbitals via inversion symmetry, and their bonding and antibonding combinations contribute equally to N_+ and N_-. Since the remaining two p orbitals at the inversion center contribute 2 only to N_-, we have $N_+ = N_{\text{cell}} - 1$ and $N_- = N_{\text{cell}} + 1$. On the other hand, when N_{cell} is odd, all p orbitals are related by inversion symmetry and thus $N_+ = N_- = N_{\text{cell}}$. The dependence of $N_\pm$ on the parity of N_{cell} is summarized in Table II.

The four distinct cases considered above can be distinguished in terms of the net parity $\mathcal{I}$ [14,63,64] defined as (with an additional -1 in our convention)

$$\mathcal{I} \equiv N_- - N_+. \tag{10}$$

Since a pair of orbitals related by inversion symmetry contribute equally to N_+ and N_-, they do not contribute to $\mathcal{I}$. Thus, it is determined by the difference in the number of p and s orbitals localized at the inversion center of the finite-size system. When N_{cell} is even, one can easily find $\mathcal{I} = 0$ ($\mathcal{I} = 2$) for a trivial (topological) insulator. On the other hand, when N_{cell} is odd, we obtain $\mathcal{I} = -2$ ($\mathcal{I} = 0$) for a trivial (topological) insulator (see Fig. 3).

A similar analysis can also be applied to the 1D second-order TI in which the filling anomaly exists. The result is summarized in Fig. 4 and Table III. In fact, $\mathcal{I}$ can serve as a bulk topological invariant for general
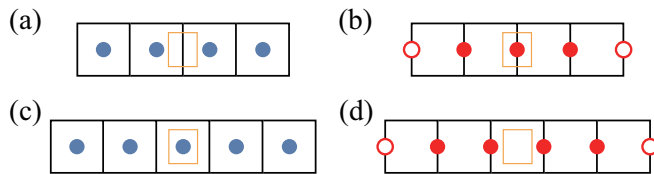

FIG. 4. The Wannier centers of 1D second-order TI and net parities. (a) Atomic configuration for a finite-size trivial insulator relevant to the 1D second-order TI when N_{cell} is even. All s orbitals form inversion-symmetric pairs, and thus $\mathcal{I} = 0$. (b) Atomic configuration for a finite-size topological insulator relevant to the 1D second-order TI when N_{cell} is even. The red empty circles at the boundaries must be occupied or unoccupied simultaneously because of the filling anomaly. All p orbitals except the one at the center form inversion-symmetric pairs, and thus $\mathcal{I} = 1$. (c) Similar to (a) but when N_{cell} is odd. All s orbitals except the one at the center form inversion-symmetric pairs, and thus $\mathcal{I} = -1$. (d) Similar to (b) but when N_{cell} is odd. All p orbitals form inversion-symmetric pairs, and thus $\mathcal{I} = 0$.

inversion-symmetric insulators without gapless boundary states, which is discussed in Sec. IV E.

III. GENERALIZED HIGHER-ORDER TOPOLOGY IN $d > 1$ DIMENSIONS

A. Dirac Hamiltonian approach

Here, we extend the notion of dD kth-order TI with $k > d$ to general dimensions $d > 1$. We focus on the symmetry class A of the AZ symmetry classification. For this purpose, we use the Dirac Hamiltonian describing the transition between two topologically distinct phases. The Dirac Hamiltonians of inversion-symmetric TI/TSCs have been exhaustively studied in Ref. [44] that we refer to construct the Dirac Hamiltonian with generalized higher-order topology.

In general, a Dirac Hamiltonian is expressed in terms of $2^n \times 2^n$ Γ matrices which satisfy the Clifford algebra $\{\Gamma_i, \Gamma_j\} = 2\delta_{ij}$ for $i, j = 1, \ldots, 2n + 1$ as

$$\mathcal{H}_0(\boldsymbol{k}) = \sum_{i=1}^{d} k_i \Gamma_i + \lambda \mathcal{M}, \tag{11}$$

where $\{\mathcal{M}, \Gamma_i\} = 0$ and $\mathcal{M}^2 = \mathbb{1}_{2^n}$. Here, $\mathbb{1}_{2^n}$ denotes the $2^n \times 2^n$ identical matrix. In Eq. (11), $\mathcal{M}$ is the bulk mass term because the energy eigenvalues are given by $E(\boldsymbol{k}) = \pm\sqrt{k^2 + \lambda^2}$. Changing the sign of the bulk mass term $\mathcal{M}$ flips all the inversion parities at $\boldsymbol{k} = 0$. We choose $\lambda > 0$ ($\lambda < 0$) to mean the topological (trivial) insulator. Here, we consider the cases when the inversion symmetry operator is identical to the bulk mass term, i.e., $I = \mathcal{M}$. When we choose $\mathcal{M} = \Gamma_{2n+1}$, there remain $(2n - d)$ additional mass terms, $m_1\Gamma_{d+1} + \cdots + m_{2n-d}\Gamma_{2n}$, which anticommute with $\mathcal{M}$, and thus break inversion symmetry when $m_{i=1,\ldots,2n-d}$ are constant.

Now we consider a topological insulator with boundaries whose global shape is inversion symmetric, and allow the position $\boldsymbol{r}$ dependence of both the bulk mass term $\lambda(\boldsymbol{r})\mathcal{M}$ and the boundary mass terms $m_{a,\boldsymbol{r}}\Gamma_{d+a}$ with $a = 1, \ldots, 2n - d$. The corresponding inversion-symmetric Dirac Hamiltonian including the boundary mass terms is given by

$$\mathcal{H}(\boldsymbol{k}, \boldsymbol{r}) = \sum_{i=1}^{d} k_i \Gamma_i + \lambda(\boldsymbol{r})\mathcal{M} + \sum_{a=1}^{2n-d} m_{a,\boldsymbol{r}} M_a, \tag{12}$$

where $M_a = \Gamma_{d+a}$ and $\lambda(\boldsymbol{r}) > 0$ [$\lambda(\boldsymbol{r}) < 0$] inside (outside) the topological insulator. $\mathcal{H}(\boldsymbol{k}, \boldsymbol{r})$ satisfies

$$I\mathcal{H}(\boldsymbol{k}, \boldsymbol{r})I^{-1} = \mathcal{H}(-\boldsymbol{k}, -\boldsymbol{r}), \tag{13}$$

in which $m_{a,\boldsymbol{r}} = -m_{a,-\boldsymbol{r}}$.

The order k of $\mathcal{H}(\boldsymbol{k}, \boldsymbol{r})$ is defined as follows. At the boundary $\boldsymbol{r}$ with $\lambda(\boldsymbol{r}) = 0$, the energy gap is given by $2m_s(\boldsymbol{r})$ where $m_s(\boldsymbol{r}) = \sqrt{\sum_{a=1}^{2n-d} m_{a,\boldsymbol{r}}^2}$. When $k \leqslant d$ where $k = 2n - d + 1$, all boundary mass terms $m_{a,\boldsymbol{r}}$ vanish simultaneously on $(d - k)$D domain due to the condition $m_{a,\boldsymbol{r}} = -m_{a,-\boldsymbol{r}}$ imposed by inversion symmetry. In this case, the order is given by k, which is the conventional way of defining the order of a topological insulator. On the other hand, when $k > d$, the boundary states are fully gapped, and thus the order k cannot be well defined. In spite of this, however, we generalize the definition of the order k so that $(k - 1)$ is identical to the number of boundary mass terms. Namely, when a dD Dirac Hamiltonian has $(k - 1)$ boundary mass terms, the relevant TI is a dD kth-order TI as defined in Sec. I. Let us emphasize once again that a dD kth-order TI in periodic systems can be well defined by the Dirac Hamiltonian when the relevant trivial insulator is the trivial-parity insulator, so that the sign reversal of the bulk mass term mediates the transition between the trivial-parity insulator and the dD kth-order TI.

Now we consider the Dirac Hamiltonian for dD kth-order TI with $k > d$. Since a dD kth-order TI exists only when $d + k = 2l + 1$ where $l = 1, 2, \ldots$, the minimal order k of a dD TI without gapless boundary states described by a Dirac Hamiltonian is $k = d + 1$. The Dirac Hamiltonian of dD $(d + 1)$th-order TI is

$$\mathcal{H}(\boldsymbol{k}, \boldsymbol{r}) = \sum_{i=1}^{d} k_i \Gamma_i + \lambda(\boldsymbol{r}) \mathcal{M} + \sum_{a=1}^{d} m_{a,\boldsymbol{r}} M_a. \quad (14)$$

Then, dD kth-order TI with $k > (d + 1)$ can be obtained by superposing $2^{\frac{k-d-1}{2}}$ copies of dD $(d + 1)$th-order TI. For instance, in 1D, we have obtained the 1D fourth-order TI by doubling the 1D second-order TI. Interestingly, all dD kth-order TIs with $k > d$ turn out to be a fragile phase as shown in Sec. V. The properties of the Dirac Hamiltonian of dD $(d + 1)$th-order TI in Eq. (14) are discussed in detail in Secs. III B and III C.

B. Homotopy of boundary mass terms

The Dirac Hamiltonian for the boundary theory $h(\boldsymbol{k}, \boldsymbol{r})$ is obtained via the boundary projection of the bulk Hamiltonian [43,44,46,52]

$$h(\boldsymbol{k}, \boldsymbol{r}) = P_+(\boldsymbol{r}) \mathcal{H}(\boldsymbol{k}, \boldsymbol{r}) P_+(\boldsymbol{r}), \quad (15)$$

where $P_+(\boldsymbol{r}) = \frac{1}{2}[\mathbb{1} - i(\boldsymbol{n}_{\boldsymbol{r}} \cdot \boldsymbol{\Gamma}) \mathcal{M}]$ denotes the projection operator to the boundary where $\boldsymbol{n}_{\boldsymbol{r}}$ is the surface normal vector at the position $\boldsymbol{r}$ and $\boldsymbol{\Gamma} = (\Gamma_1, \ldots, \Gamma_d)$. Thus, the boundary theory of dD $(d + 1)$th-order TI is given by

$$h(\boldsymbol{k}, \boldsymbol{r}) = \boldsymbol{k}_S \cdot \tilde{\boldsymbol{\Gamma}} + \sum_{a=1}^{d} m_{a,r} \tilde{M}_a, \quad (16)$$

where $\boldsymbol{k}_S = \boldsymbol{k} - (\boldsymbol{k} \cdot \boldsymbol{n}_{\boldsymbol{r}}) \boldsymbol{n}_{\boldsymbol{r}}$ denotes the boundary momentum and $\tilde{\Gamma}_i$ and $\tilde{M}_a$ are boundary-projected gamma matrices and mass matrices. The details about the boundary projection are summarized in Appendix F. The boundary states of Eq. (16) are gapped everywhere because of d distinct boundary mass terms. Since there is no gapless boundary state, the system seems to be topologically trivial. However, we show that the

nontrivial higher-order band topology is manifested in the nontrivial winding structure of the boundary mass terms in real space. With a unit vector $\boldsymbol{\varphi}(\boldsymbol{r})$ defined in terms of the boundary mass terms $\vec{m}_{\boldsymbol{r}} = (m_{1,\boldsymbol{r}}, \ldots, m_{d,\boldsymbol{r}})$,

$$\boldsymbol{\varphi}(\boldsymbol{r}) = \frac{\vec{m}_{\boldsymbol{r}}}{|\vec{m}_{\boldsymbol{r}}|}, \quad (17)$$

one can consider a mapping from the boundary position $\boldsymbol{r}$ to the unit vector $\boldsymbol{\varphi}(\boldsymbol{r})$. Note that $\boldsymbol{\varphi}(\boldsymbol{r})$ is well defined since the boundary gap $m_s(\boldsymbol{r}) = |\vec{m}_{\boldsymbol{r}}|$ is nonzero everywhere on the boundary. Also, $\boldsymbol{\varphi}(\boldsymbol{r})$ satisfies $\boldsymbol{\varphi}(\boldsymbol{r}) \cdot \boldsymbol{\varphi}(\boldsymbol{r}) = 1$. Since both the boundary and $\boldsymbol{\varphi}(\boldsymbol{r})$ are homotopic to the $(d - 1)$D sphere S^{d-1}, one can define the homotopy group $\pi_{d-1}(S^{d-1}) = \mathbb{Z}$. The winding numbers w_d relevant to $\pi_d(S^d) = \mathbb{Z}$ are given by

$$w_1 = \int d\theta \, \frac{1}{2\pi} \partial_\theta \tan^{-1}\left(\frac{\varphi_2(\theta)}{\varphi_1(\theta)}\right), \quad (18)$$

$$w_2 = \int d\theta \, d\phi \, \frac{1}{4\pi} \boldsymbol{\varphi}(\theta, \phi) \cdot \partial_\theta \boldsymbol{\varphi}(\theta, \phi) \times \partial_\phi \boldsymbol{\varphi}(\theta, \phi), \quad (19)$$

and similar expressions in higher dimensions. When the system is inversion symmetric, the unit vector $\boldsymbol{\varphi}(\boldsymbol{r})$ should satisfy

$$\boldsymbol{\varphi}(\boldsymbol{r}) = -\boldsymbol{\varphi}(-\boldsymbol{r}). \quad (20)$$

With this configuration, the winding number is constrained to be an odd integer [71]. Let us note that even when a phase transition at the boundary occurs, the winding number modulo 2 remains invariant due to Eq. (20). This shows that the winding number w_d of boundary mass terms characterizes the nontrivial bulk topology. In the following section, Sec. III C, the connection between the winding number w_d and the bulk-boundary correspondence of dD $(d + 1)$th-order TI is discussed in detail.

C. Induced U(1) current and bulk-boundary correspondence

Consider the Dirac Hamiltonian for a dD $(d + 1)$th-order TI given in Eq. (14),

$$\mathcal{H}_{(d,d+1)} = -\sum_{i=1}^{d} i \Gamma_i \partial_i + \sum_{a=1}^{d+1} m_{a,\boldsymbol{r}} M_a, \quad (21)$$

where $m_{d+1,\boldsymbol{r}} = \lambda(\boldsymbol{r})$ and $M_{d+1} = \mathcal{M}$. This can be interpreted as the Hamiltonian describing a massless Dirac fermion coupled to $(d + 1)$ scalar fields M_a. Then, the induced electric current J_d^μ is given by

$$J_d^\mu = \frac{s_d}{d! \, \text{Area}(S^d)} \epsilon^{\mu\mu_1 \ldots \mu_d} \epsilon^{a_1 \ldots a_{d+1}}$$
$$\times \Phi_{a_1} \partial_{\mu_1} \Phi_{a_2} \partial_{\mu_2} \ldots \partial_{\mu_d} \Phi_{a_{d+1}}, \quad (22)$$

where $\mu, \mu_i = 0, 1, \ldots, d$, $\partial_0 = \partial_t$, $\Phi_a = \frac{m_{a,\boldsymbol{r}}}{m_{\boldsymbol{r}}}$, $m_{\boldsymbol{r}}^2 = \sum_{a=1}^{d+1} m_{a,\boldsymbol{r}}^2$, $\text{Area}(S^d) = \frac{2\pi^{(d+1)/2}}{\Gamma(\frac{d+1}{2})}$, and $\Gamma(d)$ is the gamma function [72]. Here, the sign of $s_d = \pm 1$ depends on the representation of gamma matrices where $\text{Tr}[\Gamma_1, \ldots, \Gamma_{2d+1}] = 2^d i^d$. In our convention for gamma matrices, $s_d = -(-1)^{\frac{d(d-1)}{2}}$. The derivation of Eq. (22) is given in Appendix G. Let us note that $\partial_\mu J_d^\mu = 0$. Moreover, since $\Phi_a \to \{0, \ldots, 0, -1\}$ as $\boldsymbol{r} \to \infty$, R^d can be compactified to S^d. Then, one can regard $\int_{R^d} J_d$ as a winding number on S^d.

To compute the induced current explicitly, let us consider a finite-size dD $(d + 1)$th-order TI with the boundary between the topological phase and the vacuum (or a trivial insulator). Then, the d boundary mass terms wind along the boundary while the bulk mass term $\lambda(\boldsymbol{r})\mathcal{M}$ varies rapidly across the boundary. According to the expression of J_d^μ in Eq. (22), charges are accumulated in the region where the mass terms vary rapidly, that is, only near the boundary. Note that J_1^μ is also used in Sec. II A to explain the 1D second-order TI [see Eq. (5)]. Since J_d^μ is nonzero only near the boundary, the current density at the boundary j_{d-1}^μ can be determined by integrating J_d^μ along r taking into account $\partial_r m_{a,\boldsymbol{r}} \ll \partial_r m_{d+1,\boldsymbol{r}}$ for $a = 1, \ldots, d$ as

$$
\begin{aligned}
j_{d-1}^\mu &= \int_0^\infty dr\, J_d^\mu \\
&\simeq (-1)^d \frac{s_d}{(d-1)!\, \text{Area}(S^{d-1})} \epsilon^{\mu\mu_1\ldots\mu_{d-1}} \epsilon^{a_1\ldots a_d} \\
&\quad \times \varphi_{a_1} \partial_{\mu_1} \varphi_{a_2} \partial_{\mu_2} \ldots \partial_{\mu_{d-1}} \varphi_{a_d},
\end{aligned}
\tag{23}
$$

where $\varphi_a = \frac{m_{a,\boldsymbol{r}}}{|\vec{m}_{\boldsymbol{r}}|}$ and $\vec{m}_{\boldsymbol{r}} = (m_{1,\boldsymbol{r}}, \ldots, m_{d,\boldsymbol{r}})$. One can also derive Eq. (23) rigorously in the following way. When the domain of the TI is sufficiently large, the boundary theory of dD $(d + 1)$th-order TI given in Eq. (16) can be regarded as the Dirac Hamiltonian defined in R^{d-1} with d mass terms. Then, the induced current J_{d-1}^μ is obtained by the boundary projection, and its sign is fixed by comparison with Eq. (23). We get j_{d-1}^μ at the $(d - 1)$D boundary of dD $(d + 1)$th-order TI after compactifying R^{d-1} to S^{d-1} (see Appendix G).

Equation (23) shows that the total charge of boundary states $\int_{S^{d-1}} j_{d-1}^0$, which is nothing but the anomalous charge δ due to the filling anomaly, is determined by the winding of boundary mass terms as

$$
\delta = \int_{S^{d-1}} j_{d-1}^0 = -(-1)^{\frac{d(d+1)}{2}} w_{d-1}. \tag{24}
$$

We note that the condition $\varphi_a(\boldsymbol{r}) = -\varphi_a(-\boldsymbol{r})$ imposed by inversion symmetry restricts the winding to be an odd integer. The anomalous charge δ modulo two characterizes the bulk-boundary correspondence of dD $(d + 1)$th-order TIs since any inversion-preserving process can change the boundary charge only by even integers unless it closes the bulk gap. The charge densities predicted by j_{d-1}^0 are as follows:

$$
j_0^0 = \frac{1}{2}, \tag{25}
$$

$$
j_1^0 = \frac{1}{2\pi} \epsilon^{0\mu} \epsilon^{ab} \varphi_a \partial_\mu \varphi_b = \frac{1}{2\pi} \partial_\theta \tan^{-1}\left(\frac{\varphi_2}{\varphi_1}\right), \tag{26}
$$

$$
\begin{aligned}
j_2^0 &= -\frac{1}{8\pi} \epsilon^{0\mu\nu} \epsilon^{abc} \varphi_a \partial_\mu \varphi_b \partial_\nu \varphi_c \\
&= -\frac{1}{4\pi} \boldsymbol{\varphi} \cdot \partial_\theta \boldsymbol{\varphi} \times \partial_\phi \boldsymbol{\varphi}.
\end{aligned}
\tag{27}
$$

It is worth noting that the induced currents shown above were also discussed in Refs. [62,73–77] in various contexts. In all the previous studies, however, all the mass terms are considered as either bulk order parameters or bulk pumping parameters in time direction. In contrast to this, in our case, all $\varphi(\boldsymbol{r})$ are defined along the boundary. Thus, the physical

implication of the induced currents in our work is different from that in the previous studies. Before closing this section, let us remark on the cases when the boundary projection is not well defined or the boundary is not smooth. In general, the boundary projection is not well defined when the boundary mass terms are comparable to or larger than the bulk mass term. Nevertheless, as long as the total amount of boundary charge δ (modulo two) is preserved under any bulk gap-preserving and inversion-symmetric perturbation, our discussion on the bulk-boundary correspondence is still valid. When the boundary is not smooth, it can be treated as an extreme curvature limit of the system with smooth boundary. In Sec. V A, we numerically show that our predictions of boundary charge are still valid even when the boundary mass terms are comparable to the bulk mass term and/or the boundary is not smooth. In addition to the total amount of the boundary charge, the distribution of the boundary charge density is also consistent with that of the winding number density.

IV. SYMMETRY DATA AND CLASSIFICATION OF INVERSION-SYMMETRIC INSULATORS

In this section, by using symmetry data, we systematically classify inversion-symmetric insulators into three classes: atomic insulators, fragile topological insulators, and stable topological insulators. In particular, we provide a convenient scheme to diagnose fragile topology, and estimate the number of parity configurations belonging to each class. Also, we discuss the net parity of a finite-size system with open boundary and the condition for the presence of the filling anomaly.

In a dD inversion-symmetric system, there are 2^d distinct Wyckoff positions W_i and inversion-invariant momenta $\boldsymbol{k}_i^{\text{inv}}$ which are left invariant under inversion symmetry:

$$
\{W_{i=1,\ldots,2^d}\} = \left\{ \sum_{l=1}^d x_l \boldsymbol{a}_l \,\middle|\, \forall\, x_l = 0, \frac{1}{2} \right\}, \tag{28}
$$

$$
\{\boldsymbol{k}_{i=1,\ldots,2^d}^{\text{inv}}\} = \left\{ \sum_{l=1}^d y_l \boldsymbol{G}_l \,\middle|\, \forall\, y_l = 0, \pi \right\}, \tag{29}
$$

where $\boldsymbol{a}$ and $\boldsymbol{G}$ are the lattice and reciprocal vectors, respectively, which satisfy $\boldsymbol{a}_i \cdot \boldsymbol{G}_j = 2\pi \delta_{ij}$. We label W_i and $\boldsymbol{k}_i^{\text{inv}}$ as follows:

$$
W_{i=1+\sum_{j=1}^d 2^{j-1}\sigma_j} = \frac{1}{2}(\sigma_1, \sigma_2, \ldots \sigma_d), \tag{30}
$$

$$
\boldsymbol{k}_{i=1+\sum_{j=1}^d 2^{j-1}\sigma_j}^{\text{inv}} = \pi(\sigma_1, \sigma_2, \ldots \sigma_d), \tag{31}
$$

where $\sigma = 0, 1$. More explicitly,

$$
\begin{aligned}
W_1 &= (0, 0, \ldots, 0), \quad W_2 = \left(\tfrac{1}{2}, 0, \ldots, 0\right), \\
W_3 &= \left(0, \tfrac{1}{2}, \ldots, 0\right), \quad W_4 = \left(\tfrac{1}{2}, \tfrac{1}{2}, \ldots, 0\right), \\
&\ldots, W_{2^d} = \left(\tfrac{1}{2}, \tfrac{1}{2}, \ldots, \tfrac{1}{2}\right)
\end{aligned}
\tag{32}
$$

and, similarly,

$$
\begin{aligned}
\boldsymbol{k}_1^{\text{inv}} &= (0, 0, \ldots, 0), \quad \boldsymbol{k}_2^{\text{inv}} = (\pi, 0, \ldots, 0), \\
\boldsymbol{k}_3^{\text{inv}} &= (0, \pi, \ldots, 0), \quad \boldsymbol{k}_4^{\text{inv}} = (\pi, \pi, \ldots, 0), \\
&\ldots, \boldsymbol{k}_{2^d}^{\text{inv}} = (\pi, \pi, \ldots, \pi).
\end{aligned}
\tag{33}
$$

A. Mapping between Wannier states and parity configurations

Any given parity configuration $\mathcal{B}$ can be mapped to linear combinations of inversion-symmetric Wannier states $w_\xi(W)$. Here, $w_\xi(W)$ denotes a Wannier state with parity ξ localized at the Wyckoff position W. At the momentum $\boldsymbol{k}^{\mathrm{inv}}$ in the Brillouin zone, a state with parity $\xi \exp(2i\boldsymbol{k}^{\mathrm{inv}} \cdot W)$ can be induced by $w_\xi(W)$. For example, s and p orbitals localized at W_1 correspond to $w_+(W_1)$ and $w_-(W_1)$, respectively. Let us note that it is sufficient to consider symmetric Wyckoff positions W_i only. When a orbital is located at generic point $W \neq -W$, its partner must also be located at $-W$ because of inversion symmetry. Then, the symmetric and antisymmetric combinations of the two states give s and p orbitals at a certain symmetric Wyckoff position, say W_i. It is worth noting that this s and p orbital pair located at W_i can be deformed adiabatically to another Wyckoff position, say W_j, without breaking inversion symmetry. Such an adiabatic deformation of Wannier states can be referred as "Wannier gauge redundancy."

For a given Wannier state representation $\bigoplus_{W,\xi} \mu_{W,\xi} w_\xi(W)$, there is a corresponding parity configuration $\mathcal{B}$ in the Brillouin zone. The equivalence relation between them [17,18,20,21,23,25,40,41,60] is denoted as

$$\mathcal{B} \Leftrightarrow \bigoplus_{W,\xi} \mu_{W,\xi} w_\xi(W). \tag{34}$$

Here, $\mu_{W,\xi}$ is a rational number [11], i.e., $\mu_{W,\xi} \in \mathbb{Q}$, and dictates how many $w_\xi(W)$ are superposed in a given atomic configuration. For later convenience, we denote a parity configuration of $N_\mathcal{B}$ bands in dD that satisfies $n_-(\Gamma = \boldsymbol{k}_1^{\mathrm{inv}}) = n_+(\boldsymbol{k}^{\mathrm{inv}} \neq \Gamma) = N_\mathcal{B}$ as $\mathcal{B}_\Gamma(d, N_\mathcal{B})$. Namely, all occupied bands have odd parity at the Γ point whereas they have even parity at the other $\boldsymbol{k}^{\mathrm{inv}}$ in $\mathcal{B}_\Gamma(d, N_\mathcal{B})$.

The equivalence relation (34) is not one to one since there is an ambiguity in choosing Wannier states, that is, the Wannier gauge redundancy:

$$\bigoplus_{\xi=\pm} w_\xi(W) = \bigoplus_{\xi=\pm} w_\xi(W'). \tag{35}$$

This follows from the fact that $w_{+1}(W) \oplus w_{-1}(W)$ gives $n_+(\boldsymbol{k}^{\mathrm{inv}}) = n_-(\boldsymbol{k}^{\mathrm{inv}}) = 1$ for any W and $\boldsymbol{k}^{\mathrm{inv}}$.

According to the recent studies [10,11,16], a parity configuration $\mathcal{B}$ can be classified into three distinct classes depending on the type of $\mu_{W,\xi} \in \mathbb{Q}$. (i) $\mathcal{B}$ is diagnosed to be a stable topological phase when the set of $\mu_{W,\xi}$ includes a fraction. Adding trivial bands corresponds to $\Delta\mu_{W,\xi} \in \mathbb{Z}$, and thus it does not change the fractional part of μ_W. (ii) $\mathcal{B}$ is diagnosed to be a fragile topological phase when the set of $\mu_{W,\xi}$ includes at least one negative integer in any fixed Wannier gauge. (iii) $\mathcal{B}$ is diagnosed to be an (obstructed) atomic phase when all $\mu_{W,\xi}$ are integers greater than or equal to 0 in at least one fixed Wannier gauge.

For example, (i) $\mathcal{B}_\Gamma(2, 1)$ is equivalent to $\ominus\frac{1}{2}p(W_1) \oplus \frac{1}{2}p(W_2) \oplus \frac{1}{2}p(W_3) \oplus \frac{1}{2}p(W_4)$. Because of the fractional coefficients of p orbitals, the phase is diagnosed to be a stable topological phase. In fact, according to the recent symmetry indicator analysis, this phase is characterized by an odd Chern number [11,78], which indicates its stable band topology. (ii) $\mathcal{B}_\Gamma(2, 2)$ is equivalent to $\ominus p(W_1) \oplus p(W_2) \oplus p(W_3) \oplus$

$p(W_4)$. The negative coefficient of $p(W_1)$ cannot be removed in any Wannier gauge, and thus the phase is diagnosed to be a fragile topological phase. (iii) $\mathcal{B} \Leftrightarrow s(W_1) \ominus s(W_2) \oplus 2p(W_1)$ has a negative coefficient of $s(W_2)$, and seems to be a fragile topological phase. However, $\mathcal{B} \Leftrightarrow p(W_1) \oplus p(W_2)$ up to the Wannier gauge redundancy $s(W_1) \oplus p(W_1) = s(W_2) \oplus p(W_2)$, thus $\mathcal{B}$ is diagnosed to be an atomic phase.

Now, let us compare the real-space data $\{w_\xi(W)\}$ and the momentum-space data $\{n_\xi(\boldsymbol{k}^{\mathrm{inv}})\}$. There are 2^{d+1} possible types of $w_\xi(W)$, counting the number of Wyckoff positions with two different parities. But, only $(2^d + 1)$ of them are independent due to the Wannier gauge redundancy shown in Eq. (35). Namely, the Wannier gauge redundancy $s(W_1) \oplus p(W_1) = s(W_2) \oplus p(W_2) = \cdots = s(W_{2^d}) \oplus p(W_{2^d})$ give $(2^d - 1)$ constraint equations. Taking into account this, one can write $(2^d + 1)$ numbers invariant under the Wannier gauge redundancy as

$$\{n_{\mathrm{occ}}, \nu_{W_1}, \nu_{W_2}, \ldots, \nu_{W_{2^d}}\}, \tag{36}$$

where $\nu_W = \mu_{W,-} - \mu_{W,+}$. Note that $\mu_{W,-}$ and $\mu_{W,+}$ change by the same amount under the Wannier gauge redundancy, thus, ν_W can serve as a topological invariant. This approach was introduced in Ref. [45] for rotation-symmetric ($C_{n=2,3,4,6}$) insulators and ν_W indices were found explicitly. However, the possibility to interpret ν_W indices as the indicators for fragile topological phases was not appreciated. We show that inversion-symmetric insulators can be completely classified in terms of the indices in Eq. (36), which can also be used for the diagnosis of fragile topological phases.

On the other hand, the parity configuration $\mathcal{B}$ is characterized by 2^{d+1} integers

$$\{n_+(\boldsymbol{k}_1^{\mathrm{inv}}), n_-(\boldsymbol{k}_1^{\mathrm{inv}}), \ldots, n_+(\boldsymbol{k}_{2^d}^{\mathrm{inv}}), n_-(\boldsymbol{k}_{2^d}^{\mathrm{inv}})\}. \tag{37}$$

In an insulating phase, the number of occupied states n_{occ} is fixed to be $n_{\mathrm{occ}} = n_+(\boldsymbol{k}^{\mathrm{inv}}) + n_-(\boldsymbol{k}^{\mathrm{inv}})$ for all $\boldsymbol{k}^{\mathrm{inv}}$. This is called the compatibility relation [9–11]. Thus, $\mathcal{B}$ can be characterized by $(2^d + 1)$ independent integers. One canonical choice of these $(2^d + 1)$ integers is

$$\{n_{\mathrm{occ}}, n_-(\boldsymbol{k}_1^{\mathrm{inv}}) - n_+(\boldsymbol{k}_1^{\mathrm{inv}}), \ldots, n_-(\boldsymbol{k}_{2^d}^{\mathrm{inv}}) - n_+(\boldsymbol{k}_{2^d}^{\mathrm{inv}})\}, \tag{38}$$

including $n_-(\boldsymbol{k}_i^{\mathrm{inv}}) - n_+(\boldsymbol{k}_i^{\mathrm{inv}})$ with $i = 1, \ldots, 2^d$. Observing that $w_\xi(W)$ has the parity $\xi \exp(2i\boldsymbol{k}^{\mathrm{inv}} \cdot W)$ at $\boldsymbol{k}^{\mathrm{inv}}$, one can find a mapping between $\{\nu_W\}$ and $\{n_-(\boldsymbol{k}^{\mathrm{inv}}) - n_+(\boldsymbol{k}^{\mathrm{inv}})\}$ as

$$\begin{pmatrix} \nu_{W_1} \\ \nu_{W_2} \\ \nu_{W_3} \\ \vdots \\ \nu_{W_{2^d}} \end{pmatrix} = A_d \begin{pmatrix} n_-(\boldsymbol{k}_1^{\mathrm{inv}}) - n_+(\boldsymbol{k}_1^{\mathrm{inv}}) \\ n_-(\boldsymbol{k}_2^{\mathrm{inv}}) - n_+(\boldsymbol{k}_2^{\mathrm{inv}}) \\ n_-(\boldsymbol{k}_3^{\mathrm{inv}}) - n_+(\boldsymbol{k}_3^{\mathrm{inv}}) \\ \vdots \\ n_-(\boldsymbol{k}_{2^d}^{\mathrm{inv}}) - n_+(\boldsymbol{k}_{2^d}^{\mathrm{inv}}) \end{pmatrix}, \tag{39}$$

where the $2^d \times 2^d$ matrix A_d maps the real data $\{\nu_W\}$ and the momentum-space data $\{n_-(\boldsymbol{k}^{\mathrm{inv}}) - n_+(\boldsymbol{k}^{\mathrm{inv}})\}$, and its components are given by

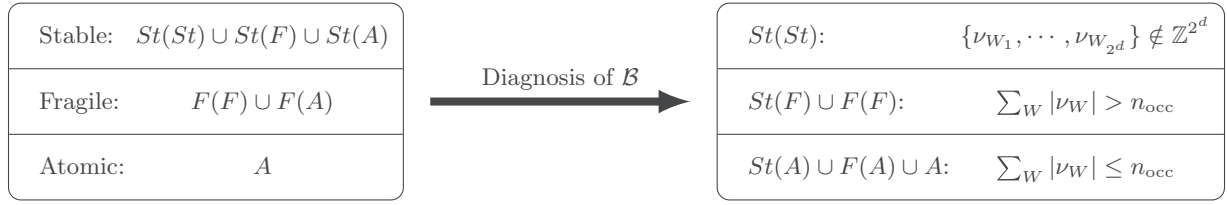$$[A_d]_{ij} = \frac{1}{2^d} \exp(2i\boldsymbol{k}_i^{\mathrm{inv}} \cdot W_j). \tag{40}$$

FIG. 5. Diagnosis of band topology. Left: all sets of possible band topology are divided into three sets $[\Omega_{i=1,2,3}] = \cup_{j\leqslant i}\Omega_i(\Omega_j)$ where Ω_1, Ω_2, and Ω_3 denote the atomic, fragile topological, and stable topological phases, respectively. Notation $\Omega_i(\Omega_j)$ means that the phase is diagnosed to be Ω_j only with the symmetry data while the phase is actually Ω_i. Right: these phases are rearranged into three sets $\cup_{j\geqslant i}\Omega_i(\Omega_j)$, and these are diagnosed in terms of ν_W indices.

Also, A_d satisfies the following relations:

$$A_d^{-1} = 2^d A_d, \quad A_d^T = A_d, \quad \sum_{i=1}^{2^d}[A_d]_{ij} = \delta_{j,1}. \quad (41)$$

For example, $A_{d=2}$ is given by

$$A_2 = \frac{1}{4}\begin{pmatrix} +1 & +1 & +1 & +1 \\ +1 & -1 & +1 & -1 \\ +1 & +1 & -1 & -1 \\ +1 & -1 & -1 & +1 \end{pmatrix}, \quad (42)$$

and the expressions for $\nu_{W_{i=1,2,3,4}}$ are the same as those in Ref. [45]. From the fact that $n_\pm(\boldsymbol{k}^{\mathrm{inv}})$ must be a non-negative integer, the possible sets of $\{\nu_W\}$ are restricted. The most fundamental restriction is that $2^d|\sum_{j=1}^{2^d}[A_d]_{ij}\nu_{W_j}|$ must be an integer less than or equal to n_{occ}. Below, we list some useful restrictions and inequalities derived from this:

$$|\nu_{W_i}| \leqslant n_{\mathrm{occ}}, \quad |\nu_{W_i} \pm \nu_{W_{j\neq i}}| \leqslant n_{\mathrm{occ}}, \quad \left|\sum_W \nu_W\right| \leqslant n_{\mathrm{occ}},$$

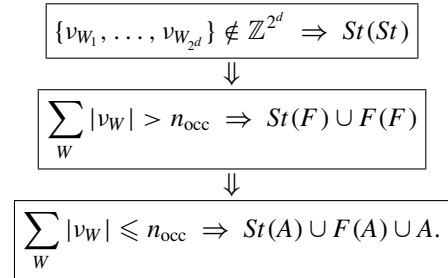$$2^{d-1}\nu_{W_i} \in \mathbb{Z}, \quad 2^{d-2}(\nu_{W_i} \pm \nu_{W_j}) \in \mathbb{Z}. \quad (43)$$

For example,

$$\{\nu_{W_1}, \ldots, \nu_{W_4}\} = \{\tfrac{1}{2}, 0, -\tfrac{1}{2}, 0\} \text{ or } \{-1, 0, 1, 0\} \quad (44)$$

cannot be realized when $n_{\mathrm{occ}} = 1$ in 2D. The first set $\{\frac{1}{2}, 0, -\frac{1}{2}, 0\}$ is forbidden due to $2^{d-2}(\nu_{W_i} \pm \nu_{W_{j\neq i}}) \in \mathbb{Z}$ while the second set $\{-1, 0, 1, 0\}$ is forbidden because of $|\nu_{W_i} \pm \nu_{W_j}| \leqslant n_{\mathrm{occ}}$. The properties of A_d and ν_W, and the derivation of the equations from Eqs. (39) to (43), are shown in Appendix B.

B. Diagnosis of fragile topology

Now, we provide an efficient scheme for diagnosing the band topology in terms of $\{n_{\mathrm{occ}}, \nu_{W_1}, \ldots, \nu_{W_{2^d}}\}$. Any given inversion-symmetric phase is an element of $[\tilde{\Omega}]$ where $\Omega = A, F, St$. Here, $[A]$, $[F]$, and $[St]$ denote a set of atomic, fragile topological, stable topological phases, respectively. Each set can be partitioned into mutually exclusive subsets: $[St] = St(St) \cup St(F) \cup St(A)$, $[F] = F(F) \cup F(A)$, and $[A] = A(A)$. The notation $\Omega_i(\Omega_j)$ means that the given inversion-symmetric phase belongs to Ω_i, but its parity configuration $\mathcal{B}$ predicts it to be in the set Ω_j. We denote $A(A) = A$ for simplicity.

The diagnosis of stable topological phases has been well established in 2D and 3D in terms of symmetry indicators [11,12]. However, an efficient method to diagnose fragile phases has not been established. Here, we propose one efficient scheme. The procedure for diagnosing inversion-symmetric insulators proceeds as follows. (i) $St(St)$ is diagnosed by a criterion $\{\nu_{W_1}, \ldots, \nu_{W_{2^d}}\} \notin \mathbb{Z}^{2^d}$ where $\mathbb{Z}^{2^d}$ indicates the set of 2^d integers. (ii) A fragile phase can be diagnosed by a criterion $\sum_W |\nu_W| > n_{\mathrm{occ}}$, which can be obtained by the fact that an atomic phase must satisfy $\sum_W |\nu_W| \leqslant n_{\mathrm{occ}}$. Thus, a phase which satisfies $\sum_W |\nu_W| > n_{\mathrm{occ}}$ belongs to $St(F) \cup F(F)$. (iii) A phase which satisfies $\sum_W |\nu_W| \leqslant n_{\mathrm{occ}}$ cannot be distinguished from atomic phases, so it belongs to $St(A) \cup F(A) \cup A$. This two-step diagnosis procedure is summarized in the following diagram, and also in Fig. 5:

$$\boxed{\{\nu_{W_1}, \ldots, \nu_{W_{2^d}}\} \notin \mathbb{Z}^{2^d} \;\Rightarrow\; St(St)}$$
$$\Downarrow$$
$$\boxed{\sum_W |\nu_W| > n_{\mathrm{occ}} \;\Rightarrow\; St(F) \cup F(F)}$$
$$\Downarrow$$
$$\boxed{\sum_W |\nu_W| \leqslant n_{\mathrm{occ}} \;\Rightarrow\; St(A) \cup F(A) \cup A.}$$

Let us emphasize that our diagnosis procedure goes beyond the diagnosis method proposed previously for stable topological phases [11,13] in that our approach can diagnose even fragile topological phases. The criterion for fragile topological and atomic phases is derived in Appendix A. It is worth noting that our classification of inversion-protected fragile TIs is complete. The band topology of class A insulators is fully characterized by inversion parities at high-symmetry points and all the Chern numbers defined in the Brillouin zone [9,11,15]. Since the Chern numbers are stable topological invariants, fragile TIs and atomic insulators can be fully characterized by using only inversion parities. This implies that $F(A)$ is an empty set and $[F] = F(F)$.

C. Results of diagnosis

We tabulate how many parity configurations are diagnosed to be atomic, fragile topological, and stable topological phases. We first fix the number of occupied bands n_{occ}. Then, we apply the diagnosis procedure to all possible parity configurations, and count $N(A)$, $N(F)$, and $N(St)$, which are the

TABLE IV. Results of the parity configuration diagnosis in 2D. When n_{occ} is sufficiently large, $N(A)$, $N(F)$, and $N(St)$ approach to $\frac{1}{3}N_{tot}$, $\frac{1}{6}N_{tot}$, and $\frac{1}{2}N_{tot}$. At least, two-thirds of parity configurations are topologically nontrivial.

n_{occ}	N_{tot}	$N(A)$	$N(F)$	$N(St)$
1	16	8	0	8
2	81	33	8	40
3	256	96	32	128
4	625	225	88	312
5	1296	456	192	648
6	2401	833	368	1200
7	4096	1408	640	2048
8	6561	2241	1040	3280
9	10000	3400	1600	5000
10	14641	4961	2360	7320
$n_{occ} \to \infty$	$(n_{occ}+1)^4$	$\frac{1}{3}N_{tot}$	$\frac{1}{6}N_{tot}$	$\frac{1}{2}N_{tot}$

number of parity configurations diagnosed to be atomic, fragile topological, and stable topological phases, respectively. The sum of $N(A)$, $N(F)$, and $N(St)$ must be N_{tot}. Here, N_{tot} is the number of all possible parity configurations and is given by $(n_{occ}+1)^{2^d}$. Let us note that when the ordering of energy bands is neglected, there can be $0, 1, \ldots, n_{occ}$ states with odd parity at each inversion-invariant momentum, so there are $(n_{occ}+1)^{2^d}$ possible parity configurations.

In 2D, as shown in Table IV, $N(A)$, $N(F)$, and $N(St)$ are given by $\frac{1}{3}N_{tot}$, $\frac{1}{6}N_{tot}$, and $\frac{1}{2}N_{tot}$, respectively, when n_{occ} is sufficiently large. Namely, at least, one-sixth (one-half) of parity configurations are predicted to be fragile (stable) topological phases. On the other hand, in 3D, most of parity configurations are diagnosed to be stable topological phases as shown in Table V. When n_{occ} is sufficiently large, we find that $N(A)$ is given by $\frac{1}{315}N_{tot}$ but it is difficult to determine the exact values of $N(F)$ and $N(St)$ in the $n_{occ} \to \infty$ limit. However, from the values of $N(A)$, $N(F)$, and $N(St)$ for various n_{occ}, we conjecture that $N(F) = \frac{283}{10080}N_{tot}$ and $N(St) = \frac{31}{32}N_{tot}$,

which implies that only about 3% of parity configurations are diagnosed to be fragile topological phases.

The implications of Tables IV and V are as follows. First, there is no fragile TI with $n_{occ} = 1$ in any dimensions [81]. This follows from the second inequality in Eq. (43), $|\nu_{W_i} \pm \nu_{W_j}| \leqslant n_{occ}$. Second, a layer stacking of 2D fragile TIs with negligible interlayer coupling gives rise to fragile TIs in higher dimensions. For instance, in 2D, there are eight fragile TIs with $n_{occ} = 2$. The ν_W indices of these fragile TIs are given by $\{\mp 1, \pm 1, \pm 1, \pm 1\}$ and its permutations. With these representative ν_W indices, the fragile TIs with $n_{occ} = 2$ in 3D can be constructed in the following way. Let us consider $\{\nu_W\} = \{-1, 1, 1, 1, 0, 0, 0, 0\}$ as an example of indices for a 3D insulator. These indices correspond to a 3D insulator obtained by a stacking of 2D layers with $\{\nu_W\} = \{-1, 1, 1, 1\}$, which satisfy $\boldsymbol{d} \cdot (x, y, z) = 0$ (mod 1) where $\boldsymbol{d} = (0, 0, 1)$ and (x, y, z) denotes the position on the 2D layers. Since there are 14 independent 2D layers that satisfy $\boldsymbol{d} \cdot (x, y, z) = 0$ or $\frac{1}{2}$ (mod 1) where $\boldsymbol{d} = (1, 0, 0), (0, 1, 0), (0, 0, 1), (1, 1, 0), (1, 0, 1), (0, 1, 1), (1, 1, 1)$, we have $8 \times 14 = 112$ fragile TIs with $n_{occ} = 2$ in 3D. Also, we note that the 1344 fragile TIs with $n_{occ} = 3$ in 3D can be obtained by adding a trivial band to 112 fragile TIs with $n_{occ} = 2$. There are 16 ways to add a trivial band, which is one of $s(W_i)$ and $p(W_i)$ for $i = 1, \ldots, 8$. However, four of them trivialize a 3D fragile TI with $n_{occ} = 2$. Accordingly, we have $112 \times 12 = 1344$ fragile TIs with $n_{occ} = 3$ in 3D. From the layer-stacking picture, we conclude that the minimal number of occupied bands to have the fragile topology is two in any dimension. This process for obtaining a higher-dimensional fragile TI by layer stacking 2D fragile TIs can be described by using a pumping process in momentum space as discussed in Sec. VII. Third, fragile topology can be trivialized under the doubling of the unit cell. For instance, let us consider the doubling of the unit cell in all spatial directions. In this case, all the symmetric Wyckoff positions except W_{2^d} form inversion-symmetric pairs at generic positions, thus, the resulting ν_W is composed of 2^d $\nu_{W_{2^d}}$ of the original system, that is, $\nu_{W_i} = \nu_{W_{2^d}}$ for $i = 1, \ldots, 2^d$. If we repeat the same

TABLE V. Results of the parity configuration diagnosis in 3D. When n_{occ} is sufficiently large, $N(A)$ is $\frac{1}{315}N_{tot}$. As for $N(F)$ and $N(St)$, although their exact numbers in the $n_{occ} \to \infty$ limit are not known, considering their n_{occ} dependence, we conjecture that $N(F) = \frac{283}{10080}N_{tot}$ and $N(St) = \frac{31}{32}N_{tot}$ in the large-n_{occ} limit. In contrast to 2D, the majority of parity configurations are stable topological phases. Here, $z_4 = -4\nu_{W_1}$ denotes the $\mathbb{Z}_4$ symmetry indicator [11,13,43] for inversion symmetry. The relation between symmetry indicators and ν_W indices is discussed in Appendix C. Let us also note that stable topological phases are Weyl semimetal when z_4 is odd [79,80].

| n_{occ}	N_{tot}	$N(A)$	$N(F)$	$N(St)$			
				$z_4 = 0$	$z_4 = 1$	$z_4 = 2$	$z_4 = 3$
1	256	16	0	56	64	56	64
2	6561	129	112	1400	1640	1640	1640
3	65536	704	1344	14336	16384	16384	16384
4	390625	2945	9536	85176	97656	97656	97656
5	1679616	10128	42368	367416	419904	419896	419904
6	5764801	29953	151248	1260000	1441200	1441200	1441200
7	16777216	78592	445696	3670016	4194304	4194304	4194304
8	43046721	187137	1160944	9413600	10761680	10761680	10761680
9	100000000	411280	2713728	21875000	25000000	24999992	25000000
10	214358881	845185	5859936	46884600	53589720	53589720	53589720

(a)   (b)
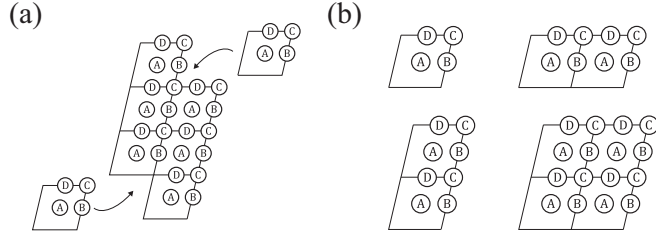
FIG. 6. Filling anomaly and the building blocks of finite-size systems. Attaching or detaching the unit cells to the boundary of the finite-size inversion-symmetric insulators does not change the number of Wannier centers at the boundary modulo two, N_∂. Four Wyckoff positions $W_{1,2,3,4}$ are denoted as A, B, D, and C, respectively. (a) A process changing N_∂ by $\sum_\xi (\mu_{B,\xi} + \mu_{C,\xi} + \mu_{D,\xi}) - \sum_\xi (\mu_{B,\xi} + 3\mu_{C,\xi} + \mu_{D,\xi}) = -2 \sum_\xi \mu_{C,\xi} = 0$ modulo 2. Note that $\nu_W = \mu_{W,-} - \mu_{W,+} = \sum_\xi \mu_{W,\xi}$ modulo 2. (b) For any finite-size system, the corresponding building block is determined uniquely. In 2D, there are four building blocks. The building block corresponding to the geometry depicted in (a) is 2×2 unit cells. The presence (absence) of the filling anomaly is well defined only when $\nu_{B,C,D}$ are odd (even) integers simultaneously.

doubling process, the number of occupied bands increases while $\sum_W |\nu_W| = 2^d |\nu_{W_{2^d}}|$ is fixed. Then, the result of the diagnosis for fragile TI, $\sum_W |\nu_W| > n_{\text{occ}}$, can change to $\sum_W |\nu_W| \leqslant n_{\text{occ}}$. Finally, when $n_-(\boldsymbol{k}_i^{\text{inv}})$ for $i = 1, \ldots 2^d$ are less than 2^{d-1}, at least one ν_W index among $\nu_{W_{2,3,\ldots,2^d}}$ is zero, i.e., $\prod_{i=2}^{2^d} \nu_{W_i} = 0$. We have verified that this is true for arbitrary number of occupied bands in 2D and 3D, and we expect that this is also true in any dimension $d > 3$.

D. Filling anomaly in general dimensions

In this section, we propose a condition for the presence or absence of the filling anomaly, independent of the geometry of finite-size systems. First, we observe that, for a given finite-size system, the number of the Wannier centers at the boundary modulo two, N_∂, is invariant under an attaching or a detaching of unit cells to the boundary in an inversion-symmetric way. This is depicted in Fig. 6(a). Second, there are 2^d building blocks for the finite-size systems in dD. Any finite-size inversion-symmetric insulators can be constructed by attaching unit cells at the boundary of these building blocks. For example, in 2D, there are four building blocks composed of 1×1, 2×1, 1×2, and 2×2 unit cells [see Fig. 6(b)]. For the building block made of the 1×1 unit cell, N_∂ is given by $\nu_{W_2} + \nu_{W_3} + \nu_{W_4}$ modulo 2. However, in the case of the building block composed of 1×2 unit cells, N_∂ is given by $2\nu_{W_2} + \nu_{W_3} + 2\nu_{W_4}$ modulo 2. Since the filling anomaly exists when N_∂ is odd and N_∂ depends on the building blocks, the presence or absence of the filling anomaly depends on the type of these building blocks for given $\nu_{W_{2,3,4}}$. Investigating all the building blocks in dD, we conclude that ν_{W_i} for $i = 2, 3, \ldots, 2^d$ must be odd integers (even integers) at the same time to have (not to have) the filling anomaly independent of the type of the building blocks. Physically, this condition is equivalent to the vanishing polarization $\boldsymbol{P} = \sum_W W\nu_W = (0, 0)$ in 2D. In the rest of this paper, we
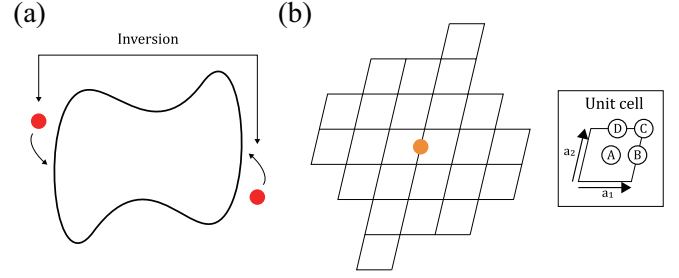
(a)   (b)

FIG. 7. Schematic figures describing how the net parity is defined for inversion-symmetric insulators without gapless boundary states. (a) Localized degrees of freedom, red dots, added to the boundary in an inversion-symmetric way. Their symmetric and antisymmetric combinations generate s and p orbitals, and thus $\mathcal{I}$ does not change. (b) A finite-size system with an open boundary in which the Wyckoff position B is at the inversion center, the orange dot. In this case, the net parity $\mathcal{I}$ is given by ν_B.

focus on the cases where the filling anomaly is well defined independent of the type of the building blocks.

The condition for the presence of the filling anomaly puts a constraint to the number of occupied bands. As at least one ν_W index among $\nu_{W_{2,3,\ldots,2^d}}$ is zero when $n_-(\boldsymbol{k}_i^{\text{inv}})$ for $i = 1, \ldots, 2^d$ are less than 2^{d-1}, the filling anomaly occurs only when $n_{\text{occ}} \geqslant 2^{d-1}$. For atomic insulators, the number of occupied bands must be greater than or equal to $(2^d - 1)$ in order to have all $\nu_{W_{2,3,\ldots,2^d}}$ as odd integers. Thus, there are 2^{2^d-1} minimal atomic insulators with the filling anomaly, and they have $\{\nu_W\} = \{0, \pm 1, \pm 1, \pm 1\}$ in 2D and $\{0, \pm 1, \pm 1, \pm 1, \pm 1, \pm 1, \pm 1, \pm 1\}$ in 3D. Here, all $\pm$ are independent. In contrast to atomic insulators, fragile TIs can have the filling anomaly when $n_{\text{occ}} \geqslant 2^{d-1}$. In other words, all insulators with the filling anomaly are fragile TIs when $2^{d-1} \leqslant n_{\text{occ}} \leqslant 2^d - 2$.

E. Net parity in open boundary

In this section, we discuss the net parity [52,63,64] of finite-size inversion-symmetric insulators without gapless boundary states, which generalizes the discussion in Sec. II B. For any inversion-symmetric insulator in dD which does not host gapless boundary states, the energy spectra of occupied and unoccupied states are well defined. In this case, the net parity of a finite-size system $\mathcal{I} = N_- - N_+$ in Eq. (10) characterizes the bulk band topology [52,63,64]. Here, $N_\pm$ denotes the number of occupied states with parity $\pm$. Now, we argue that $\mathcal{I}$ does not change if we add localized states at the boundary. For instance, when an electron is added to the boundary, its inversion partner also has to be added to preserve inversion symmetry as shown in Fig. 7(a). Then, the two electrons form a symmetric and an antisymmetric state. In this process, both N_+ and N_- increase by one, so $\mathcal{I}$ is invariant. The only way to change $\mathcal{I}$ is to add electrons at the inversion center. However, this cannot be done in an inversion-symmetric way. Therefore, $\mathcal{I}$ is the bulk topological invariant of inversion-symmetric systems that does not change as long as the bulk gap is preserved.

As discussed in Sec. II B, the net parity $\mathcal{I}$ is determined by the difference in the number of p and s orbitals at the center of

the system with an open boundary ΔN_{center}. When the system with an open boundary is inversion symmetric, its center must be one of the Wyckoff position W^*. Hence, ΔN_{center} is given by ν_{W^*}, and the net parity $\mathcal{I}$ is manifested as one of ν_W indices as shown in Fig. 7(b).

V. dD $(d+1)$th-ORDER TI AS MINIMAL FRAGILE TOPOLOGICAL INSULATOR WITH FILLING ANOMALY

In this section, we propose a minimal Dirac Hamiltonian for a fragile TI with filling anomaly. We assume that the number of occupied bands is $N_{\mathcal{B}}$, and all the occupied bands at the Γ point have negative parity while they have positive parity at all the other inversion-invariant momenta. Then, the corresponding parity configuration is $\mathcal{B}_\Gamma(d, N_{\mathcal{B}})$. Since such a parity configuration can be generated by a band inversion at Γ, starting from a trivial-parity insulator having only positive-parity states at inversion-invariant momenta, the state corresponding to $\mathcal{B}_\Gamma(d, N_{\mathcal{B}})$ can be described by a Dirac Hamiltonian.

The minimal dimension of the Dirac Hamiltonian can be determined by our diagnosis method of fragile topology as follows. First, we compute 2^d inversion indices $\{\nu_{W_1}, \ldots, \nu_{W_{2^d}}\}$ by using Eq. (39). Namely,

$$\begin{pmatrix} \nu_{W_1} \\ \nu_{W_2} \\ \nu_{W_3} \\ \vdots \\ \nu_{W_{2^d}} \end{pmatrix} = A_d \begin{pmatrix} N_{\mathcal{B}} \\ -N_{\mathcal{B}} \\ -N_{\mathcal{B}} \\ \vdots \\ -N_{\mathcal{B}} \end{pmatrix}, \tag{45}$$

which gives

$$\{\nu_{W_1}, \ldots, \nu_{W_{2^d}}\} = 2^{1-d} N_{\mathcal{B}}\{1 - 2^{d-1}, 1, 1, \ldots, 1\}. \tag{46}$$

To be a fragile topological phase, $\{\nu_W\}$ must be a set of integers and satisfy $\sum_W |\nu_W| > N_{\mathcal{B}}$. These conditions constrain $N_{\mathcal{B}}$ to be an integer multiple of 2^{d-1} in any dimensions greater than one. Thus, the minimal number of occupied bands for the fragile phase is $N_{\mathcal{B}} = 2^{d-1}$. Importantly, all ν_{W_i} for $i = 2, \ldots, 2^d$ are odd integers when $N_{\mathcal{B}} = 2^{d-1}$, and thus the filling anomaly exists. This is consistent with the result discussed in Sec. IV D where it is shown that the filling anomaly can occur when $n_{\text{occ}} \geqslant 2^{d-1}$. Also, we can find the equivalent representation for Wannier states corresponding to $\mathcal{B}_\Gamma(d, 2^{d-1})$ by using $\nu_W = \mu_{W,-} - \mu_{W,+}$ such as

$$\mathcal{B}_\Gamma(d, 2^{d-1}) \Leftrightarrow \bigoplus_{i=1}^{2^d} p(W_i) \ominus 2^{d-1} p(W_1). \tag{47}$$

Let us note three implications of Eqs. (46) and (47). First, the Wannier obstruction can be lifted after adding $(2^{d-1} - 1) p(W_1)$ orbitals. Second, $\mathcal{B}_\Gamma(d, N_{\mathcal{B}})$ with $N_{\mathcal{B}} < 2^{d-1}$ must have stable band topology since ν_W must be a fractional number. Third, an integer multiple of $\mathcal{B}_\Gamma(d, 2^{d-1})$ retains the fragile topology since multiplying Eq. (46) by an integer does not change the relevant inequality, i.e., $\sum_W |\nu_W| > n_{\text{occ}}$.

In Sec. III A, it is shown that the Dirac Hamiltonian for a class A dD kth-order TI is expressed by $2^{\frac{d+k-1}{2}} \times 2^{\frac{d+k-1}{2}}$ gamma matrices. Hence, the Dirac Hamiltonian correspond-
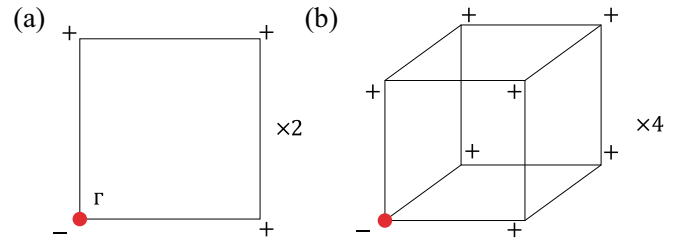

FIG. 8. Parity configurations for dD $(d+1)$th-order TIs. (a) $\mathcal{B}_\Gamma(2, 2)$ for a 2D third-order TI. (b) $\mathcal{B}_\Gamma(3, 4)$ for a 3D fourth-order TI.

ing to $\mathcal{B}_\Gamma(d, 2^{d-1})$ can describe a dD $(d+1)$th-order TI. For example, the Dirac Hamiltonian relevant to $\mathcal{B}_\Gamma(2, 2)$ describes a 2D third-order TI, and similarly, the Dirac Hamiltonian relevant to $\mathcal{B}_\Gamma(3, 4)$ describes a 3D fourth-order TI. The corresponding parity configurations are shown in Fig. 8. When the number of occupied states is greater than 2^{d-1}, the corresponding Dirac Hamiltonian describes a dD kth-order TI with $k > (d+1)$. As discussed above, all dD kth-order TIs with $k > d$ have fragile band topology.

In Secs. V A and V B, we examine the charge accumulation in the dD $(d+1)$th-order TI and establish the bulk-boundary correspondence, which can be viewed as 2D and 3D generalizations of the idea discussed in Sec. II A.

Before we proceed, let us comment on the case where the occupied states with negative parity are distributed over the multiple inversion-invariant momenta. In this case, the minimal number of occupied bands to have fragile topology is two in any dimensions which is smaller than 2^{d-1} for $d > 2$ (see Sec. IV C). However, these insulators cannot have the filling anomaly unless the number of occupied bands is greater than or equal to 2^{d-1} as discussed in Sec. IV D. In Appendix D, we discuss how an odd number of band inversions corresponding to the dD $(d+1)$th-order Dirac Hamiltonian generates the filling anomaly.

A. Tight-binding model

First, we define 4×4 gamma matrices $\Gamma_{n=1,\ldots,5}$ and 8×8 gamma matrices $\check{\Gamma}_{m=1,\ldots,7}$ in order to construct the tight-binding models for class A 2D third-order and 3D fourth-order TIs protected by inversion symmetry. We choose that Γ_n and $\check{\Gamma}_n$ with an even (odd) n are real (imaginary). For example, $\{\Gamma_1, \ldots, \Gamma_5\} = \{\tau_x\sigma_x, \tau_x\sigma_y, \tau_x\sigma_z, \tau_y\sigma_0, \tau_z\sigma_0\}$ and $\{\check{\Gamma}_1, \ldots, \check{\Gamma}_7\} = \{\mu_x\tau_x\sigma_x, \mu_x\tau_x\sigma_y, \mu_x\tau_x\sigma_z, \mu_x\tau_y\sigma_0, \mu_x\tau_z\sigma_0, \mu_y\tau_0\sigma_0, \mu_z\tau_0\sigma_0\}$.

Now, we discuss how the boundary mass terms can be introduced in lattice models. Following [46,52], we briefly review the mechanism for generating the boundary mass terms from symmetric perturbations to the bulk Hamiltonian. An inversion-symmetric Dirac Hamiltonian without any perturbation is

$$\mathcal{H}_0(\boldsymbol{k}) = \sum_{i=1}^d k_i \Gamma_i + \lambda \mathcal{M}, \tag{48}$$

$$I\mathcal{H}_0(\boldsymbol{k})I^{-1} = \mathcal{H}_0(-\boldsymbol{k}), \tag{49}$$

where I denotes the operator for inversion symmetry. Inversion-symmetric perturbation H_1 is given by

$$H_1 = i \sum_{i=1}^{d} \sum_{a=1}^{d} \Delta_{i,a} \Gamma_i M_a \mathcal{M}, \tag{50}$$

where $M_a = -I M_a I^{-1}$ with $a = 1, \ldots, d$.

After projection to the boundary, H_1 becomes

$$P_+(\boldsymbol{r}) H_1 P_+(\boldsymbol{r}) = \sum_{i=1}^{d} \sum_{a=1}^{d} \Delta_{i,a} \, \boldsymbol{n}_{r,i} \tilde{M}_a, \tag{51}$$

where $\tilde{M}_a = M_a P_+(\boldsymbol{r})$. Then, one can identify the boundary mass terms as $m_{a,r} = \sum_{i=1}^{d} \Delta_{i,a} \boldsymbol{n}_{r,i}$. Since $m_{a,r}$ is proportional to the surface normal vector $\boldsymbol{n}_r$, $m_{a,r} = -m_{a,-r}$ is naturally implemented. Finally, the lattice regularization with the substitution $k_i \to \sin k_i$ and $\lambda \to -(d - \lambda - \sum_{i=1}^{d} \cos k_i)$ leads to the bulk Hamiltonian

$$H(\boldsymbol{k}) = \sum_{i=1}^{d} \sin k_i \Gamma_i - \left(d - \lambda - \sum_{i=1}^{d} \cos k_i \right) \mathcal{M} + H_1, \tag{52}$$

which naturally contains the boundary mass terms whose explicit form appears after projection to the boundary. All the tight-binding models used in the paper are constructed by using this method. For example, the tight-binding models for class A 2D third-order and 3D fourth-order TIs are given by

$$H_{A(2,3)} = \sum_{i=1}^{2} \sin k_i \Gamma_i - \left(2 - \lambda - \sum_{i=1}^{2} \cos k_i \right) \Gamma_5$$
$$+ i \sum_{i=1}^{2} \sum_{a=3}^{4} \Delta_{i,a} \, \Gamma_i \Gamma_a \Gamma_5 \tag{53}$$

and

$$H_{A(3,4)} = \sum_{i=1}^{3} \sin k_i \check{\Gamma}_i - \left(3 - \lambda - \sum_{i=1}^{3} \cos k_i \right) \check{\Gamma}_7$$
$$+ i \sum_{i=1}^{3} \sum_{a=4}^{6} \check{\Delta}_{i,a} \, \check{\Gamma}_i \check{\Gamma}_a \check{\Gamma}_7. \tag{54}$$

For the tight-binding models defined above, since the boundary mass terms are given by $m_{a,r} = \sum_{i=1}^{d} \Delta_{i,a} \boldsymbol{n}_{r,i}$, the corresponding winding numbers are determined by the sign of the determinant of $\Delta_{i,a}$. For example,

$$w_1 = \frac{1}{2\pi} \oint d\theta \, (\varphi_1 \partial_\theta \varphi_2 - \varphi_1 \partial_\theta \varphi_2)$$
$$= \frac{1}{2\pi} \oint d\theta \, \frac{1}{m_1^2 + m_2^2} (m_1 \partial_\theta m_2 - m_1 \partial_\theta m_2)$$
$$= \text{Det}(\boldsymbol{\Delta}) \frac{1}{2\pi} \oint d\theta \, \frac{1}{m_1^2 + m_2^2}$$
$$= \frac{\text{Det}(\boldsymbol{\Delta})}{|\text{Det}(\boldsymbol{\Delta})|}$$
$$= \text{sgn}(\text{Det}(\boldsymbol{\Delta})), \tag{55}$$

where we use $m_{a=1,2} = \Delta_{1,a+2} \cos \theta + \Delta_{2,a+2} \sin \theta$ and

$$\frac{1}{2\pi} \oint d\theta \, \frac{1}{A \cos 2\theta + B \sin 2\theta + C} \tag{56}$$

$$= \text{sgn}(C - A) \frac{1}{\sqrt{C^2 - A^2 - B^2}}. \tag{57}$$

Similarly, we obtain $w_d = \text{sgn}(\text{Det}(\boldsymbol{\Delta}))$. Thus, the dD $(d+1)$th-order TI described by the relevant Dirac Hamiltonian is characterized by $w_d = 1 \pmod 2$.

B. Numerical calculations

In order to verify our theoretical prediction for charge accumulation at the boundary based on the continuum Dirac Hamiltonian, here we calculate the energy spectrum and the eigenstates of 2D third-order and 3D fourth-order TIs described by the lattice Hamiltonian $H_{A(2,3)}$ and $H_{A(3,4)}$, by considering various shapes of open boundaries. We choose square and disk geometries for 2D third-order TI, and cube and sphere geometries for 3D fourth-order TI. For numerical calculations, we choose $\Delta_{1,3} = 0.240$, $\Delta_{1,4} = -0.196$, $\Delta_{2,3} = -0.259$, $\Delta_{2,4} = -0.204$ for the 2D third-order TI, and $\check{\Delta}_{1,4} = -0.25$, $\check{\Delta}_{1,5} = 0.05$, $\check{\Delta}_{1,6} = 0.10$, $\check{\Delta}_{2,4} = -0.05$, $\check{\Delta}_{2,5} = 0.30$, $\check{\Delta}_{2,6} = -0.10$, $\check{\Delta}_{3,4} = 0.05$, $\check{\Delta}_{3,5} = -0.05$, $\check{\Delta}_{3,6} = 0.35$ for the 3D fourth-order TI. Then, $\text{sgn}(\text{Det}(\boldsymbol{\Delta})) = -1$ and $\text{sgn}(\text{Det}(\check{\boldsymbol{\Delta}})) = -1$ in both cases. Also, we assume that all sublattice sites are located at the unit-cell center for simplicity.

The energy spectra in Figs. 9(a) and 9(d) show that the number of occupied bands and that of unoccupied bands are different in the topological phase ($\lambda = 1$) whereas they are the same in the trivial phase ($\lambda = -1$). Figures 9(a) and 9(d) correspond to the 2D third-order TI and the 3D fourth-order TI, respectively. Moreover, when the states below (above) the gap are fully occupied (unoccupied) by adding an extra electron or hole to the half-filled system, we find that the extra charge accumulation is localized only at certain subregions of the boundary where the surface and the bulk mass terms change rapidly. More explicitly, it is found that the extra charge is localized at the corners of the system with a square or cube geometry, while the extra charge is spread over the whole boundary region when the system geometry has a disk or sphere shape, as shown in Fig. 9.

The difference in the number of occupied and unoccupied states in dD $(d+1)$th-order TIs can be understood by examining the change in the energy spectrum of a dD dth-order TI with chiral symmetry when chiral-symmetry-breaking perturbations are added. Specifically, a dD dth-order TI with chiral symmetry has two zero-energy modes related by inversion. Adding chiral-symmetry-breaking perturbation, the zero-energy modes are pushed either upward or downward until they are merged to the unoccupied or occupied states, leading to a dD $(d+1)$th-order TI without in-gap states. As long as inversion symmetry is preserved, the two in-gap states should be degenerate during this process. The filling anomaly requires that an extra electron or hole is added to the half-filled system, and the states below (above) the gap are fully occupied (unoccupied), to preserve inversion symmetry. Then, one can examine the extra charge accumulation relative to the half-filling (see Sec. II A for the related discussion in 1D second-order TIs).
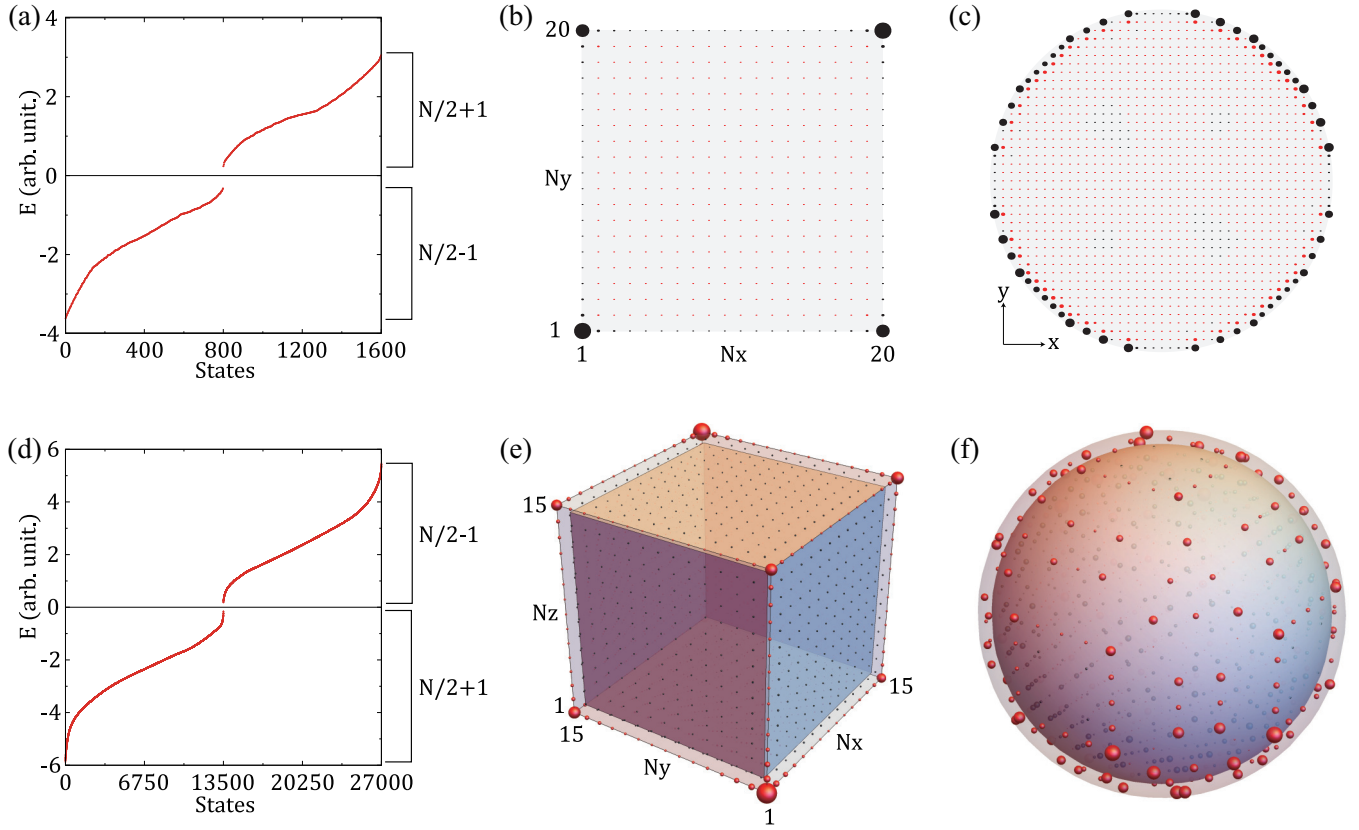
FIG. 9. Energy spectra and boundary charge accumulations of finite-size 2D third-order and 3D fourth-order TIs. (a) The energy spectrum of the lattice model for 2D third-order TIs in Eq. (53), in the topological phase ($\lambda = 1$). The system has the square geometry with 20×20 unit cells ($N = 1600$). (b) The extra charge accumulation $\Delta\rho(x, y)$ defined in Eq. (58) in the square geometry with 20×20 unit cells. (c) The extra charge accumulation $\Delta\rho(x, y)$ in the disk geometry. The radius of the disk (R) is equal to the length of 20.5 unit cells ($R = 20.5$). (d) The energy spectrum of the lattice model for 3D fourth-order TIs in Eq. (54), in the topological phase ($\lambda = 1$). The system has the cube geometry with $15 \times 15 \times 15$ unit cells ($N = 27\,000$). (e) The extra charge accumulation $\Delta\rho(x, y, z)$ in Eq. (61) in the cubic geometry with $15 \times 15 \times 15$ unit cells. (f) The extra charge accumulation $\Delta\rho(x, y, z)$ in the sphere geometry. The radius of the sphere (R) is equal to the length of 6.7 unit cells ($R = 6.7$). The orientation of the coordinate system is same as (e). In (b) and (c) and (e) and (f), the size of the dots and spheres dictates the absolute value of the accumulated or depleted charges. A black (red) dot and sphere denotes the depletion (accumulation). To enhance the visibility of the boundary, the cube with the edge length of 14.5 unit cells and the sphere with the radius of 6.2 unit cells are depicted in (e) and (f), respectively.

However, to understand the distribution of the extra charge accumulation at the boundary, we need the additional information of the induced current j_d^μ as explained in Sec. III C. To confirm the charge accumulation predicted by the induced current in Sec. III C, we first numerically solve the lattice model for a 2D third-order TI and compute the extra charge density $\Delta\rho(x, y)$ at the position (x, y) relative to the half-filling ($\rho_0 = 2$). In both the square and disk geometries, the extra charge density $\Delta\rho(x, y)$ is defined as

$$\Delta\rho(x, y) = \sum_{i=1}^{N_{\text{occ}}} |\psi_i(x, y)|^2 - \rho_0, \tag{58}$$

where $\psi_i(x, y)$ is the ith energy eigenstate and N_{occ} is the number of occupied states. Since total extra charge is -1 according to $\delta = \int j_1^0 = \text{sgn}(\text{Det}(\mathbf{\Delta})) = -1$, the total sum of $\Delta\rho(x, y)$ is equal to -1. Namely,

$$\sum_{x=1}^{N_x} \sum_{y=1}^{N_y} \Delta\rho(x, y) = -1, \tag{59}$$

where N_x and N_y denote the number of lattice sites in the x and y directions, respectively.

In the case of the square geometry, the extra charge is mostly localized at the corners as shown in Fig. 9(b). This is simply because the boundary mass terms vary abruptly near the corners. To demonstrate the spatial distribution of the extra charge accumulation, we divide the system into four quadrants. Then, we compare the total extra charge in each quadrant $Q_{i=1,2,3,4}^{\text{num.}}$ with the total induced charge density j_1^0 along the boundary of each quadrant Q_i. Because of inversion symmetry, $Q_1^{\text{num.}} = Q_3^{\text{num.}}$ and $Q_2^{\text{num.}} = Q_4^{\text{num.}}$. Explicitly, $Q_{1,2}^{\text{num.}}$ are defined as

$$Q_1^{\text{num.}} = \sum_{\frac{N_x}{2} < x} \sum_{\frac{N_y}{2} < y} \Delta\rho(x, y),$$

$$Q_2^{\text{num.}} = \sum_{x < \frac{N_x}{2}} \sum_{\frac{N_y}{2} < y} \Delta\rho(x, y). \tag{60}$$

According to the numerical data displayed in Table VI, the deviation of Q_i from $Q_i^{\text{num.}}$ is only about 1%. This is

TABLE VI. The extra charge accumulation in the 2D third-order TI. $Q_{i=1,2,3,4}^{\text{num.}}$ ($Q_{i=1,2,3,4}$) indicates the extra charge in the ith quadrant computed from the lattice model (from the induced charge of the continuum model). Note that $Q_1^{\text{num.}} = Q_3^{\text{num.}}$ and $Q_2^{\text{num.}} = Q_4^{\text{num.}}$ due to inversion symmetry, and similar relations hold for Q_i.

$Q_1^{\text{num.}}$	Q_1	$Q_2^{\text{num.}}$	Q_2
−0.282329	−0.284825	−0.217611	−0.215175

because when the bulk gap is sufficiently large, our formula for the induced current becomes more accurate due to the negligible contributions of higher-order terms in the derivative expansion. More detailed information about how the induced currents are computed is in Appendix G. On the other hand, in contrast to the case of the square geometry, the extra charge is spread over the whole boundary in the disk geometry as shown in Fig. 9(c). This delocalized charge accumulation is also consistent with the profile of $j_1^0(\theta)$ in Eq. (26).

Now, let us consider the 3D fourth-order TI. Both in the cube and sphere geometries, the extra charge density $\Delta\rho(x, y, z)$ at the position (x, y, z) compared to half-filling ($\rho_0 = 4$) is defined as

$$\Delta\rho(x, y, z) = \sum_{i=1}^{N_{\text{occ}}} |\psi_i(x, y, z)|^2 - \rho_0, \qquad (61)$$

where $\psi_i(x, y, z)$ is the ith energy eigenstate and N_{occ} is the number of occupied states. Also, the total accumulated charge is 1 according to $\delta = \int j_2^0 = -\text{sgn}(\text{Det}(\check{\mathbf{\Delta}})) = 1$, and thus the total sum of $\Delta\rho(x, y, z)$ is equal to 1. Namely,

$$\sum_{x=1}^{N_x} \sum_{y=1}^{N_y} \sum_{z=1}^{N_z} \Delta\rho(x, y, z) = 1, \qquad (62)$$

where $N_{i=x,y,z}$ denote the number of lattice sites in the i direction.

In the case of the cube geometry, the extra charge is mostly accumulated at the corners where the boundary mass terms vary rapidly, as shown in Fig. 9(e). To demonstrate the spatial distribution of the extra charge accumulation, we divide the system into eight octants. Then, we compare the total extra charge in each octant $Q_{i=1,...,8}^{\text{num.}}$ with the total induced charge density j_2^0 along the boundary of each octant Q_i. Inversion symmetry imposes $Q_1^{\text{num.}} = Q_7^{\text{num.}}$, $Q_2^{\text{num.}} = Q_8^{\text{num.}}$, $Q_3^{\text{num.}} = Q_5^{\text{num.}}$, and $Q_4^{\text{num.}} = Q_6^{\text{num.}}$. Explicitly, $Q_{1,2,3,4}^{\text{num.}}$ are defined as

$$Q_1^{\text{num.}} = \sum_{\frac{N_x}{2} < x} \sum_{\frac{N_y}{2} < y} \sum_{\frac{N_z}{2} < z} \Delta\rho(x, y, z),$$

$$Q_2^{\text{num.}} = \sum_{x < \frac{N_x}{2}} \sum_{\frac{N_y}{2} < y} \sum_{\frac{N_z}{2} < z} \Delta\rho(x, y, z),$$

$$Q_3^{\text{num.}} = \sum_{x < \frac{N_x}{2}} \sum_{y < \frac{N_y}{2}} \sum_{\frac{N_z}{2} < z} \Delta\rho(x, y, z),$$

$$Q_4^{\text{num.}} = \sum_{\frac{N_x}{2} < x} \sum_{y < \frac{N_y}{2}} \sum_{\frac{N_z}{2} < z} \Delta\rho(x, y, z). \qquad (63)$$

TABLE VII. The extra charge accumulation in the 3D fourth-order TI. $Q_{i=1,...,8}^{\text{num.}}$ ($Q_{i=1,...,8}$) indicates the extra charge in the ith octant computed from the lattice model (from the induced charge of the continuum model). Note that $Q_1^{\text{num.}} = Q_7^{\text{num.}}$, $Q_2^{\text{num.}} = Q_8^{\text{num.}}$, $Q_3^{\text{num.}} = Q_5^{\text{num.}}$, and $Q_4^{\text{num.}} = Q_6^{\text{num.}}$ due to inversion symmetry, and similar relations hold for Q_i.

$Q_1^{\text{num.}}$	Q_1	$Q_2^{\text{num.}}$	Q_2
0.116481	0.113613	0.203660	0.223673
$Q_3^{\text{num.}}$	Q_3	$Q_4^{\text{num.}}$	Q_4
0.089725	0.081586	0.090134	0.081127

The results of numerical calculations are displayed in Table VII, which shows that the deviation of Q_i from $Q_i^{\text{num.}}$ is about 10% . This is because our formula for the induced current in Eq. (22) get corrections from the higher-order terms when the bulk gap is small. When the bulk gap becomes larger, the deviation of Q_i from $Q_i^{\text{num.}}$ becomes smaller. In contrast to the case of the cube geometry, the extra charge is spread over the whole boundary in the sphere geometry as shown in Fig. 9(f). This delocalized charge accumulation is also consistent with the profile of $j_2^0(\theta, \phi)$ in Eq. (27). These numerical studies for 2D third-order and 3D fourth-order TIs in various open boundaries demonstrate the validity of the theory based on the induced current.

VI. WILSON LOOP OF FRAGILE TI

As we have shown in Secs. IV and V, the inversion parities completely characterize inversion-protected fragile topological insulators. On the other hand, there is an alternative powerful method, called the Wilson loop method [36,37,65–67,82], that can be used to diagnosis the Wannier obstruction. Here, we demonstrate the consistency between the inversion-parity analysis and the Wilson loop method to complete the analysis of the fragile band topology.

The Wilson loop is an operator defined along a periodic direction in the Brillouin zone, whose spectral winding along the other periodic direction indicates the Wannier obstruction on the 2D subspace in the Brillouin zone [29,65,82]. When the Wilson loop spectrum is gapped, the nested Wilson loop can be defined by treating the Wilson loop spectrum like the energy spectrum [36,37]. As shown below, the spectral winding of the Wilson loop and the nested Wilson loop spectra contain the essential characteristics of fragile TIs in three dimensions.

For completeness, in this section, we investigate the fragile topology of dD ($d + 1$)th-order TIs by using the Wilson loop method and show that the Wilson loop analysis is consistent with the diagnosis based on the parity eigenvalues. First, we observe that the Wilson loop spectrum of fragile TIs has a nonzero relative winding [66]. Then, we show that the relative winding of the Wilson loop can be unwound by adding appropriately chosen trivial bands. In dimensions greater than two, however, the number of additional orbitals required to trivialize the fragile topology does not match with the number of additional orbitals required to unwind the relative winding of the Wilson loop spectrum. We find that their number difference counts the number of orbitals required to unwind

the relative winding of the nested Wilson loop spectrum. Comparing the Wilson loop and nested Wilson loop spectra of 2D third-order and 3D fourth-order TIs, we show that the fragile topology of 3D insulators is characterized by a nonzero relative winding of the nested Wilson loop, and its unwinding requires extra trivial bands to be added. We show that this idea is generally valid for dD kth-order TIs with $d \geqslant 3$ and $k > d$. In all dimensions d and for all order k, the number of trivial bands needed to unwind all nested Wilson loops is consistent with the number of bands needed to trivialize the fragile topology determined by parity eigenvalues, which is indicated in Eq. (47).

A. Fragile band topology and the relative winding number

The fragile band topology of a dD $(d + 1)$th-order TI is manifested by the winding of the (nested) Wilson loop spectrum. The Wilson loop $W_{\boldsymbol{k}_0 + \boldsymbol{G} \leftarrow \boldsymbol{k}_0}$ indicates the parallel transport of Bloch wave functions along a noncontractible loop in the Brillouin zone, from $\boldsymbol{k}_0$ to $\boldsymbol{k}_0 + \boldsymbol{G}$ where $\boldsymbol{G}$ is a reciprocal lattice vector [65–67]. In a tight-binding model, the Bloch wave function is replaced by the eigenstate $|n, \boldsymbol{k}\rangle$ of the tight-binding Hamiltonian $H(\boldsymbol{k})$, which satisfies $H(\boldsymbol{k})|n, \boldsymbol{k}\rangle = E_n(\boldsymbol{k})|n, \boldsymbol{k}\rangle$. The Wilson loop is defined in terms of $|n, \boldsymbol{k}\rangle$ as

$$\left[W_{\boldsymbol{k}_0 + \boldsymbol{G} \leftarrow \boldsymbol{k}_0}\right]_{nm} = \lim_{N \to \infty} \langle n, \boldsymbol{k}_0 + \boldsymbol{G}| \left[\prod_{i=1}^{N-1} P(\boldsymbol{k}_i)\right]|m, \boldsymbol{k}_0\rangle, \quad (64)$$

where $\boldsymbol{k}_i = \boldsymbol{k}_0 + \frac{i}{N}\boldsymbol{G}$ with an integer i, and n_{occ} denotes the number of occupied states. And the projector into the occupied states $P(\boldsymbol{k})$ is defined by $P(\boldsymbol{k}) = \sum_{n=1}^{n_{\text{occ}}} |n, \boldsymbol{k}\rangle\langle n, \boldsymbol{k}|$. Note that the Wilson loop spectrum $\{\theta(\boldsymbol{k_0})\}$, $W_{\boldsymbol{k}_0 + \boldsymbol{G} \leftarrow \boldsymbol{k}_0}|\theta(\boldsymbol{k_0})\rangle = e^{i\theta(\boldsymbol{k_0})}|\theta(\boldsymbol{k_0})\rangle$, is independent of the start point $\boldsymbol{k}_0$. Instead of the Wilson loop spectrum, we sometimes use the equivalent term, the Wilson bands in the following discussions. Also, since we mostly consider the Wilson loop defined along the k_1 direction, we will denote $\{\theta_1(k_2, k_3, \dots)\}$ as the Wilson loop spectrum. The definition and properties of the Wilson loop are summarized in Appendix H.

Here, let us review the Wilson loop of inversion-symmetric systems studied comprehensively in Ref. [66]. For simplicity, let us consider a 2D plane (k_1, k_2) which is left invariant under the inversion. The Wilson loop spectrum satisfies $\{\theta_1(k_2)\} = \{-\theta_1(-k_2)\}$ and can exhibit chiral and/or relative winding. We always assume that there is no chiral winding since it represents the nonzero Chern number and we are interested in the insulators which are not stable TIs. Figure 10 shows the Wilson loop spectra for a 2D third-order TI and a 3D fourth-order TI. In Fig. 10(a) relevant to the 2D third-order TI, one Wilson band has the winding number 1 while the other one has the winding number -1. Their winding number difference is called the relative winding number N_W, and $N_W = 1$ in this case. Similarly, Fig. 10(b) has $N_W = 2$ while Figs. 10(c) and 10(d) have $N_W = 0$.

Due to the constraint $\{\theta_1(k_2)\} = \{-\theta_1(-k_2)\}$, the Wilson loop spectrum at $\bar{k}_2 = 0, \pi$ consists of $\theta_1(\bar{k}_2) = 0$ or π which are inversion symmetric by itself, or $(-\theta_0, \theta_0)$ which are inversion symmetric as a pair. Thus, we define $n_0^W(\bar{k}_2)$, $n_\pi^W(\bar{k}_2)$, and $n_c^W(\bar{k}_2)$, which indicate the number of Wilson loop spectrum with eigenvalues $\theta(\bar{k}_2) = 0, \pi$, and $(-\theta_0, \theta_0)$, respectively.
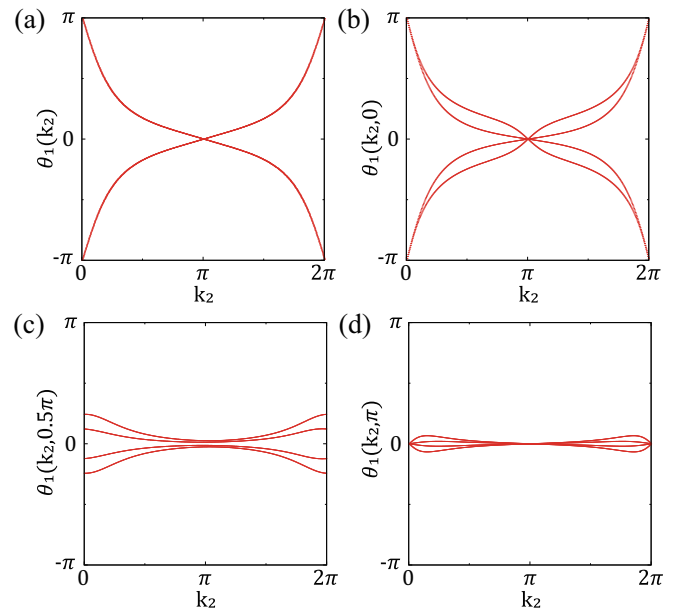

FIG. 10. Wilson loop spectrum. (a) 2D third-order TI. (b)–(d) 3D fourth-order TI. The Wilson loop spectrum shows (a) $N_W = 1$, (b) $N_W = 2$ at $k_3 = 0$. The Wilson loop spectrum (c) at $k_3 = 0.5\pi$, (d) at $k_3 = \pi$. The Wilson loop is defined along the k_1 direction.

For example, the parity configuration $\mathcal{B}_\Gamma(2, 2)$ shown in Fig. 8(a) is mapped to $\{n_\theta^W(0)\} = (n_0^W(0), n_\pi^W(0), n_c^W(0)) = (0, 2, 0)$ and $\{n_\theta^W(\pi)\} = (n_0^W(\pi), n_\pi^W(\pi), n_c^W(\pi)) = (2, 0, 0)$. Then, the relative winding number N_W is given by [66]

$$2N_W = \max\left(n_\pi^W(0) - n_\pi^W(\pi) - n_c^W(\pi),\right.$$
$$\left. n_\pi^W(\pi) - n_\pi^W(0) - n_c^W(0), 0\right), \quad (65)$$

which is unambiguously determined by $n_\xi(\boldsymbol{k}^{\text{inv}})$ where $n_\xi(\boldsymbol{k}^{\text{inv}})$ denotes the number of the occupied bands at $\boldsymbol{k}^{\text{inv}} = (0, 0), (\pi, 0), (0, \pi)$, or (π, π) with inversion parity $\xi = \pm 1$. The mapping between the inversion parities of occupied states $\{n_\xi(\boldsymbol{k}^{\text{inv}})\}$ and the Wilson loop spectrum $\{n_\theta^W(\bar{k}_2)\}$ are studied for arbitrary number of occupied states n_{occ} [66], as summarized in Appendix H 6.

Equation (65) implies that the relative winding N_W is fragile, i.e., N_W decreases as appropriately chosen trivial bands are added. To see this, let us consider the lattice model for a dD $(d + 1)$th-order TI in Eq. (52) with $\lambda = 1$, which has 2^{d-1} occupied eigenstates whose parity configuration corresponds to $\mathcal{B}_\Gamma(d, N_B = 2^{d-1})$. We focus on the (k_1, k_2) plane with $k_{i>2} = 0$. It is straightforward to show that the Wilson loop spectrum of $\mathcal{B}_\Gamma(d, 2^{d-1})$ is given by $\{n_\theta^W(0)\} = \{n_0^W(0), n_\pi^W(0), n_c^W(0)\} = \{0, 2^{d-1}, 0\}$ and $\{n_\theta^W(\pi)\} = \{n_0^W(\pi), n_\pi^W(\pi), n_c^W(\pi)\} = \{2^{d-1}, 0, 0\}$. Then, Eq. (65) gives the relative winding number $N_W = 2^{d-2}$. Now, let us examine how N_W changes as trivial bands are added. In the 2D unit cell in real space, which is reciprocal to the (k_1, k_2) plane, there are four Wyckoff positions: $A = \boldsymbol{0}$, $B = \frac{1}{2}\boldsymbol{a}_1$, $C = \frac{1}{2}\boldsymbol{a}_1 + \frac{1}{2}\boldsymbol{a}_2$, $D = \frac{1}{2}\boldsymbol{a}_2$ where $\boldsymbol{a}_{1,2}$ are relevant lattice vectors. Then, adding a $p(B)$, $p(C)$, or $p(D)$ orbital does not change N_W. Here, we use the expression $p(W)$ to denote the p orbital at the Wyckoff position W. On the

TABLE VIII. Change of parity configuration and the Wilson loop spectrum after adding trivial orbitals.

Band rep.	$\{n_\theta^W(k_2 = 0)\}$			$\{n_\theta^W(k_2 = \pi)\}$			
	$n_0^W(0)$	$n_\pi^W(0)$	$n_c^W(0)$	$n_0^W(\pi)$	$n_\pi^W(\pi)$	$n_c^W(\pi)$	N_W
$\mathcal{B}_\Gamma(d, 2^{d-1}) \oplus p(A)$	1	2^{d-1}	0	$2^{d-1} - 1$	0	2	$2^{d-2} - 1$
$\mathcal{B}_\Gamma(d, 2^{d-1}) \oplus p(B)$	0	$2^{d-1} + 1$	0	2^{d-1}	1	0	2^{d-2}
$\mathcal{B}_\Gamma(d, 2^{d-1}) \oplus p(C)$	0	$2^{d-1} + 1$	0	2^{d-1}	1	0	2^{d-2}
$\mathcal{B}_\Gamma(d, 2^{d-1}) \oplus p(D)$	1	2^{d-1}	0	$2^{d-1} + 1$	0	0	2^{d-2}

other hand, adding a $p(A)$ decreases N_W by 1. In general, the relative winding of the Wilson loop can be unwound by adding 2^{d-2} $p(A)$ orbitals for a dD $(d+1)$th-order TI. The above results are summarized in Table VIII.

We verify numerically the fragile nature of the relative winding number discussed above. Figure 11 shows that the Wilson loop spectrum of 2D third-order TIs changes as expected when $s(A)$ or $p(A)$ orbitals are added. Namely, adding a $p(A)$ orbital opens a gap in the Wilson loop spectrum while adding a $s(A)$ orbital cannot. The details of numerical calculations are summarized in Appendix J. Since the Wilson bands are divided into two sectors ($P_{1,2}$) after we add a $p(A)$ orbital as shown in Fig. 11(b), the Berry phase $\tilde{\Phi}$ of each sector can be calculated. $P_{1,2}$ regroup the Wilson bands in an inversion-symmetric manner, and thus have quantized Berry phases $\tilde{\Phi}[P_{1,2}]$ in the k_2 direction. We find $\tilde{\Phi}[P_1] = \pi$ and $\tilde{\Phi}[P_2] = (0, \pi)$. On the other hand, let us note that the average Φ of the Wilson loop eigenvalues in P_1 and P_2 sectors along the k_1 direction are 0 in both cases. As the two Wilson bands in P_2 have a fixed symmetric value $\theta_1(k_2) = \pi$ at $k_2 = 0$, we interpret $\Phi[P_2] = 0$ in a way that the Wannier centers of the two Wilson bands in the $\boldsymbol{a}_1$ direction are $\frac{1}{2}$ in both cases. Thus, we conclude that the Wannier centers of three bands in P_1 and P_2 are $(0, \pi)$, $(\pi, 0)$, and (π, π), respectively. These values support that the Wannier state representation for the 2D third-order TI is $\ominus p(A) \oplus p(B) \oplus p(C) \oplus p(D)$ [20]. This is also consistent with Eq. (47) and the corner charge accumulation [60] in the square boundary shown in Fig. 9(b).

Let us note that the fragility of $N_W = 1$ Wilson bands has already been studied in Refs. [20,48]. However, the fragility of $N_W = 2$ Wilson bands in a 3D fourth-order TI and in its higher-dimensional generalization has more involved

structures and has not been studied yet. In the following, we show that, when $d > 2$, adding 2^{d-2} $p(A)$ orbitals are not sufficient to trivialize the fragile topology of dD $(d+1)$th-order TI even though it makes all the relative windings of the Wilson loops to be zero. This implies the nontrivial winding of the nested Wilson loops, which is addressed in the next section.

B. Nested Wilson loop and trivialization of fragile topology

In this section, we discuss the fragility of the Wilson loop of the 3D fourth-order TI. Symmetry data analysis shows that the trivialization of the 3D fourth-order TI requires at least three $p(A)$ orbitals although the relative winding of the Wilson bands can be gapped with two $p(A)$ orbitals. To understand the origin of the mismatch in the number of required orbitals, we investigate the nested Wilson loop of the 3D fourth-order TI with two or three additional $p(A)$ orbitals.

1. Adding one $p(A)$ orbital

Adding one $p(A)$ orbital reduces the relative winding from $N_W = 2$ to 1 as shown in Figs. 12(a)–12(c). Thus, the winding of the Wilson loop persists, and thus the nontrivial band topology still exists.

2. Adding two $p(A)$ orbitals

Adding two $p(A)$ orbitals reduces the relative winding from $N_W = 2$ to 0 as shown in Figs. 12(d)–12(f). Six Wilson bands are divided into two groups, P_{in} and P_{out}, in an inversion-symmetric manner. Then, we can compute the nested Wilson loops of P_{in} and P_{out}, which show nonzero nested Chern numbers $C_{\text{nest}} = -2$ and $C_{\text{nest}} = 2$, respectively, as shown in Figs. 13(a) and 13(b). This can be explained by the fact that a 3D fourth-order TI can be considered as two copies of the class A 3D second-order TI, i.e., the axion insulator, which is characterized by an odd nested Chern number [20]. However, let us note that an even value of the nested Chern number itself does not guarantee the nontrivial bulk topology. This is because only the parity of C_{nest} remains robust when a band crossing between Wilson bands in P_{in} and those in P_{out}, or a Wilson band transition, happens while keeping the bulk gap [20]. Since two $p(A)$ orbitals cannot trivialize the band topology according to the symmetry data analysis, the nontrivial bulk topology must be manifested in the nested Wilson loop. We show that the nontrivial band topology appears in the form of the relative winding in the nested Wilson loop. After the band crossing between Wilson bands, the nested Wilson loop of P_{in} shows the nested relative winding number $N_{W,\text{nest}} = 1$ while the nested Wilson loop of P_{out} is completely unwound as shown in Figs. 13(c) and 13(d). In the nested Wilson loop spectra for P_{in} sector shown in Figs. 13(a) and 13(c), we
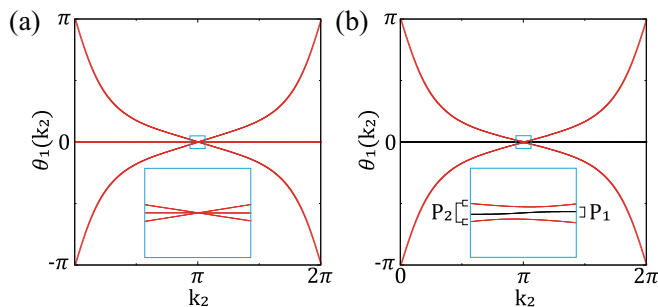

FIG. 11. The Wilson loop spectrum of 2D third-order TI. (a) Adding $s(A)$ orbital cannot open the gap of Wilson spectrum. (b) Adding $p(A)$ orbital opens the gap of Wilson loop spectrum. Three bands are divided into P_1 and P_2. The black band (red bands) belongs (belong) to P_1 (P_2). P_1 band has the nested Berry phase π, and P_2 bands have the nested Berry phases $(0, \pi)$.
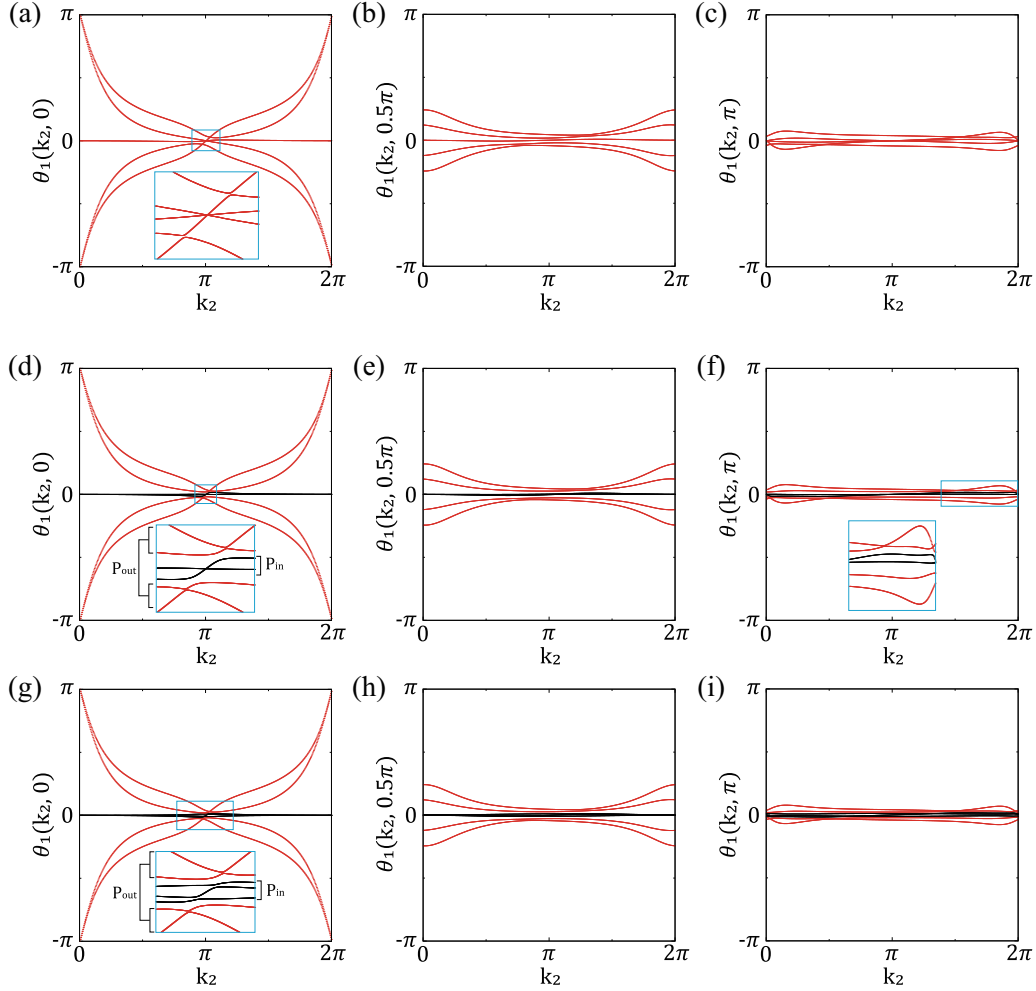
FIG. 12. The Wilson loop spectrum of 3D fourth-order TI (a)–(c) after adding one $p(A)$ orbital, (d)–(f) after adding two $p(A)$ orbitals, (g)–(i) after adding three $p(A)$ orbitals. (a) The Wilson loop spectrum at $k_3 = 0$. The $N_W = 2$ relative winding is reduced to $N_W = 1$. (b) The Wilson loop spectrum at $k_3 = 0.5\pi$. (c) The Wilson loop spectrum at $k_3 = \pi$. (d) The Wilson loop spectrum at $k_3 = 0$. The $N_W = 2$ relative winding is reduced to $N_W = 0$. (e) The Wilson loop spectrum at $k_3 = 0.5\pi$. (f) The Wilson loop spectrum at $k_3 = \pi$. (g) The Wilson loop spectrum at $k_3 = 0$. The $N_W = 2$ relative winding is reduced to $N_W = 0$. (h) The Wilson loop spectrum at $k_3 = 0.5\pi$. (i) The Wilson loop spectrum at $k_3 = \pi$. As the Wilson spectra are gapped after adding two or three $p(A)$ orbitals, we can define two sectors of Wilson bands, P_{in} and P_{out}.

have $|C_{\text{nest}}| + 2N_{W,\text{nest}} = 2$. This means that the fragile band topology manifests as the nontrivial winding of the nested Wilson loop spectrum encoded in either C_{nest} or $N_{W,\text{nest}}$.

By generalizing the above results, we propose an indicator $N_{d,\text{nest}}$ which characterizes the fragile band topology. First, let us define $N_{d,\text{nest}}$ in a way similar to how its counterpart N_d in Eq. (65) is defined for the Wilson loop:

$$N_{d,\text{nest}} \equiv \max\big(n_\pi^{W_{\text{nest}}}(0) - n_\pi^{W_{\text{nest}}}(\pi) - n_c^{W_{\text{nest}}}(\pi),$$
$$n_\pi^{W_{\text{nest}}}(\pi) - n_\pi^{W_{\text{nest}}}(0) - n_c^{W_{\text{nest}}}(0)\big), \qquad (66)$$

where $n_\pi^{W_{\text{nest}}}(\bar{k}_3)$ and $n_c^{W_{\text{nest}}}(\bar{k}_3)$ are the number of eigenvalues equal to π and that equal to a generic value, respectively, in the nested Wilson loop spectrum computed at $\bar{k}_3 = 0, \pi$. The indicator $N_{d,\text{nest}}$ is invariant under a band crossing between the Wilson bands, and thus it determines the band topology of a given nested Wilson loop spectrum. We note that there may be one or more gaps in the Wilson loop spectrum, and all possible nested Wilson loop spectra have to be considered.

Let us distinguish the indicator $N_{d,\text{nest}}$ into the following ways: (i) When $N_{d,\text{nest}}$ is an odd integer, the nested Wilson loop spectrum shows an odd C_{nest}. This implies the stable band topology. (ii) When $N_{d,\text{nest}}$ is a positive even integer, $|C_{\text{nest}}| + 2N_{W,\text{nest}} = N_{d,\text{nest}}$ holds for $|C_{\text{nest}}| < N_{d,\text{nest}}$. Thus, the nested Wilson loop shows the nested relative winding number equal to $N_{W,\text{nest}} = \frac{1}{2}N_{d,\text{nest}}$ even when the band crossing between the Wilson bands change C_{nest} to zero. (iii) When $N_{d,\text{nest}}$ is a negative even integer or zero, the nested Wilson loop can be unwound by a band crossing between the Wilson bands. The rules (ii) and (iii) can be applied to the nested Wilson loop spectrum of P_{in} and P_{out} which show $N_{d,\text{nest}} = 2$ and -2, respectively, as shown in Figs. 13(a)–13(d). More details of our claim and the relevant proof are provided in Appendix. I.

3. Adding three $p(A)$ orbitals

Adding the third $p(A)$ orbital to the case considered above makes little changes in the Wilson loop spectra. For instance,
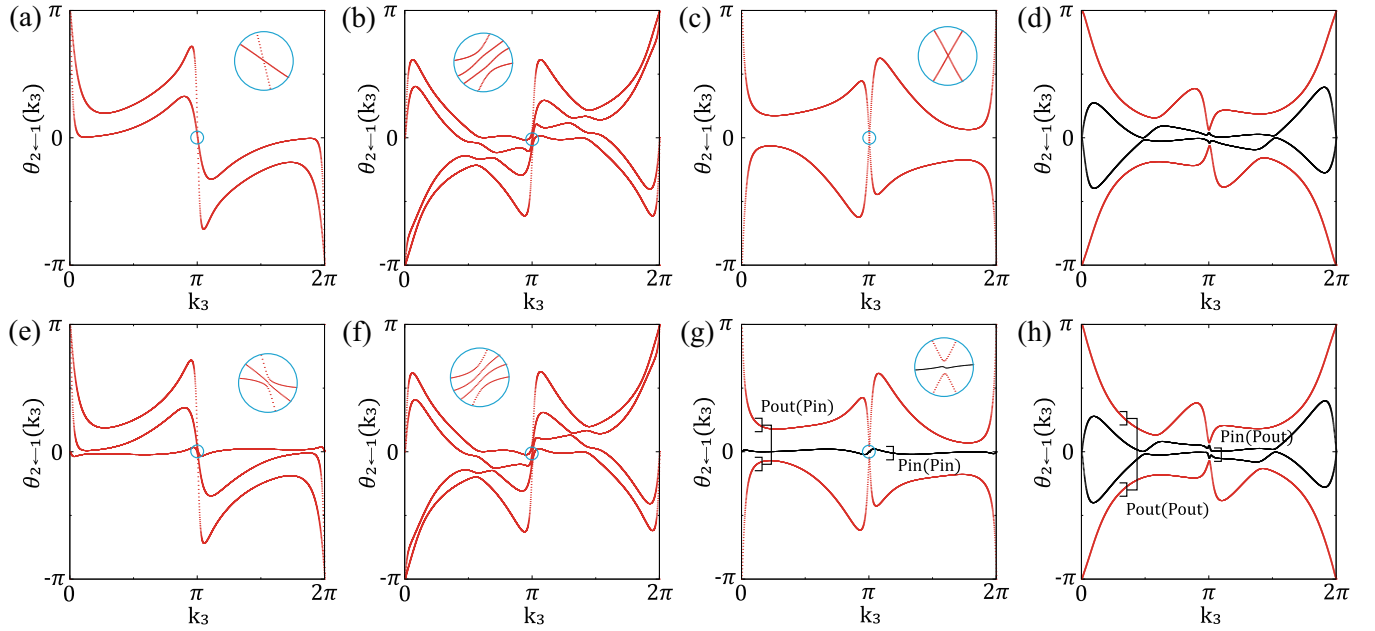
FIG. 13. The nested Wilson loop spectra of 3D fourth-order TI after adding two or three trivial $p(A)$ orbitals. (a)–(d) The nested Wilson loop spectrum of 3D fourth-order TI with two additional $p(A)$ orbitals. The nested Wilson loop spectrum of (a) $P_{\rm in}$, (b) $P_{\rm out}$ before the Wilson band transition. The nested Wilson loop spectrum of (c) $P_{\rm in}$, (d) $P_{\rm out}$ after the Wilson band transition. (e)–(h) The nested Wilson loop spectrum of 3D fourth-order TI with three additional $p(A)$ orbitals. The nested Wilson loop spectrum of (e) $P_{\rm in}$, (f) $P_{\rm out}$ before the Wilson band transition. The nested Wilson loop spectrum of (g) $P_{\rm in}$, (h) $P_{\rm out}$ after the Wilson band transition.

the third $p(A)$ orbital does not change the nested Chern number $C_{\rm nest}$ as shown in Figs. 13(e) and 13(f). However, after the band crossing between Wilson bands in $P_{\rm in}$ and those in $P_{\rm out}$, the windings in the nested Wilson loops for both $P_{\rm in}$ and $P_{\rm out}$ have been unwound as shown in Figs. 13(g) and 13(h). This can be inferred from the fact that the nested Wilson loop spectrum of $P_{\rm in}$ and $P_{\rm out}$ in Figs. 13(e)–13(h) show $N_{d,\rm nest} = 0$ and -2, respectively. Therefore, we conclude that the fragile TI is characterized by the nontrivial relative winding of the nested Wilson loop.

Since the Wannier obstruction is fully relaxed, we can find the Wannier state representations corresponding to the cases shown in Figs. 13(g) and 13(h). One interesting feature of the nested Wilson loops in Fig. 13(g) is that even the nest Wilson bands from $P_{\rm in}$ can be divided further into two different groups of nested Wilson bands, $P_{\rm in}(P_{\rm in})$ and $P_{\rm out}(P_{\rm in})$, which is possible since there is no winding or relative winding in the spectrum. Similarly, Fig. 13(h) shows that the nested Wilson bands from $P_{\rm out}$ can be divided into $P_{\rm in}(P_{\rm out})$ and $P_{\rm out}(P_{\rm out})$ (see Appendix H for more details). Then, the corresponding averaged eigenvalues Φ and the Berry phases $\tilde{\Phi}$ are given by $\Phi[P_{\rm in,out}] = \Phi[P_{\rm in,out}(P_{\rm in,out})] = 0$, $\tilde{\Phi}[P_{\rm in}(P_{\rm in})] = \pi$, $\tilde{\Phi}[P_{\rm out}(P_{\rm in})] = (0, \pi)$, $\tilde{\Phi}[P_{\rm in}(P_{\rm out})] = (0, \pi)$, and $\tilde{\Phi}[P_{\rm out}(P_{\rm out})] = (0, \pi)$. Here, $\Phi[P_i]$ ($\Phi[P_i(P_j)]$) indicates the average eigenvalues of the Wilson band P_i [the nested Wilson band $P_i(P_j)$] while $\tilde{\Phi}[P_i]$ ($\tilde{\Phi}[P_i(P_j)]$) denotes the Berry phase of the Wilson band P_i [the nested Wilson band $P_i(P_j)$]. The corresponding Wannier centers of the seven occupied states are $(0, \pi, 0)$, $(\pi, 0, 0)$, $(\pi, \pi, 0)$, $(0, 0, \pi)$, $(0, \pi, \pi)$, $(\pi, 0, \pi)$, and (π, π, π), respectively. This supports that the Wannier state representation for the 3D fourth-order TI is $\bigoplus_{i=2}^{8} p(W_i) \ominus 3p(W_1)$, which is con-

sistent with Eq. (47). Also, the corner charge accumulation in the cubic geometry shown in Fig. 9(e) can be related to the Wannier state representation in the same way as in 2D.

C. Generalization to higher dimensions and higher order

The idea presented in the previous section can be generalized further to dD kth-order TI with $d \geqslant 3$ and $k > d$. The key observation is that only the inner Wilson bands in P_{in} of the trivialized lth nested Wilson loop have the relative winding number in their $(l + 1)$th nested Wilson loop spectrum. We assume that the nested Chern numbers are always zero, which can always be achieved via the band crossing between Wilson bands.

Explicitly, according to the discussion in Sec. V, a dD kth-order TI has an equivalent Wannier state representation given by

$$2^{n-d}\left[\bigoplus_{i=1}^{2^d} p(W_i) \ominus 2^{d-1} p(W_1) \right], \qquad (67)$$

where $d + k = 2n + 1$ and $n = d, d + 1, \ldots$ for class A systems. Thus, the dD kth-order TI can be trivialized by adding $2^{n-d}(2^{d-1} - 1) p(W_1)$ orbitals according to Eq. (67). Now, we give a heuristic argument suggesting that $2^{n-d} \times 2^{d-l-2} p(W_1)$ orbitals trivialize the relative winding of lth nested Wilson loop for $l = 0, 1, \ldots, d - 2$. Here, the 0th nested Wilson loop means the conventional non-nested Wilson loop. First, we consider the Wilson loop of dD kth-order TI defined along the k_d direction. As shown in Sec. VI A, it has the relative winding number $2^{n-d} \times 2^{d-2}$. Thus, adding $2^{n-d} \times 2^{d-2} p(W_1)$ orbitals unwinds the Wilson loop

completely. Then, the resulting Wannier state representation is

$$2^{n-d}\left[\bigoplus_{i=1}^{2^d} p(W_i) \ominus 2^{d-2} p(W_1)\right]. \quad (68)$$

Since there is no relative winding in the Wilson loop, the Wilson bands can be divided into two groups P_{in} and P_{out}. Here, P_{in} consist of the nearly flat Wilson bands near $\theta_1 = 0$ which come from the additional trivial orbitals. This indicates that the Wannier centers of the Wilson bands in P_{in} in the $\boldsymbol{a}_d$ direction are all zero. Then, the Wannier state representation of the Wilson bands in P_{in} is equivalent to

$$2^{n-d}\left[\bigoplus_{i=1}^{2^{d-1}} p(W_i) \ominus 2^{d-2} p(W_1)\right], \quad (69)$$

where we projected out the Wyckoff positions W_i ($i = 2^{d-1} + 1, \ldots, 2^d$) whose coordinate in the $\boldsymbol{a}_d$ direction is $\frac{1}{2}$. Since the Wannier state representation in Eq. (69) is equivalent to that for the $(d-1)$D $(k-1)$th-order TI, we can repeat a similar procedure to trivialize the first nested Wilson loop. Repeating this procedure recursively, we conclude that the inner Wannier bands P_{in} of the lth nested Wilson loop are equivalent to the $(d-l-1)$D $(k-l-1)$th-order TI which is characterized by the relative winding number $2^{n-d} \times 2^{d-l-3}$. This completes our heuristic proof. Since adding $2^{n-d} \times 2^{d-l-2} p(W_1)$ orbitals can unwind the lth nested Wilson loop for $l = 0, 1, \ldots, d-2$, the total number of $p(W_1)$ orbitals required for complete trivialization is

$$\sum_{l=0}^{d-2} 2^{n-d} \times 2^{d-l-2} = 2^{n-d}(2^{d-1} - 1). \quad (70)$$

In this way, we can understand the total number of additional orbitals required to trivialize the fragile topology in terms of the relative winding numbers in all possible nested Wilson loops.

VII. GENERAL PUMPING PROCESS

In this section, we describe the pumping process of inversion-symmetric TIs. The main claim is that the band topology of the $(d+1)$D $(k-1)$th-order TI can be understood in terms of the adiabatic pumping process between the dD kth-order TI and the trivial-parity insulator along the $(d+1)$th momentum direction. In particular, we discuss how the higher-order TIs with hinge states, i.e., $(d+1)$D dth-order TIs, can be constructed via the pumping process of dD $(d+1)$th-order TIs. This can be considered as the generalization of the idea proposed in Ref. [20].

A. General pumping process

Let us consider an adiabatic pumping process of the parity configurations of dD kth-order TIs along the k_{d+1} direction between $k_{d+1} = 0$ and $k_{d+1} = \pi$ planes. We label the symmetry data in the $k_{d+1} = 0$ plane as $\{n_-(\boldsymbol{k}_1^{\text{inv}}) - n_+(\boldsymbol{k}_1^{\text{inv}}), \ldots, n_-(\boldsymbol{k}_{2^d}^{\text{inv}}) - n_+(\boldsymbol{k}_{2^d}^{\text{inv}})\}$ and those in the $k_{d+1} = \pi$ plane as $\{n_-(\boldsymbol{k}_{2^d+1}^{\text{inv}}) - n_+(\boldsymbol{k}_{2^d+1}^{\text{inv}}), \ldots, n_-(\boldsymbol{k}_{2^{d+1}}^{\text{inv}}) - n_+(\boldsymbol{k}_{2^{d+1}}^{\text{inv}})\}$, respectively. At each dD subspace, the momentum-space symmetry data can be mapped to 2^d $\nu_W(k_{d+1})$ indices for dD inversion-symmetric insulator by using Eq. (39) as

$$\begin{pmatrix} \nu_{W_1}(0) \\ \nu_{W_2}(0) \\ \nu_{W_3}(0) \\ \vdots \\ \nu_{W_{2^d}}(0) \end{pmatrix} = A_d \begin{pmatrix} n_-(\boldsymbol{k}_1^{\text{inv}}) - n_+(\boldsymbol{k}_1^{\text{inv}}) \\ n_-(\boldsymbol{k}_2^{\text{inv}}) - n_+(\boldsymbol{k}_2^{\text{inv}}) \\ n_-(\boldsymbol{k}_3^{\text{inv}}) - n_+(\boldsymbol{k}_3^{\text{inv}}) \\ \vdots \\ n_-(\boldsymbol{k}_{2^d}^{\text{inv}}) - n_+(\boldsymbol{k}_{2^d}^{\text{inv}}) \end{pmatrix} \quad (71)$$

and

$$\begin{pmatrix} \nu_{W_1}(\pi) \\ \nu_{W_2}(\pi) \\ \nu_{W_3}(\pi) \\ \vdots \\ \nu_{W_{2^d}}(\pi) \end{pmatrix} = A_d \begin{pmatrix} n_-(\boldsymbol{k}_{2^d+1}^{\text{inv}}) - n_+(\boldsymbol{k}_{2^d+1}^{\text{inv}}) \\ n_-(\boldsymbol{k}_{2^d+2}^{\text{inv}}) - n_+(\boldsymbol{k}_{2^d+2}^{\text{inv}}) \\ n_-(\boldsymbol{k}_{2^d+3}^{\text{inv}}) - n_+(\boldsymbol{k}_{2^d+3}^{\text{inv}}) \\ \vdots \\ n_-(\boldsymbol{k}_{2^{d+1}}^{\text{inv}}) - n_+(\boldsymbol{k}_{2^{d+1}}^{\text{inv}}) \end{pmatrix}. \quad (72)$$

Let us note that, thanks to the simple structure of inversion symmetry, the matrix A_d in Eq. (39), which connects the symmetry data in real and momentum spaces, satisfies the following simple recursion relation:

$$A_{d+1} = \frac{1}{2}\begin{pmatrix} A_d & A_d \\ A_d & -A_d \end{pmatrix}, \quad (73)$$

which is proved in Appendix. B. Then, 2^{d+1} ν_W indices for $(d+1)$D inversion-symmetric insulator are given by

$$\nu_{W_i} = \frac{1}{2}\left[\nu_{W_i}(0) + \nu_{W_i}(\pi)\right],$$
$$\nu_{W_{i+2^d}} = \frac{1}{2}\left[\nu_{W_i}(0) - \nu_{W_i}(\pi)\right], \quad (74)$$

where $i = 1, \ldots, 2^d$. Thus, the resulting phase can be diagnosed by using $\{\nu_W(0)\}$ and $\{\nu_W(\pi)\}$.

Equation (74) shows that any fragile TI or atomic insulators in $(d+1)$D can be understood as a pumping process between fragile TI or atomic insulators. Since all ν_W indices for $(d+1)$D fragile TI or atomic insulator are integers, all $\nu_{W_i}(0)$ and $\nu_{W_i}(\pi)$ are also integers according to Eq. (74). This means that the parity configurations at $k_{d+1} = 0$ and π correspond to either fragile TIs or atomic insulators.

In Sec. IV C, it is mentioned that, when $n_{\text{occ}} = 2$, the fragile TI in higher dimensions can be obtained by a layer stacking of 2D fragile TI, and this process can also be described by a momentum-space pumping of fragile TIs. To illustrate this idea, let us consider a trivial pumping process in which the parity configurations at $k_{d+1} = 0$ and π are identical to each other, i.e., $\nu_{W_i}(0) = \nu_{W_i}(\pi)$ for $i = 1, \ldots, 2^d$. In this situation, ν_W indices for $(d+1)$D inversion-symmetric insulator are given by $\nu_{W_i} = \nu_{W_i}(0)$ and $\nu_{W_{i+2^d}} = 0$ for $i = 1, \ldots, 2^d$. This shows that a fragile TI with $n_{\text{occ}} = 2$ in 3D, $\{\nu_W\} = \{-1, 1, 1, 1, 0, 0, 0, 0\}$, for example, can be understood as a trivial pumping process of 2D fragile TI with $\{\nu_W(0)\} = \{\nu_W(\pi)\} = \{-1, 1, 1, 1\}$ in the k_3 direction, consistent with the previous description.

B. Hamiltonian mapping

Here, we show that an adiabatic pumping between the dD kth-order TI and the trivial-parity insulator leads to the

$(d + 1)$D $(k - 1)$th-order TI:

$$(d + 1)D(k - 1)\text{th-order TI}$$
$$=$$
Pumping between a dD kth-order TI and the
trivial $-$ parity insulator.

The Hamiltonians for a class A dD kth-order TI and a $(d + 1)$D $(k - 1)$th-order TI are given by

$$H_{\text{A}(d,k)} = \sum_{i=1}^{d} \sin k_i \Gamma_i - \left(d - \lambda + \sum_{i=1}^{d} \cos k_i \right) \mathcal{M} \quad (75)$$

and

$$H_{\text{A}(d+1,k-1)} = \sum_{i=1}^{d+1} \sin k_i \Gamma_i - \left(d + 1 - \lambda + \sum_{i=1}^{d+1} \cos k_i \right) \mathcal{M}, \quad (76)$$

where the number of Γ matrices is $q = d + k = 2n + 1$ and their dimension is $2^n \times 2^n$. The bulk mass term $\mathcal{M}$ and the inversion-symmetry operator I are given by $\mathcal{M} = I = \Gamma_q$. The parity configurations corresponding to $H_{\text{A}(d,k)}$ and $H_{\text{A}(d+1,k-1)}$ are $\mathcal{B}_\Gamma(d, 2^{n-1})$ and $\mathcal{B}_\Gamma(d + 1, 2^{n-1})$, respectively. The ν_W indices for $\mathcal{B}_\Gamma(d, 2^{n-1})$ are given by

$$2^{n-d}\{1 - 2^{d-1}, 1, \ldots, 1\}, \quad (77)$$

while those for the trivial parity configuration of 2^{n-1} bands with only positive parities are

$$\{-2^{n-1}, 0, \ldots, 0\}. \quad (78)$$

Thus, the pumping between $\mathcal{B}_\Gamma(d, 2^{n-1})$ and the trivial parity configuration gives 2^{d+1} ν_W indices $2^{n-d-1}\{1 - 2^d, 1, 1, \ldots, 1\}$, which is exactly the ν_W indices of $\mathcal{B}_\Gamma(d + 1, 2^{n-1})$.

Also, one can explicitly construct a mapping between the Hamiltonians given by

$$\varphi_\uparrow[H_{\text{A}(d,k)}](\boldsymbol{k}, k_{d+1}, \lambda)$$
$$= H_{\text{A}(d,k)}(\boldsymbol{k}, \lambda - 1 + \cos k_{d+1}) + \sin k_{d+1} \Gamma_{d+1}, \quad (79)$$

where $H_{\text{A}(d,k)}(\boldsymbol{k}, \lambda)$ is the Hamiltonian for a dD kth-order TI in Eq. (75). The map $\varphi_\uparrow[H]$ increases the dimension of the Hamiltonian H by one, and describes the pumping process of the dD kth-order TI. Here, λ is a parameter governing the topological phase transition between the trivial and topological phases. $(d + k)$ should be an odd integer in order that the dD kth-order and $(d + 1)$D $(k - 1)$th-order TIs exist. $H_{\text{A}(d,k)}(\boldsymbol{k}, \lambda)$ is in the trivial (topological) phase when $\lambda < 0$ $(0 < \lambda < 2)$. For any k_{d+1}, the map $\varphi_\uparrow[H_{\text{A}(d,k)}](\boldsymbol{k}, k_{d+1}, \lambda) = H_{\text{A}(d+1,k-1)}$ preserves the bulk gap since

$$\{\varphi_\uparrow[H_{\text{A}(d,k)}](\boldsymbol{k}, k_{d+1}, \lambda)\}^2 > 0. \quad (80)$$

The nontrivial topology of $\varphi_\uparrow[H_{\text{A}(d,k)}]$ originates from the band topology of $H_{\text{A}(d,k)}$. $\varphi_\uparrow[H_{\text{A}(d,k)}]$ is in the topological (trivial) phase of $H_{\text{A}(d,k)}$ at $k_{d+1} = 0$ $(k_{d+1} = \pi)$ when $0 < \lambda < 2$. Hence, the map $\varphi_\uparrow[H_{\text{A}(d,k)}]$ describes the desired pumping process.

One can consider the following examples as an application of the pumping picture. For instance, a pumping of

a 1D second-order TI described by the SSH model without chiral symmetry leads to the 2D first-order TI, the Chern insulator. A pumping of a 2D third-order TI gives a 3D second-order TI, the axion insulator [20]. Finally, a pumping of a 3D second-order TI gives a 4D first-order TI, the 4D Chern insulator. In the case of other AZ classes, the Hamiltonian mapping is more restricted. For instance, in class AI, a pumping of a 2D third-order TI produces $\mathbb{Z}_2$ monopole nodal line semimetal [83–89]. In the case of class AII, a pumping of a 2D third-order TI generates the doubled strong TI characterized by the $\mathbb{Z}_4$ symmetry indicator [11,41,43]. Finally, let us mention several related works discussing the pumping of a 2D third-order TI. References [45,90] discussed a charge-pumping process of roto-inversion-symmetric systems. Reference [91] discussed a fractional charge bound to a vortex, which can be understood as a charge-pumping process, in the systems with various crystalline symmetries including inversion symmetry. Although the relevant symmetries are different from ours, all these pumping processes are essentially the pumping of a 2D third-order TI, or 2D second-order TI when the chiral symmetry is present, to a 3D second-order TI.

VIII. CONCLUSION

In this work, we systematically study the bulk and boundary properties of fragile TIs protected by inversion symmetry. In particular, we focus on the class A inversion-symmetric insulators which can be characterized by $(2^d + 1)$ invariants, n_{occ} and $\{\nu_W\}$, defined in terms of symmetry data in momentum space. Using these invariants, stable TIs, fragile TIs, and atomic insulators are distinguished. We propose an efficient method for diagnosing fragile topological phases protected by inversion symmetry, and estimate the number of parity configurations corresponding to atomic insulators, fragile TIs, and stable TIs, respectively. Considering that the symmetry indicator cannot distinguish atomic insulators and fragile TIs, our diagnosis method goes beyond the recently proposed diagnosis schemes.

We have extended the notion of higher-order topology by generalizing the concept of dD kth-order TI to the cases with $k > d$, which is normally defined for $k \leqslant d$. We show that dD kth-order TIs with $k > d$ have fragile band topology. In contrast to the case of stable TIs where the relative topology between a trivial and a topological insulators can be described by a Dirac Hamiltonian unambiguously, the relative topology between a fragile TI and an atomic insulator is more subtle. In particular, the Dirac Hamiltonian approach to the fragile TI is meaningful only when we specify trivial insulator taking into account the parity of occupied states at all inversion-invariant momenta. In our case, we define the trivial-parity insulator having positive-parity occupied states at all inversion-invariant momenta as a reference trivial insulator. Then, the band inversion described by the Dirac Hamiltonian gives a fragile TI unambiguously. In fact, once we have the full symmetry data at all inversion-invariant momenta, we can completely analyze the fragile band topology protected by inversion symmetry which we have demonstrated rigorously.

Moreover, we derive the bulk-boundary correspondence of dD $(d + 1)$th-order TI, and identify a minimal fragile

phase with the filling anomaly as the dD $(d+1)$th-order TI. In other words, a fragile TI corresponding to the dD $(d+1)$th-order phase can have nontrivial boundary charge. We also explain the topological origin of the charge accumulation on the boundary. We show how the mass winding, the induced current, the filling anomaly, and corner charges are related to each other in a unified way. In the case of dD kth-order TIs with $k > (d+1)$ although there is no nontrivial charge accumulation, the net parity $\mathcal{I}$, serves as a bulk topological invariant for for any $k > d$. In fact, the net parity characterizes the bulk topology of all inversion-symmetric insulators without gapless boundary states. Also, from the careful study of Wilson loops and nested Wilson loops, we show that fragile topological phases are characterized by the relative winding in all possible Wilson loops. Finally, we discuss the implication of the pumping process of inversion-symmetric insulators.

We expect that all the concepts developed in this paper, such as the mass winding, topological induced currents, the net parity, and the diagnosis of fragile topology based on symmetry data, can be applied to other topological crystalline insulators in general. For example, the mass winding approach can be extended to fragile topological or atomic phases with rotation symmetries, considering the recent progress reported in Refs. [24,36,37,60]. We leave the extension of our theory to more general cases of fragile TIs protected by various space groups and magnetic space groups for future studies.

Note added. Recently, we noticed that a paper by Song *et al.* [25] appeared on arXiv. They classified all fragile topological phases indicated by symmetry eigenvalues for the class AII and 230 space groups. For inversion-symmetric cases, i.e., space group 2, linear inequalities for diagnosing fragile TIs are proposed in Ref. [25] which is equivalent to our nonlinear inequality in Fig. 5.

APPENDIX A: DERIVATION OF DIAGNOSIS CRITERION

In this Appendix, we derive our criterion $\sum_W |\nu_W| > n_{\mathrm{occ}}$ that distinguishes the fragile topological and atomic phases. In the following, we adopt two assumptions: (i) the band topology is not stable topological, i.e., it is either a fragile topological phase or an atomic phase, and (ii) we consider only the band topology protected by inversion symmetry, such that inversion parity determines the band topology exactly.

Let us first prove that the phases with $\sum_W |\nu_W| > n_{\mathrm{occ}}$ cannot be atomic insulator. Any atomic phase has μ_W integer greater than or equal to zero. Then, the following inequality

holds:

$$n_{\mathrm{occ}} = \sum_W (\mu_{W,+} + \mu_{W,-}) \geqslant \sum_W |\mu_{W,+} - \mu_{W,-}| = \sum_W |\nu_W|. \tag{A1}$$

Thus, a phase which satisfies $\sum_W |\nu_W| > n_{\mathrm{occ}}$ cannot be atomic phase.

Now, let us prove that insulators satisfying $\sum_W |\nu_W| \leqslant n_{\mathrm{occ}}$ are atomic insulators. In other words, we can construct an equivalent Wannier state representation with $\mu_{W,\pm} \geqslant 0$. From the n_{occ} occupied states, we first construct $\sum_W |\nu_W|$ Wannier states

$$\bigoplus_{W,\xi} \left(\frac{s_W - \xi}{2} \right) \nu_W \, w_\xi(W), \tag{A2}$$

where $s_W = \mathrm{sgn}(\nu_W)$. By construction, we have $\mu_{W,\xi} = (\frac{s_W - \xi}{2}) \nu_W = (|\nu_W| - \xi \nu_W)/2 \geqslant 0$. Then, we consider the remaining $n_{\mathrm{occ}} - \sum_W |\nu_W|$ states. Since the Wannier state representation in Eq. (A2) satisfies $\mu_{W,-} - \mu_{W,+} = \nu_W$ already, adding the remaining states should not change ν_W at each W. It can be done by locating pairs of even- and odd-parity states at the Wyckoff positions. It is possible to do so because $n_{\mathrm{occ}} - \sum_W |\nu_W| = \sum_{W,\xi} (1 + \xi s_W) \mu_{W,\xi}$ and $(1 \pm s_W)$ are even integers. Thus, we can locate $\frac{1}{2}(n_{\mathrm{occ}} - \sum_W |\nu_W|)$ pairs of s and p orbitals at any W without changing ν_W.

In conclusion, an insulator satisfying $\sum_W |\nu_W| > n_{\mathrm{occ}}$ is fragile TI, and vice versa.

APPENDIX B: PROPERTIES OF A_d AND ν_W

1. Representation of symmetric Wannier state

Let us consider a Wannier state $w_\xi(W)$ centered at the Wyckoff position W in the unit cell labeled by the lattice vector $\boldsymbol{R}$. We denote such states as $|w_{\xi,\boldsymbol{R}}(W)\rangle$. Inversion symmetry acts on $|w_{\xi,\boldsymbol{R}}(W)\rangle$ as

$$I |w_{\xi,\boldsymbol{R}}(W)\rangle = \xi |w_{\xi,-\boldsymbol{R}-2W}(W)\rangle, \tag{B1}$$

where $\xi = \pm 1$. Then, the corresponding Bloch wave function $|\psi_\xi^W(\boldsymbol{k})\rangle$ is

$$\left| \psi_\xi^W(\boldsymbol{k}) \right\rangle = \frac{1}{\sqrt{N_{\mathrm{cell}}}} \sum_{\boldsymbol{R}} e^{i\boldsymbol{k}\cdot\boldsymbol{R}} |w_{\xi,\boldsymbol{R}}(W)\rangle, \tag{B2}$$

where N_{cell} is the number of unit cells. Its transformation property under inversion is inherited from $|w_{\xi,\boldsymbol{R}}(W)\rangle$,

$$\begin{aligned} I \left| \psi_\xi^W(\boldsymbol{k}) \right\rangle &= \frac{1}{\sqrt{N_{\mathrm{cell}}}} \sum_{\boldsymbol{R}} e^{i\boldsymbol{k}\cdot\boldsymbol{R}} I |w_{\xi,\boldsymbol{R}}(W)\rangle \\ &= \frac{1}{\sqrt{N_{\mathrm{cell}}}} \sum_{\boldsymbol{R}} e^{i\boldsymbol{k}\cdot\boldsymbol{R}} \xi |w_{\xi,-\boldsymbol{R}-2W}(W)\rangle \\ &= \frac{1}{\sqrt{N_{\mathrm{cell}}}} \sum_{\boldsymbol{R}'} e^{-i\boldsymbol{k}\cdot(\boldsymbol{R}'+2W)} \xi |w_{\xi,\boldsymbol{R}'}(W)\rangle \\ &= \xi e^{-2i\boldsymbol{k}\cdot W} \left| \psi_\xi^W(-\boldsymbol{k}) \right\rangle. \end{aligned} \tag{B3}$$

This means that the Bloch wave function $|\psi_\xi^W(\boldsymbol{k})\rangle$ constructed by $w_\xi(W_i)$ has parity $\xi \eta_{ij}$ at inversion-invariant momentum $\boldsymbol{k}_j^{\mathrm{inv}}$, where we define $\eta_{ij} \equiv \xi e^{-2i\boldsymbol{k}_j^{\mathrm{inv}}\cdot W_i}$. In other

words, $|w_{\xi,\boldsymbol{R}}(W_i)\rangle$ generates $n_\pm(\boldsymbol{k}_j^{\mathrm{inv}}) = \frac{1}{2}(1 \pm \xi \eta_{ij})$ Bloch states with parity ± 1 at $\boldsymbol{k}_j^{\mathrm{inv}}$.

2. Properties of η_{ij}

Since $\boldsymbol{k}_i^{\mathrm{inv}} = 2\pi W_i$ and $\frac{2}{\pi}\boldsymbol{k}_i^{\mathrm{inv}} \cdot W_j \in \mathbb{Z}$, $\eta_{ij} = e^{-2i\boldsymbol{k}_i^{\mathrm{inv}} \cdot W_j}$ satisfies

$$\eta_{ij} = \eta_{ji} = \eta_{ij}^{-1} \qquad (\text{B4})$$

and

$$\sum_{i=1}^{2^d} \eta_{ij} = 2^d \delta_{1j}, \quad \sum_{l=1}^{2^d} \eta_{il}\eta_{lj} = 2^d \delta_{ij}. \qquad (\text{B5})$$

Let first us prove $\sum_{i=1}^{2^d} \eta_{ij} = 2^d \delta_{1j}$. When $j = 1$, all η_{i1} are equal to 1 because $W_1 = 0$ by definition. Thus, $\sum_{i=1}^{2^d} \eta_{i1} = \sum_{i=1}^{2^d} 1 = 2^d$. When $j \neq 1$, η_{ij} always has a partner $\eta_{i'j} = -\eta_{ij}$ for some i'. Therefore, $\sum_{i=1}^{2^d} \eta_{ij}$ is zero. Combining the above relations, we obtain $\sum_{i=1}^{2^d} \eta_{ij} = 2^d \delta_{j1}$.

In a similar manner, one can prove that $\sum_{l=1}^{2^d} \eta_{il}\eta_{lj} = \sum_{l=1}^{2^d} e^{-2i(\boldsymbol{k}_i^{\mathrm{inv}} - \boldsymbol{k}_j^{\mathrm{inv}}) \cdot W_l} = 2^d \delta_{ij}$. The proof is trivial when $i = j$. When $i \neq j$, either $\boldsymbol{k}_i^{\mathrm{inv}}$ or $\boldsymbol{k}_j^{\mathrm{inv}}$ is nonzero. Let us assume that $\boldsymbol{k}_i^{\mathrm{inv}} \neq 0$ without loss of generality. Then, $\eta_{il}\eta_{lj} = e^{-2i(\boldsymbol{k}_i^{\mathrm{inv}} - \boldsymbol{k}_j^{\mathrm{inv}}) \cdot W_l}$ always has a partner $\eta_{il'}\eta_{l'j} = -\eta_{il}\eta_{lj}$ for some l'. The summation of $\eta_{il}\eta_{lj}$ over l thus vanishes.

3. Derivation of the mapping A_d

We derive the matrix A_d that relates the number of the Wannier sates in real space to the number of occupied states of even and odd parity in momentum space. As we show in the first subsection, $|w_{\xi,\boldsymbol{R}}(W_i)\rangle$ generates $n_\pm(\boldsymbol{k}_j^{\mathrm{inv}}) = \frac{1}{2}(1 \pm \xi\eta_{ij})$ Bloch states with parity ± 1 at $\boldsymbol{k}_j^{\mathrm{inv}}$, a set of Wannier states $\sum_{W,\xi} \mu_{W,\xi} w_\xi(W)$ produces

$$n_\pm(\boldsymbol{k}_i^{\mathrm{inv}}) = \sum_{j=1}^{2^d} \sum_{\xi=\pm} \frac{1}{2}(1 \pm \xi\eta_{ij})\mu_{W_j,\xi}$$

$$= \frac{1}{2}\sum_{j=1}^{2^d} \sum_{\xi=\pm} \mu_{W_j,\xi} \pm \frac{1}{2}\sum_{j=1}^{2^d} \eta_{ij}\sum_{\xi=\pm} \xi\mu_{W_j,\xi}$$

$$= \frac{1}{2}n_{\mathrm{occ}} \mp \frac{1}{2}\sum_{j=1}^{2^d} \eta_{ij}\nu_{W_j}. \qquad (\text{B6})$$

Thus, we obtain

$$n_-(\boldsymbol{k}_i^{\mathrm{inv}}) - n_+(\boldsymbol{k}_i^{\mathrm{inv}}) = \sum_{j=1}^{2^d} \eta_{ij}\nu_{W_j}. \qquad (\text{B7})$$

Equivalently, $\nu_{W_i} = \sum_{j=1}^{2^d} 2^{-d}\eta_{ij}[n_-(\boldsymbol{k}_i^{\mathrm{inv}}) - n_+(\boldsymbol{k}_i^{\mathrm{inv}})]$ because $\eta^{-1} = 2^{-d}\eta$ in the matrix notation as shown in

Eqs. (B4) and (B5). We introduce a new notation A_d by

$$\begin{pmatrix} \nu_{W_1} \\ \nu_{W_2} \\ \nu_{W_3} \\ \vdots \\ \nu_{W_{2^d}} \end{pmatrix} = A_d \begin{pmatrix} n_-(\boldsymbol{k}_1^{\mathrm{inv}}) - n_+(\boldsymbol{k}_1^{\mathrm{inv}}) \\ n_-(\boldsymbol{k}_2^{\mathrm{inv}}) - n_+(\boldsymbol{k}_2^{\mathrm{inv}}) \\ n_-(\boldsymbol{k}_3^{\mathrm{inv}}) - n_+(\boldsymbol{k}_3^{\mathrm{inv}}) \\ \vdots \\ n_-(\boldsymbol{k}_{2^d}^{\mathrm{inv}}) - n_+(\boldsymbol{k}_{2^d}^{\mathrm{inv}}) \end{pmatrix}, \qquad (\text{B8})$$

where

$$[A_d]_{ij} = \frac{1}{2^d}\eta_{ij} = \frac{1}{2^d}\exp(2i\boldsymbol{k}_i^{\mathrm{inv}} \cdot W_j). \qquad (\text{B9})$$

From Eqs. (B4) and (B5), one can find that A_d satisfies

$$A_d^{-1} = 2^d A_d, \quad A_d^T = A_d, \quad \sum_{i=1}^{2^d}[A_d]_{ij} = \delta_{j,1}. \qquad (\text{B10})$$

For later use, we write Eq. (B8) in another form,

$$\begin{pmatrix} \nu_{W_1} + n_{\mathrm{occ}} \\ \nu_{W_2} \\ \nu_{W_3} \\ \vdots \\ \nu_{W_{2^d}} \end{pmatrix} = 2A_d \begin{pmatrix} n_-(\boldsymbol{k}_1^{\mathrm{inv}}) \\ n_-(\boldsymbol{k}_2^{\mathrm{inv}}) \\ n_-(\boldsymbol{k}_3^{\mathrm{inv}}) \\ \vdots \\ n_-(\boldsymbol{k}_{2^d}^{\mathrm{inv}}) \end{pmatrix} \qquad (\text{B11})$$

by using $n_+(\boldsymbol{k}_i^{\mathrm{inv}}) + n_-(\boldsymbol{k}_i^{\mathrm{inv}}) = n_{\mathrm{occ}}$.

Also, A_{d+1} and A_d have a recursion relation

$$A_{d+1} = \frac{1}{2}\begin{pmatrix} A_d & A_d \\ A_d & -A_d \end{pmatrix}. \qquad (\text{B12})$$

This can be easily proven by using $\frac{1}{\pi}(\boldsymbol{k}_{i+2^d}^{\mathrm{inv}} - \boldsymbol{k}_i^{\mathrm{inv}}) = 2(W_{i+2^d} - W_i) = (0, \ldots, 0, 1)$ for $i = 1, \ldots, 2^d$.

4. Properties of ν_W

As $n_\xi(\boldsymbol{k}^{\mathrm{inv}})$ must be an integer which satisfies $0 \leqslant n_\xi(\boldsymbol{k}^{\mathrm{inv}}) \leqslant n_{\mathrm{occ}}$, $\{\nu_W\}$ cannot take any values. Most importantly, $\{\nu_W\}$ satisfy

$$\left|\sum_{j=1}^{2^d}[A_d]_{ij}\nu_{W_j}\right| = \frac{1}{2^d}n, \qquad (\text{B13})$$

where n is an integer less than or equal to n_{occ}, according to Eq. (B6). Also, ν_W indices have the following properties:

$$
\begin{aligned}
&a. & 2^{d-1}\nu_{W_i} &\in \mathbb{Z}, \\
&b. & 2^{d-2}(\nu_{W_i} \pm \nu_{W_{j\neq i}}) &\in \mathbb{Z}, \\
&c. & |\nu_{W_i}| &\leqslant n_{\mathrm{occ}}, \qquad (\text{B14}) \\
&d. & |\nu_{W_i} \pm \nu_{W_j}| &\leqslant n_{\mathrm{occ}}, \\
&e. & \left|\sum_W \nu_W\right| &\leqslant n_{\mathrm{occ}}.
\end{aligned}
$$

a. Proof of $2^{d-1}\nu_{W_i} \in \mathbb{Z}$. As $n_-(\boldsymbol{k}^{\mathrm{inv}})$ is an integer greater than or equal to zero and A_d satisfies $2^d[A_d]_{ij} = \pm 1$,

$\nu_{W_i} = \sum_{j=1}^{2^d} 2[A_d]_{ij} n_-(\boldsymbol{k}_j^{\mathrm{inv}})$ (mod 1) in Eq. (B11) implies

$$2^{d-1} \nu_{W_i} \in \mathbb{Z}. \qquad (B15)$$

b. Proof of $2^{d-2}(\nu_{W_i} \pm \nu_{W_j}) \in \mathbb{Z}$. From $2^{d-1}([A_d]_{ij} \pm [A_d]_{i'j}) = 0$ or ± 1, it follows that $\nu_{W_i} \pm \nu_{W_{i'}} = \sum_{j=1}^{2^d} 2([A_d]_{ij} \pm [A_d]_{i'j}) n_-(\boldsymbol{k}_j^{\mathrm{inv}})$ for $i, i' \neq 1$, which implies

$$2^{d-2}(\nu_{W_i} \pm \nu_{W_{i'}}) \in \mathbb{Z} \qquad (B16)$$

when $i, i' \neq 1$. Similarly, $\nu_{W_1} \pm \nu_{W_i} = \sum_{j=1}^{2^d} 2([A_d]_{1j} \pm [A_d]_{ij}) n_-(\boldsymbol{k}_j^{\mathrm{inv}}) - n_{\mathrm{occ}}$ for $i \neq 1$ implies

$$2^{d-2}(\nu_{W_1} \pm \nu_{W_i}) \in \mathbb{Z}. \qquad (B17)$$

Thus, we obtain $2^{d-2}(\nu_{W_i} \pm \nu_{W_j}) \in \mathbb{Z}$ for $i \neq j$. This completes the proof because when $i = i'$ the property *b* reduces to the property *a*, which we prove above.

c. Proof of $|\nu_{W_i}| \leqslant n_{\mathrm{occ}}$. Let us first prove $|\nu_{W_1}| \leqslant n_{\mathrm{occ}}$. From Eqs. (B10) and (B11), we obtain

$$|\nu_{W_1}| = \left| 2 \sum_{j=1}^{2^d} [A_d]_{1j} n_-(\boldsymbol{k}_j^{\mathrm{inv}}) - n_{\mathrm{occ}} \right|$$

$$= \left| 2 n_-(\boldsymbol{k}_1^{\mathrm{inv}}) - n_{\mathrm{occ}} \right| \leqslant n_{\mathrm{occ}}. \qquad (B18)$$

Thus, $|\nu_{W_1}| \leqslant n_{\mathrm{occ}}$. We can prove $|\nu_{W_i}| \leqslant n_{\mathrm{occ}}$ for $i \neq 1$ in a similar way. For $i \neq 1$, the number of $[A_d]_{ij} = \pm \frac{1}{2^d}$ is equal. Let us relabel the j indices such that $[A_d]_{ij} = \frac{1}{2^d}$ for $j = 1, \ldots, 2^{d-1}$ and $-\frac{1}{2^d}$ for $j = 2^{d-1} + 1, \ldots, 2^d$. Then, we obtain

$$|\nu_{W_i}| = 2 \left| \sum_{j=1}^{2^d} [A_d]_{ij} n_-(\boldsymbol{k}_j^{\mathrm{inv}}) \right|$$

$$= 2^{1-d} \sum_{j=1}^{2^{d-1}} \left| n_-(\boldsymbol{k}_j^{\mathrm{inv}}) - n_-(\boldsymbol{k}_{j+2^{d-1}}^{\mathrm{inv}}) \right|$$

$$\leqslant n_{\mathrm{occ}}. \qquad (B19)$$

d. Proof of $|\nu_{W_i} \pm \nu_{W_{j \neq i}}| \leqslant n_{\mathrm{occ}}$. Let us first prove $|\nu_{W_1} \pm \nu_{W_{i \neq 1}}| \leqslant n_{\mathrm{occ}}$. We can relabel the j indices for given i such that $[A_d]_{ij} = \pm \frac{1}{2^d}$ for $j = 1, \ldots, 2^{d-1}$ and $\mp \frac{1}{2^d}$ for $j = 2^{d-1} + 1, \ldots, 2^d$. Then, $2^{d-1}([A_d]_{1j} \pm [A_d]_{ij}) = 1$ for $j = 1, \ldots, 2^{d-1}$ and 0 for $j = 2^{d-1} + 1, \ldots, 2^d$. Thus,

$$\left| \nu_{W_1} \pm \nu_{W_i} \right| = \left| 2 \sum_{j=1}^{2^d} ([A_d]_{1j} \pm [A_d]_{ij}) n_-(\boldsymbol{k}_j^{\mathrm{inv}}) - n_{\mathrm{occ}} \right|$$

$$= \left| 2^{2-d} \sum_{j=1}^{2^{d-1}} n_-(\boldsymbol{k}_j^{\mathrm{inv}}) - n_{\mathrm{occ}} \right| \leqslant n_{\mathrm{occ}}. \qquad (B20)$$

When $i, i' \neq 1$ and $i \neq i'$, we can relabel the j indices such that $2^{d-1}([A_d]_{ij} \pm [A_d]_{i'j}) = 1$ for $j = 1, \ldots, 2^{d-2}$, -1 for $j = 2^{d-2} + 1, \ldots, 2^{d-1}$, and 0 for $j = 2^{d-1}, \ldots, 2^d$. The relabeling of j indices is achieved as follows. Since both $\boldsymbol{k}_i^{\mathrm{inv}}$ and $\boldsymbol{k}_{i'}^{\mathrm{inv}}$ are inversion-invariant momenta, so is $\boldsymbol{k}_{i'}^{\mathrm{inv}} - \boldsymbol{k}_i^{\mathrm{inv}}$. Thus, we can write it as $\boldsymbol{k}_{i'}^{\mathrm{inv}} - \boldsymbol{k}_i^{\mathrm{inv}} = \frac{\Delta \boldsymbol{G}}{2}$ where $\Delta \boldsymbol{G}$ is a reciprocal lattice vector. Then, $\eta_{ij} \pm \eta_{i'j} = \eta_{ij}[1 \pm \exp(i \Delta \boldsymbol{G} \cdot W_j)]$,

thus, $\eta_{ij} \pm \eta_{i'j} = 0$ for $j = 2^{d-1} + 1, \ldots, 2^d$ after the relabeling of j indices. From $\sum_j \eta_{ij} \pm \eta_{i'j} = 0$, $\eta_{ij} \pm \eta_{i'j} = \pm 1$ are equally distributed, say $\eta_{ij} \pm \eta_{i'j} = 1$ for $j = 1, \ldots, 2^{d-2}$ and -1 for $j = 2^{d-2} + 1, \ldots, 2^{d-1}$. Finally,

$$\left| \nu_{W_i} \pm \nu_{W_{i'}} \right| = \left| 2 \sum_{j=1}^{2^d} ([A_d]_{ij} \pm [A_d]_{i'j}) n_-(\boldsymbol{k}_j^{\mathrm{inv}}) \right|$$

$$= \left| 2^{2-d} \sum_{j=1}^{2^{d-2}} \left[n_-(\boldsymbol{k}_j^{\mathrm{inv}}) - n_-(\boldsymbol{k}_{j+2^{d-2}}^{\mathrm{inv}}) \right] \right|$$

$$\leqslant n_{\mathrm{occ}}. \qquad (B21)$$

e. Proof of $|\sum_W \nu_W| \leqslant n_{\mathrm{occ}}$. Using Eq. (B10), we obtain

$$\left| \sum_W \nu_W \right| = \left| 2 \sum_{i,j=1}^{2^d} [A_d]_{ij} n_-(\boldsymbol{k}_j^{\mathrm{inv}}) - n_{\mathrm{occ}} \right|$$

$$= \left| 2 n_-(\boldsymbol{k}_1^{\mathrm{inv}}) - n_{\mathrm{occ}} \right| \leqslant n_{\mathrm{occ}}. \qquad (B22)$$

APPENDIX C: RELATIONS BETWEEN ν_W INDICES AND SYMMETRY INDICATOR

Symmetry indicators are constructed from symmetry eigenvalues in momentum space, and these distinguish stable topological phases from fragile topological and atomic phases [11]. Here, we relate ν_W indices with inversion-symmetry indicators.

In d dimensions, one can define the $\mathbb{Z}_{2^{d-1}}$ symmetry indicator $z_{2^{d-1}}$ for inversion symmetry:

$$z_{2^{d-1}} = \frac{1}{2} \sum_{i=1}^{2^d} \left(n_+(\boldsymbol{k}_i^{\mathrm{inv}}) - n_-(\boldsymbol{k}_i^{\mathrm{inv}}) \right) \pmod{2^{d-1}}. \quad (C1)$$

To see why it is defined modulo 2^{d-1}, we connect it to ν_W indices. Let us recall that an atomic orbital localized at W_i with inversion parity ξ has parity $\xi \exp(2i \boldsymbol{k}_j^{\mathrm{inv}} \cdot W_i)$ at inversion-invariant momentum $\boldsymbol{k}_j^{\mathrm{inv}}$. Therefore, we have

$$z_{2^{d-1}} = \frac{1}{2} \sum_{i=1}^{2^d} \left(n_+(\boldsymbol{k}_i^{\mathrm{inv}}) - n_-(\boldsymbol{k}_i^{\mathrm{inv}}) \right)$$

$$= -\frac{1}{2} \sum_{i,j=1}^{2^d} \eta_{ij} \nu_{W_j}$$

$$= -2^{d-1} \nu_{W_1} \pmod{2^{d-1}},$$

where Eqs. (B7) and (B5) are used in the first and second lines. Since all fragile topological and atomic phases have ν_W indices as integers so that they have trivial $z_{2^{d-1}}$ indicator, $z_{2^{d-1}} = 0$, this indicator is nontrivial only for stable topological phases.

While only ν_{W_1} determines the strong index $z_{2^{d-1}}$, other ν_W indices are related to the weak indices $z^{(w)}$. For example, in two dimensions, $\nu_{W_i} \pm \nu_{W_j}$ are constrained to be integers as shown in Appendix B. Thus, all stable topological phases detected by $\nu_A = \frac{1}{2}$ modulo 1 have $\nu_{B,C,D}$ as half-integers. Thus, $\nu_{B,C,D}$ do not form additional symmetry indicators. This follows from the fact that there

is no weak topology in two dimensions because there is no Wannier obstruction coming from the 1D band topology: all 1D insulators are atomic insulators. On the other hand, we have three $\mathbb{Z}_2$ weak indices in three dimensions, $z_{i=1,2,3}^{(w)}$ [92]. These generate seven distinct weak topological phases characterized by $(z_1^{(w)}, z_2^{(w)}, z_3^{(w)}) = (0,0,1)$, $(0,1,0)$, $(1,0,0)$, $(1,1,0)$, $(1,0,1)$, $(0,1,1)$, $(1,1,1)$. The weak symmetry indicators

$$z_1^{(w)} = \frac{1}{2} \sum_{i=2,4,6,8} \left[\left(n_+\left(k_i^{\text{inv}}\right) - n_-\left(k_i^{\text{inv}}\right) \right) \right] \pmod 2,$$

$$z_2^{(w)} = \frac{1}{2} \sum_{i=3,4,7,8} \left[\left(n_+\left(k_i^{\text{inv}}\right) - n_-\left(k_i^{\text{inv}}\right) \right) \right] \pmod 2, \quad \text{(C2)}$$

$$z_3^{(w)} = \frac{1}{2} \sum_{i=5,6,7,8} \left[\left(n_+\left(k_i^{\text{inv}}\right) - n_-\left(k_i^{\text{inv}}\right) \right) \right] \pmod 2$$

are expressed by ν_{W_1}, ν_{W_2}, ν_{W_3}, and ν_{W_5} as follows:

$$z_1^{(w)} = 2\left(\nu_{W_1} - \nu_{W_2}\right) \pmod 2,$$

$$z_2^{(w)} = 2\left(\nu_{W_1} - \nu_{W_3}\right) \pmod 2, \quad \text{(C3)}$$

$$z_3^{(w)} = 2\left(\nu_{W_1} - \nu_{W_5}\right) \pmod 2.$$

Note that symmetry-indicated stable topological phases can be either insulators or semimetals [11]. For example, in three dimensions, the phase is gapless when the strong indicator z_4 is odd [79,80].

APPENDIX D: FILLING ANOMALY FROM INVERSION OF MINIMAL NUMBER OF BANDS CORRESPONDING TO dD $(d+1)$th-order DIRAC HAMILTONIAN

In this Appendix, we discuss how an odd number of band inversions corresponding to dD $(d+1)$th-order Dirac Hamiltonian generates the filling anomaly. Here, we mean a band inversion at inversion-invariant momentum k_i^{inv} by a change of parity configuration by $\Delta n_-(k_i^{\text{inv}}) = \pm 2^{d-1}$. A change of ν_W indices due to a band inversion at k_i^{inv}, $\Pi(k_i^{\text{inv}})$, is readily obtained from Eq. (39):

$$\Pi_i\left(k_j^{\text{inv}}\right) = \Pi_j\left(k_i^{\text{inv}}\right) = \pm\eta_{ij} = \pm\exp\left(2ik_i^{\text{inv}} \cdot W_j\right). \quad \text{(D1)}$$

Here, $\pm$ corresponds to $\Delta n_-(k_i^{\text{inv}}) = \pm 2^{d-1}$. For example, band inversions at k_1^{inv} and k_2^{inv} in 3D correspond to $\Pi(k_1^{\text{inv}}) = \pm\{1,1,1,1,1,1,1,1\}$ and $\Pi(k_2^{\text{inv}}) = \pm\{1,-1,1,-1,1,-1,1,-1\}$, respectively. Since $\Pi_i(k_j^{\text{inv}}) = \pm 1$, changes in ν_{W_i} for $i = 1, \ldots, 2^d$ are odd (even) integers simultaneously when the band inversions occur odd (even) number of times.

First, let us suppose that we have an insulator without the filling anomaly, i.e., ν_{W_i} are even integers for $i = 2, \ldots, 2^d$. After an odd (even) number of band inversions, ν_{W_i} become odd (even) integers for $i = 2, \ldots, 2^d$ and this implies the presence (absence) of the filling anomaly. Likewise, an odd (even) number of band inversions implies the absence (presence) of the filling anomaly when we start from an insulator with the filling anomaly, i.e., ν_{W_i} are odd integers for $i = 2, \ldots, 2^d$.

Conversely, any inversion-symmetric insulators with (without) the filling anomaly become atomic insulator with-

out (with) the filling anomaly after an odd (even) number of band inversions. For example, when $n_{\text{occ}} = 6$, $\{\nu_W\} = \{-1, 1, 3, 1, 1, -1, 1, 1\}$ has the following parity configuration:

k_1^{inv}	k_2^{inv}	k_3^{inv}	k_4^{inv}	k_5^{inv}	k_6^{inv}	k_7^{inv}	k_8^{inv}
−	−	+	−	−	−	−	+
−	−	+	−	−	−	−	+
−	−	+	+	−	+	+	+
−	−	+	+	−	+	+	+
−	+	+	+	+	+	+	+
−	+	+	+	+	+	+	+

(D2)

We always reorder the energy levels so that odd-parity states are atop even-parity states. After the band inversions at $k_{1,2,5}^{\text{inv}}$, ν_W indices change by $-\sum_{i=1,2,5} \Pi(k_i^{\text{inv}})$, thus $\{\nu_W\} = \{-4, 0, 0, 0, 0, 0, 0, 2\}$:

k_1^{inv}	k_2^{inv}	k_3^{inv}	k_4^{inv}	k_5^{inv}	k_6^{inv}	k_7^{inv}	k_8^{inv}
−	+	+	−	+	−	−	+
−	+	+	−	+	−	−	+
+	+	+	+	+	+	+	+
+	+	+	+	+	+	+	+
+	+	+	+	+	+	+	+
+	+	+	+	+	+	+	+

(D3)

Now the parity configuration is equivalent to $4s(W_1) \oplus 2p(W_8)$, which is an atomic insulator without the filling anomaly. Hence, the number of band inversions modulo 2, which is equal to $N_{\text{BI}} = \sum_{i=1}^{2^d} \lfloor \frac{n_-(k_i^{\text{inv}})}{2^{d-1}} \rfloor \pmod 2$, determines the filling anomaly, i.e., $N_{\text{BI}} = 0$ ($N_{\text{BI}} = 1$) for the absence (presence) of the filling anomaly. Here, $\lfloor x \rfloor$ denotes the greatest integer less than or equal to x.

APPENDIX E: LAYER CONSTRUCTION OF INVERSION-SYMMETRIC TIs AND TSCs

Inversion-symmetric kth-order TIs/TSCs for $k \leqslant d$ in d dimensions can be constructed by staking first-order TIs/TSCs in $(d - k + 1)$ dimensions [44]. Based on the layer construction, higher-order topological phases protected by inversion symmetry are neatly summarized in Table IX, which is reproduced from Ref. [44]. On the other hand, it was pointed out in Refs. [52,63,64] that topological phases without gapless boundary states are given by the layer construction starting from 0D states. In this way, any dD systems are constructed by stacking 0D states (see Fig. 14). Here, we extended the layer construction in Ref. [44] to the case for $k > d$, where no gapless boundary states appear. We focus
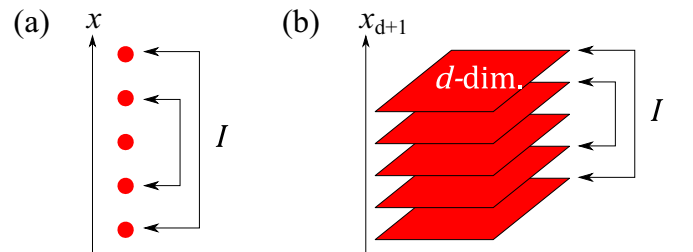

FIG. 14. Layer construction. (a) Stacking 0D systems gives a 1D system. (b) Stacking dD systems gives a $(d+1)$D system.

TABLE IX. Classification of generic higher-order TIs/TSCs protected by inversion symmetry [44]. Among the 10 AZ classes, classes A and AIII belong to complex AZ classes while the other eight classes belong to real AZ classes. s labels the AZ classes: $s = 0, 1$ for complex AZ classes and $s = 0, 1, \dots, 7$ for real AZ classes. T, P, and S denote time-reversal, particle-hole, and chiral symmetries. T^2 are denoted as 0 when the symmetry is absent. The same notation is adopted for P and S. Inversion-symmetry operator I satisfies $[I, T] = \{I, P\} = 0$. δ is given by dimension d and order k, $\delta = d - k + 1$ (mod 8). Here, k is an arbitrary positive integer. As for $\mathbb{Z}_2$ and "$\mathbb{Z}_2$" classifications, $\mathbb{Z}_2$ and "$\mathbb{Z}_2$" nontrivial classes exhibit gapless boundary states when $k \leqslant d$. When $k = d + 1$, only "$\mathbb{Z}_2$" nontrivial classes exhibit the filling anomaly.

AZ class	s	T^2	P^2	S^2	$\delta = 0$	$\delta = 1$	$\delta = 2$	$\delta = 3$	$\delta = 4$	$\delta = 5$	$\delta = 6$	$\delta = 7$
A	0	0	0	0	"$\mathbb{Z}_2$"	0	$\mathbb{Z}_2$	0	$\mathbb{Z}_2$	0	$\mathbb{Z}_2$	0
AIII	1	0	0	1	0	$\mathbb{Z}_2$	0	$\mathbb{Z}_2$	0	$\mathbb{Z}_2$	0	$\mathbb{Z}_2$
AI	0	1	0	0	"$\mathbb{Z}_2$"	0	0	0	$\mathbb{Z}_2$	0	$\mathbb{Z}_2$	$\mathbb{Z}_2$
BDI	1	1	1	1	$\mathbb{Z}_2$	$\mathbb{Z}_2$	0	0	0	$\mathbb{Z}_2$	0	$\mathbb{Z}_2$
D	2	0	1	0	$\mathbb{Z}_2$	$\mathbb{Z}_2$	$\mathbb{Z}_2$	0	0	0	$\mathbb{Z}_2$	0
DIII	3	−1	1	1	0	$\mathbb{Z}_2$	$\mathbb{Z}_2$	$\mathbb{Z}_2$	0	0	0	$\mathbb{Z}_2$
AII	4	−1	0	0	"$\mathbb{Z}_2$"	0	$\mathbb{Z}_2$	$\mathbb{Z}_2$	$\mathbb{Z}_2$	0	0	0
CII	5	−1	−1	1	0	$\mathbb{Z}_2$	0	$\mathbb{Z}_2$	$\mathbb{Z}_2$	$\mathbb{Z}_2$	0	0
C	6	0	−1	0	0	0	$\mathbb{Z}_2$	0	$\mathbb{Z}_2$	$\mathbb{Z}_2$	$\mathbb{Z}_2$	0
CI	7	1	−1	1	0	0	0	$\mathbb{Z}_2$	0	$\mathbb{Z}_2$	$\mathbb{Z}_2$	$\mathbb{Z}_2$

on the case where inversion-symmetry operator I satisfies the commutation relations with T and P in the same way as the Hamiltonian, i.e., $[I, T] = 0$ and $\{I, P\} = 0$. When I satisfies commutation relations different from that of H, only order of $k \leqslant 2$ or 3 can be realized depending on the AZ classes, and we refer readers to [44,52] for discussions about such cases.

The layer construction can be employed to construct the Hamiltonian for generalized kth-order TIs/TSCs with $k > d$ as was done for $k \leqslant d$ in Ref. [44]. Before introducing a dimensional raising mapping of Hamiltonian based on the layer construction, we adopt the following convention:

(1) $\mathcal{H}_{(d,k)}$ and $I_{(d,k)}$ denote the Dirac Hamiltonian and inversion-symmetry operator of dD kth-order TI/TSC.

(2) $T_{(d,k)}$, $P_{(d,k)}$, and $S_{(d,k)}$ denote time-reversal, particle-hole, and chiral symmetry operators for dD kth-order TI/TSC. These nonspatial symmetries exist or not according to the AZ class.

(3) $\mathcal{M}_{(d,k)}$ denotes the bulk mass term and satisfies

$$[I_{(d,k)}, \mathcal{M}_{(d,k)}] = 0, \quad [T_{(d,k)}, \mathcal{M}_{(d,k)}] = 0,$$
$$\{P_{(d,k)}, \mathcal{M}_{(d,k)}\} = 0, \quad \{S_{(d,k)}, \mathcal{M}_{(d,k)}\} = 0. \quad \text{(E1)}$$

Given a Hamiltonian $\mathcal{H}_{(d,k)}$, $\mathcal{H}_{(d+1,k+1)}$ is obtained by the dimensional raising mapping

$$\mathcal{H}_{(d+1,k+1)} = \mathcal{H}_{(d,k)} \otimes \tau_z + k_{d+1}\,\tau_x + m_{k,\boldsymbol{r}}\,\tau_y, \quad \text{(E2)}$$

where $m_{k,\boldsymbol{r}} = -m_{k,-\boldsymbol{r}}$ denotes the boundary mass term. Note that the boundary mass terms $m_{a,\boldsymbol{r}}$, for $a = 1, \dots, k - 1$, in $\mathcal{H}_{(d,k)}$ are deformed to be odd under inversion symmetry in $(d + 1)$D once the dimensional raising mapping (E2) is done. The symmetry operators of $(d + 1)$D $(k + 1)$th-order TI/TSC are given by

$$I_{(d+1,k+1)} = I_{(d,k)} \otimes \tau_z,$$
$$T_{(d+1,k+1)} = T_{(d,k)} \otimes \tau_z,$$
$$P_{(d+1,k+1)} = P_{(d,k)} \otimes \tau_0,$$
$$S_{(d+1,k+1)} = S_{(d,k)} \otimes \tau_z, \quad \text{(E3)}$$

thus, the dimensional raising mapping (E2) does not change the AZ class. Note that Eq. (E2) is understood as a continuum

limit of

$$H_{(d+1,k+1)} = H_{(d,k)} \otimes \tau_z - (1 - \cos k_{d+1}) \mathcal{M}_{(d+1,k+1)}$$
$$+ \sin k_{d+1}\, \tau_x, \quad \text{(E4)}$$

where $\mathcal{M}_{(d+1,k+1)} = \mathcal{M}_{(d,k)} \otimes \tau_z$. Accordingly, the Hamiltonian for dD $(d + n)$th-order TI/TSC, $\mathcal{H}_{(d,d+n)}$ for $n > 0$ and $d \geqslant 1$, is constructed by a "0D nth-order" Hamiltonian $\mathcal{H}_{(0,n)}$ by using the dimensional raising mapping repeatedly:

$$\mathcal{H}_{(d,d+n)} = \sum_{i=1}^{d} k_i \Gamma_i + \lambda \mathcal{M}_{(d,d+n)} + \sum_{a=1}^{d+n-1} m_{a,\boldsymbol{r}} \Gamma_{a+d}. \quad \text{(E5)}$$

We define a 0D nth-order Hamiltonian $\mathcal{H}_{(0,n)}$,

$$\mathcal{H}_{(0,n)} = \lambda \mathcal{M}_{(0,n)} + \sum_{a=1}^{n-1} m_{a,\boldsymbol{R}} \Gamma_a, \quad \text{(E6)}$$

where $\boldsymbol{R}$ is regarded as a set of auxiliary parameters that are promoted to $\boldsymbol{r}$ after the construction of $\mathcal{H}_{(d,d+n)}$ is done. Thus, $m_{a,\boldsymbol{R}}$ transforms under the symmetry operators

$$I : \quad m_{a,\boldsymbol{R}} \to -m_{a,\boldsymbol{R}},$$
$$T : \quad m_{a,\boldsymbol{R}} \to m_{a,\boldsymbol{R}},$$
$$P : \quad m_{a,\boldsymbol{R}} \to m_{a,\boldsymbol{R}},$$
$$S : \quad m_{a,\boldsymbol{R}} \to m_{a,\boldsymbol{R}}. \quad \text{(E7)}$$

Now, let us regard $m_{a,\boldsymbol{R}}$ as momentumlike variables. Then, T and P can be regarded as space-time inversion symmetry and particle-hole symmetry combined with inversion symmetry. Hence, the 0D Hamiltonian $\mathcal{H}_{(0,n)}$ is identical to the inversion-symmetric $(n - 1)$D Dirac Hamiltonian in the presence/absence of IT, IP, and S [87]. Therefore, n is allowed when $n + s = 1$ (mod 2) in complex AZ classes, and $n + s = 1, 2, 3, 5$ (mod 8) in real AZ classes where $s = 0, 1$ (mod 2) and $s = 0, \dots, 7$ (mod 8) label the complex and real AZ classes, respectively. This is summarized in Table IX, and it is identical to the classification table for $k \geqslant d$ in Ref. [44]. Therefore, our analysis generalizes Table IX to arbitrary non-negative integers k and d. Here, the inversion-protected

dD kth-order topology has a $\mathbb{Z}_2$ classification because a two-copy of dD kth-order TIs is not a dD kth-order TI anymore. Instead, it has a higher order. In our Dirac Hamiltonian construction in class A, a two-copy of dD kth-order TIs gives dD $(k + 2)$th-order TI. For example, in class AII, a two-copy of dD $(d + 1)$th-order TIs gives dD $(d + 5)$th-order TI.

APPENDIX F: BOUNDARY PROJECTION

In this Appendix, we review the boundary projection introduced in Refs. [43,44,46,52]. Consider the Dirac Hamiltonian in d dimensions $\mathcal{H}(\boldsymbol{r})$:

$$\mathcal{H}(\boldsymbol{r}) = -i \sum_{i=1}^{d} \partial_i \Gamma_i + \lambda(\boldsymbol{r})\mathcal{M}. \tag{F1}$$

Here, $\Gamma_{i=1,\ldots,d}$ are gamma matrices and $\mathcal{M}$ is bulk mass term. Gamma matrices Γ_i and the bulk mass term $\mathcal{M}$ satisfy $\{\Gamma_i, \Gamma_j\} = 2\delta_{ij}$ and $\{\Gamma_i, \mathcal{M}\} = 0$. We consider a system that is in the topological phase. Let us take $\lambda > 0$ in the topological phase and $\lambda < 0$ in the trivial phase. Then, λ is positive inside the system while λ is negative outside the system. We set $\lambda(\boldsymbol{r})$ such that it approaches to $+1$ as $\boldsymbol{r}$ approaches the center of the system, $\boldsymbol{r} = 0$, and it approaches to -1 as $\boldsymbol{r}$ goes to infinity. On the boundary, $\lambda = 0$ because λ changes sign there.

For our analysis of the boundary theory of the Dirac Hamiltonian, we define $(d - 1)$ orthonormal tangent basis vector $\boldsymbol{e}_{r,L=1,\ldots,d-1}$ and the normal vectors $\boldsymbol{n}_r$. On the tangent space at $\boldsymbol{r}$, the Dirac Hamiltonian in Eq. (F1) is expressed as

$$\mathcal{H}_\perp(\boldsymbol{k}_S, \boldsymbol{r}) = \boldsymbol{k}_S \cdot \boldsymbol{\Gamma} - i(\boldsymbol{n}_r \cdot \boldsymbol{\Gamma})\partial_{x_\perp} + \lambda(x_\perp)\mathcal{M}. \tag{F2}$$

Here, $\boldsymbol{k}_S$ denotes the boundary momentum normal to $\boldsymbol{n}_r$, $\boldsymbol{k}_S = \boldsymbol{k} - (\boldsymbol{k} \cdot \boldsymbol{n}_r)\boldsymbol{n}_r$. Also, we use the vector notation for gamma matrices $\boldsymbol{\Gamma} = (\Gamma_1, \ldots, \Gamma_d)$, and $x_\perp$ denotes the normal coordinate at $\boldsymbol{r}$ on the boundary $\delta x_\perp = \boldsymbol{n}_r \cdot \delta \boldsymbol{r}$. Note that the kinetic term, the first term in Eq. (F2), can be expressed in terms of $\boldsymbol{e}_{r,L}$:

$$\boldsymbol{k}_S \cdot \boldsymbol{\Gamma} = \sum_{L=1}^{d-1} (\boldsymbol{k}_S)_L (\boldsymbol{e}_{r,L} \cdot \boldsymbol{\Gamma}), \tag{F3}$$

where $(\boldsymbol{k}_S)_L = \boldsymbol{k}_S \cdot \boldsymbol{e}_{r,L}$.

When the system is sufficiently large, $\mathcal{H}_\perp(\boldsymbol{k}_S, \boldsymbol{r})$ has eigenstate $\psi(\boldsymbol{k}_S, \boldsymbol{r})$ that is exponentially localized on the boundary. One can show that the Schrödinger equation

$$\mathcal{H}_\perp(\boldsymbol{k}_S, \boldsymbol{r})\psi(\boldsymbol{k}_S, \boldsymbol{r}) = E(\boldsymbol{k}_S)\psi(\boldsymbol{k}_S, \boldsymbol{r}) \tag{F4}$$

is solved by the following ansatz:

$$\psi(\boldsymbol{k}_S, \boldsymbol{r}) = e^{\int^{x_\perp} dt\, \lambda(t)} P_+(\boldsymbol{r})\tilde{\psi}(\boldsymbol{k}_S), \tag{F5}$$

where we define projection operators $P_\pm(\boldsymbol{r}) = \frac{1}{2}[\mathbb{1} \mp i(\boldsymbol{n}_r \cdot \boldsymbol{\Gamma})\mathcal{M}]$ is projection operator. The choice of projection operator $P_+(\boldsymbol{r})$ or $P_-(\boldsymbol{r})$ depends on the profile of $\lambda(\boldsymbol{r})$. In our case, since $\lambda = -1$ outside the system, $P_+(\boldsymbol{r})$ is the proper choice. $P_\pm(\boldsymbol{r})$ satisfies the following relation:

$$P_\pm(\boldsymbol{r})^2 = P_\pm(\boldsymbol{r}), \quad P_\pm(\boldsymbol{r})P_\mp(\boldsymbol{r}) = 0,$$
$$[P_\pm(\boldsymbol{r}), \boldsymbol{e}_{r,L} \cdot \boldsymbol{\Gamma}] = 0, \quad P_\pm(\boldsymbol{r})\mathcal{M} = \mathcal{M}P_\mp(\boldsymbol{r}), \tag{F6}$$
$$P_\pm(\boldsymbol{r})(\boldsymbol{n}_r \cdot \boldsymbol{\Gamma}) = (\boldsymbol{n}_r \cdot \boldsymbol{\Gamma})P_\mp(\boldsymbol{r}).$$

With the help of the ansatz in Eqs. (F5) and (F6), the eigenvalue problem in Eq. (F4) is reduced to the form

$$P_+(\boldsymbol{r})[\boldsymbol{k}_S \cdot \boldsymbol{\Gamma}]P_+(\boldsymbol{r})\tilde{\psi}(\boldsymbol{k}_S) = E(\boldsymbol{k}_S)\tilde{\psi}(\boldsymbol{k}_S), \tag{F7}$$

where we define the boundary Hamiltonian $h(\boldsymbol{k}_S, \boldsymbol{r}) \equiv P_+(\boldsymbol{r})\mathcal{H}_\perp(\boldsymbol{k}_S, \boldsymbol{r})P_+(\boldsymbol{r})$.

Now, we consider the kth-order topology, which is defined by the presence of $(k - 1)$ odd-parity mass terms $m_{a,\boldsymbol{r}}M_a$ with $a = 1, \ldots, k - 1$, where M_a satisfy $\{\Gamma_i, M_a\} = 0$, $\{\mathcal{M}, M_a\} = 0$, and $\{M_a, M_b\} = 2\delta_{ab}$. Inversion symmetry under $I = \mathcal{M}$ requires that $m_{a,\boldsymbol{r}}$ is odd under inversion, i.e., $m_{a,\boldsymbol{r}} = -m_{a,-\boldsymbol{r}}$. Those mass terms break translation symmetry because of their $\boldsymbol{r}$ dependence, and we assume that they are finite only near the boundary.

After the boundary mass terms are included, the boundary Hamiltonian becomes

$$h(\boldsymbol{k}_S, \boldsymbol{r}) = P_+(\boldsymbol{r})\left[\boldsymbol{k}_S \cdot \boldsymbol{\Gamma} + \sum_{a=1}^{k-1} m_{a,\boldsymbol{r}}M_a\right]P_+(\boldsymbol{r}). \tag{F8}$$

The eigenvalue problem for $h(\boldsymbol{k}_S, \boldsymbol{r})$ can be solved in the following way. The boundary-projected gamma matrices and mass matrices $\tilde{\Gamma}_L$ and $\tilde{M}_a$ are defined by the projection

$$\tilde{\Gamma}_L = P_+(\boldsymbol{r})(\boldsymbol{e}_{r,L} \cdot \boldsymbol{\Gamma})P_+(\boldsymbol{r}) = (\boldsymbol{e}_{r,L} \cdot \boldsymbol{\Gamma})P_+(\boldsymbol{r}),$$
$$\tilde{M}_a = P_+(\boldsymbol{r})M_a P_+(\boldsymbol{r}) = M_a P_+(\boldsymbol{r}), \tag{F9}$$

and satisfy $\{\tilde{\Gamma}_L, \tilde{\Gamma}_M\} = 2\delta_{LM}P_+(\boldsymbol{r})$, $\{\tilde{M}_a, \tilde{M}_b\} = 2\delta_{ab}P_+(\boldsymbol{r})$, and $\{\tilde{\Gamma}_L, \tilde{M}_a\} = 0$. Hence, energy eigenvalues are given by $E(\boldsymbol{k}_S, \boldsymbol{r}) = \pm\sqrt{\boldsymbol{k}_S^2 + \sum_{a=1}^{k-1} m_{a,\boldsymbol{r}}^2}$.

So far, the boundary-projected mass terms $m_{a,\boldsymbol{r}}\tilde{M}_a$ are generated by the position-dependent mass terms $m_{a,\boldsymbol{r}}M_a$. Alternatively, $m_{a,\boldsymbol{r}}\tilde{M}_a$ can be generated by a constant perturbation $\mathcal{H}_{\text{pert}}$ [46,52]

$$\mathcal{H}_{\text{pert}} = i \sum_{i=1}^{d} \sum_{a=1}^{k-1} \Delta_{i,a} \Gamma_i M_a \mathcal{M}. \tag{F10}$$

After the boundary projection, $\mathcal{H}_{\text{pert}}$ is reduced to

$$P_+(\boldsymbol{r})\,\mathcal{H}_{\text{pert}}\,P_+(\boldsymbol{r}) = \sum_{i=1}^{d} \sum_{a=1}^{k-1} \Delta_{i,a}\,\boldsymbol{n}_{r,i}\tilde{M}_a. \tag{F11}$$

We use this method in numerical calculations.

APPENDIX G: INDUCED CURRENT

In this Appendix, we derive the induced current J_d^μ in Eq. (22). Let us consider the Dirac Hamiltonian coupled to $(d + 1)$ slowly varying background scalar fields $m_{a,\boldsymbol{r}}$,

$$\mathcal{H}(\boldsymbol{r}) = -i \sum_{i=1}^{d} \partial_i \Gamma_i + \sum_{a=1}^{d+1} m_{a,\boldsymbol{r}} M_a, \tag{G1}$$

where Γ denotes gamma matrix and $M_a = \Gamma_{a+d}$. Gamma matrices satisfy $\{\Gamma_i, \Gamma_j\} = 2\delta_{ij}$ and are chosen to be $\Gamma_1\Gamma_2\ldots\Gamma_{2d+1} = \chi_d \mathbb{1}_{2^d}$ where $\chi_d = i^d$. Thus, $\text{Tr}[\Gamma_{i_1}\Gamma_{i_2}\ldots\Gamma_{i_{2d+1}}] = \epsilon_{i_1 i_2 \ldots i_{2d+1}}\text{Tr}[\chi_d \mathbb{1}_{2^d}] = \epsilon_{i_1 i_2 \ldots i_{2d+1}}\chi_d 2^d$ where $\epsilon_{12\ldots 2d+1} = 1$. The Lagrangian is given by $\mathcal{L} = i\Psi^\dagger \partial_t \Psi - \bar{\Psi}\mathcal{H}\Psi$ where Ψ denotes the Dirac spinor

and $\bar{\Psi} = \Psi^\dagger \gamma^0$:

$$\mathcal{L} = \bar{\Psi}\left[i\slashed{\partial} - \sum_{a=1}^{d} m_{a,\mathbf{r}}\gamma^{a+d} - m_{d+1,\mathbf{r}}\mathbb{1}_{2^d} \right], \tag{G2}$$

where we use the Feynman slash notation $\slashed{A} = \sum_{\mu=0}^{d} A_\mu \gamma^\mu$, and define new gamma matrices $\gamma^0 = \Gamma_{2d+1}$ and $\gamma^{i\neq0} = \gamma^0 \Gamma_i$. γ^μ satisfies $\{\gamma^\mu, \gamma^\nu\} = -2\eta^{\mu\nu}$ where $\eta_{\mu\nu} = \text{diag}(-1, 1, \ldots, 1)$ for $\mu, \nu = 0, 1, \ldots, 2d$, and $\text{Tr}[\gamma^{\mu_1}\gamma^{\mu_2}\ldots\gamma^{\mu_{2d+1}}] = \epsilon^{\mu_1\mu_2\ldots\mu_{2d+1}}\chi_d(-1)^d 2^d$, where $\epsilon^{012\ldots2d} = 1$.

We calculate the current density $\langle j_d^\mu(x)\rangle$ by using

$$\left\langle j_d^\mu(x) \right\rangle = \langle \bar{\Psi}(x)\gamma^\mu\Psi(x)\rangle = -\lim_{y\to x}\text{Tr}[\langle T\Psi(x)\bar{\Psi}(y)\rangle\gamma^\mu] = \lim_{y\to x}\text{Tr}[iG(x,y)\gamma^\mu], \tag{G3}$$

where $G(x,y) = i\langle T\Psi(x)\bar{\Psi}(y)\rangle$ is the propagator. Here, we denote $x^\mu = (x^0, \mathbf{x})$ as x for simplicity. The propagator $G(x,y)$ satisfies

$$\left[-i\slashed{\partial}_x + \sum_{a=1}^{d} m_{a,\mathbf{x}}\gamma^{a+d} + m_{d+1,\mathbf{x}} \right]G(x,y) = \delta^{(d+1)}(x-y). \tag{G4}$$

Regarding $G(x,y)$ as a function of x and $(x-y)$, we Fourier transform the propagator by [93]

$$G(x,y) = \int \frac{d^{d+1}p}{(2\pi)^{d+1}} e^{ip\cdot(x-y)}\tilde{G}(x,p). \tag{G5}$$

Note that translation symmetry is broken by $m_{a,\mathbf{r}}$, so $G(x,y)$ can not be a function of $(x-y)$ only. Then, we expand $\tilde{G}(x,p)$ by its spatial derivative terms:

$$\tilde{G}(x,p) = \frac{1}{\slashed{p} + \sum_{a=1}^{d} m_{a,\mathbf{x}}\gamma^{a+d} + m_{d+1,\mathbf{x}} - i\slashed{\partial}_x}$$
$$= \tilde{G}_0(x,p) + \tilde{G}_0(x,p)i\slashed{\partial}_x\tilde{G}_0(x,p) + \tilde{G}_0(x,p)i\slashed{\partial}_x\tilde{G}_0(x,p)i\slashed{\partial}_x\tilde{G}_0(x,p) + \cdots = \tilde{G}_0(x,p)\sum_{k=0}^{\infty}[i\slashed{\partial}\,\tilde{G}_0(x,p)]^k. \tag{G6}$$

Here, we define $\tilde{G}_0(x,p)$:

$$\tilde{G}_0(x,p) = \frac{1}{\slashed{p} + \sum_{a=1}^{d} m_{a,\mathbf{x}}\gamma^{a+d} + m_{d+1,\mathbf{x}}} = \frac{1}{p^2 + m_\mathbf{x}^2}\left(m_{d+1,\mathbf{x}} - \slashed{p} - \sum_{a=1}^{d} m_{a,\mathbf{x}}\gamma^{a+d} \right) = \frac{1}{p^2 + m_\mathbf{x}^2}(M_\mathbf{x} - \slashed{p}), \tag{G7}$$

where $m_\mathbf{x}^2 = \sum_{a=1}^{d+1} m_{a,\mathbf{x}}^2$ and $M_\mathbf{x} = m_{d+1,\mathbf{x}} - \sum_{a=1}^{d} m_{a,\mathbf{x}}\gamma^{a+d}$. The lowest-order contribution comes from $k = d$ term in Eq. (G6). Up to the lowest order in the derivative, we have

$$\left\langle j_d^\mu(x) \right\rangle = i^{d+1}\int \frac{d^{d+1}p}{(2\pi)^{d+1}} \frac{1}{\left(p^2 + m_\mathbf{x}^2\right)^{d+1}} \text{Tr}[(M_\mathbf{x} - \slashed{p})\slashed{\partial}M_\mathbf{x}\slashed{\partial}M_\mathbf{x}\ldots\slashed{\partial}M_\mathbf{x}\gamma^\mu]$$
$$= i^{d+1}\int \frac{d^{d+1}p}{(2\pi)^{d+1}} \frac{1}{\left(p^2 + m_\mathbf{x}^2\right)^{d+1}} \text{Tr}[M_\mathbf{x}\slashed{\partial}M_\mathbf{x}\slashed{\partial}M_\mathbf{x}\ldots\slashed{\partial}M_\mathbf{x}\gamma^\mu]. \tag{G8}$$

From

$$\text{Tr}\left[M_\mathbf{x}\gamma^{\mu_1}\partial_{\mu_1}M_\mathbf{x}\gamma^{\mu_2}\partial_{\mu_2}M_\mathbf{x}\ldots\gamma^{\mu_d}\partial_{\mu_d}M_\mathbf{x}\gamma^\mu \right] = (-1)^{d(d+1)/2}2^d\chi_d\,\epsilon^{a_1a_2\ldots a_{d+1}}\epsilon^{\mu\mu_1\ldots\mu_d}m_{a_1,\mathbf{x}}\partial_{\mu_1}m_{a_2,\mathbf{x}}\ldots\partial_{\mu_d}m_{a_{d+1},\mathbf{x}}, \tag{G9}$$

we obtain

$$\left\langle j_d^\mu(x) \right\rangle = i^{d+1}(-1)^{d(d+1)/2}2^d\chi_d\int \frac{d^{d+1}p}{(2\pi)^{d+1}} \frac{1}{\left(p^2 + m_\mathbf{x}^2\right)^{d+1}} \epsilon^{a_1a_2\ldots a_{d+1}}\epsilon^{\mu\mu_1\ldots\mu_d}m_{a_1,\mathbf{x}}\partial_{\mu_1}m_{a_2,\mathbf{x}}\ldots\partial_{\mu_d}m_{a_{d+1},\mathbf{x}}$$
$$= -i^d(-1)^{d(d+1)/2}\frac{\chi_d}{d!\,\text{Area}(S^d)}\epsilon^{a_1a_2\ldots a_{d+1}}\epsilon^{\mu\mu_1\ldots\mu_d}\hat{m}_{a_1,\mathbf{x}}\partial_{\mu_1}\hat{m}_{a_2,\mathbf{x}}\ldots\partial_{\mu_d}\hat{m}_{a_{d+1},\mathbf{x}}$$
$$= -(-1)^{d(d-1)/2}\frac{1}{d!\,\text{Area}(S^d)}\epsilon^{a_1a_2\ldots a_{d+1}}\epsilon^{\mu\mu_1\ldots\mu_d}\hat{m}_{a_1,\mathbf{x}}\partial_{\mu_1}\hat{m}_{a_2,\mathbf{x}}\ldots\partial_{\mu_d}\hat{m}_{a_{d+1},\mathbf{x}}, \tag{G10}$$

where $\hat{m}_{a,\mathbf{x}} = \frac{m_{a,\mathbf{x}}}{m_\mathbf{x}}$ and $\mathrm{Area}(S^d) = \frac{2\pi^{(d+1)/2}}{\Gamma(\frac{d+1}{2})}$. Hence, the induced current $\langle j_d^\mu(x) \rangle$ in d dimensions (denoted as J_d^μ in the main text) is given by the winding number density of mass terms $m_{a,\mathbf{r}}$ where $a = 1, \ldots, d$.

The induced current density can be calculated either using the bulk Hamiltonian or the boundary Hamiltonian. There is a caveat because the convention for the gamma matrices may change by the projection, which can lead a different choice of χ_d on the boundary while we take $\chi_d = i^d$ in the bulk. Therefore, we need to carefully calculate $\tilde{\chi}_{d-1} \equiv 2^{-(d-1)}\mathrm{Tr}[\tilde{\Gamma}_1 \ldots \tilde{\Gamma}_{d-1}\tilde{M}_1 \ldots \tilde{M}_d]$ on the boundary, where $\tilde{\Gamma}$ and $\tilde{M}$ are gamma matrices and mass matrices projected to boundary defined in Appendix F. It turns out that $\tilde{\chi}_{d-1} = -\chi_{d-1}$ as we show now.

Now, let us turn to the boundary theory when a domain between trivial and topological phases is formed. The boundary Hamiltonian $h(\mathbf{k}_S, \mathbf{r})$ is

$$h(\mathbf{k}_S, \mathbf{r}) = P_+(\mathbf{r})\left[\mathbf{k}_S \cdot \mathbf{\Gamma} + \sum_{a=1}^d m_{a,\mathbf{r}}M_a\right]P_+(\mathbf{r}), \qquad \text{(G11)}$$

which is obtained by the projection to the boundary, introduced in Appendix F. Since $h(\mathbf{k}_S, \mathbf{r})$ has $(d-1)$ kinetic terms and d mass terms, the induced current $\langle j_{d-1}^\mu(x) \rangle$ on the $(d-1)$D boundary is given by repeating the above calculation. The minus sign can be traced in the following way. From the definition of $\tilde{\Gamma}_{L=1,\ldots,d-1} = (\mathbf{e}_{\mathbf{r},L} \cdot \mathbf{\Gamma})P_+(\mathbf{r})$ and $\tilde{M}_{a=1,\ldots,d} = M_a P_+(\mathbf{r})$, where $\mathbf{e}_{\mathbf{r},L}$ are orthonormal bases at $\mathbf{r}$, we show $\mathrm{Tr}[\tilde{\Gamma}_1 \ldots \tilde{\Gamma}_{d-1}\tilde{M}_1 \ldots \tilde{M}_d] = -2^{d-1}\chi_{d-1}$ explicitly:

$$
\begin{aligned}
\mathrm{Tr}[\tilde{\Gamma}_1 \ldots \tilde{\Gamma}_{d-1}\tilde{M}_1 \ldots \tilde{M}_d] &= (\mathbf{e}_{\mathbf{r},1})_{\mu_1} \ldots (\mathbf{e}_{\mathbf{r},d-1})_{\mu_{d-1}}\mathrm{Tr}\big[\Gamma_{\mu_1}P_+(\mathbf{r}) \ldots \Gamma_{\mu_{d-1}}P_+(\mathbf{r})M_1 P_+(\mathbf{r}) \ldots M_d P_+(\mathbf{r})\big] \\
&= (\mathbf{e}_{\mathbf{r},1})_{\mu_1} \ldots (\mathbf{e}_{\mathbf{r},d-1})_{\mu_{d-1}}\mathrm{Tr}\big[\Gamma_{\mu_1} \ldots \Gamma_{\mu_{d-1}}M_1 \ldots M_d P_+(\mathbf{r})\big] \\
&= -\frac{i}{2}(\mathbf{e}_{\mathbf{r},1})_{\mu_1} \ldots (\mathbf{e}_{\mathbf{r},d-1})_{\mu_{d-1}}\mathrm{Tr}\big[\Gamma_{\mu_1} \ldots \Gamma_{\mu_{d-1}}M_1 \ldots M_d(\mathbf{e}_{\mathbf{r},0} \cdot \mathbf{\Gamma})M_{d+1}\big] \\
&= \frac{i}{2}(\mathbf{e}_{\mathbf{r},0})_{\mu_0} \ldots (\mathbf{e}_{\mathbf{r},d-1})_{\mu_{d-1}}\mathrm{Tr}[\Gamma_1 \ldots \Gamma_d M_1 \ldots M_{d+1}] = \frac{i}{2}\epsilon_{01\ldots d-1}\mathrm{Det}\,(\mathbf{e}_\mathbf{r})\,2^d\chi_d = -2^{d-1}\chi_{d-1},
\end{aligned}
$$
$$\text{(G12)}$$

where we define $\mathbf{e}_{\mathbf{r},0} \equiv \mathbf{n}_\mathbf{r}$ in the third line, $\mathrm{Det}(\mathbf{e}_\mathbf{r})$ is the determinant of $\mathbf{e}_\mathbf{r}$ in the matrix notation.

Finally, let us mention that dD $(d+1)$th-order phase is allowed for classes A, AI, AII, BDI, and D. However, when the chiral or particle-hole symmetry exists, the induced current is zero. Thus, charge accumulation on boundary occurs only for classes A, AI, and AII.

APPENDIX H: REVIEW OF THE WILSON LOOP

In this Appendix, we review the Wilson loop and its symmetry transformation. We closely follow Ref. [67]. In addition, we introduce a more general method which exploits parallel transport and symmetry transformation of Berry connection.

1. Tight-binding notation

In the tight-binding model, Hamiltonian is spanned by a basis set $|\mathbf{R}\,\alpha\rangle$. We denote $\mathbf{R}$ and $\mathbf{x}_\alpha$ as the unit-cell position and the sublattice position of the orbital α:

$$
\begin{aligned}
\hat{H} &= \sum_{\mathbf{R},\mathbf{R}'}\sum_{\alpha,\beta}|\mathbf{R}\,\alpha\rangle H(\mathbf{R} - \mathbf{R}')_{\alpha\beta}\langle\mathbf{R}'\,\beta| \\
&= \sum_\mathbf{k}\sum_{\alpha,\beta}|\mathbf{k}\,\alpha\rangle H(\mathbf{k})_{\alpha\beta}\langle\mathbf{k}\,\beta|. \qquad \text{(H1)}
\end{aligned}
$$

Here, $|\mathbf{k}\,\alpha\rangle$ is the Fourier transformation of $|\mathbf{R}\,\alpha\rangle$,

$$|\mathbf{k}\,\alpha\rangle \equiv \frac{1}{\sqrt{N_{\mathrm{cell}}}}\sum_\mathbf{R} e^{i\mathbf{k}\cdot(\mathbf{R}+\mathbf{x}_\alpha)}|\mathbf{R}\,\alpha\rangle, \qquad \text{(H2)}$$

where N_{cell} is the number of unit cells in the system. These basis states are orthonormal: $\langle\mathbf{R}\,\alpha|\mathbf{R}'\,\beta\rangle = \delta_{\mathbf{R},\mathbf{R}'}\delta_{\alpha\beta}$ and $\langle\mathbf{k}\,\alpha|\mathbf{k}'\,\beta\rangle = \delta_{\mathbf{k},\mathbf{k}'}\delta_{\alpha\beta}$.

When the orbitals are located at $\mathbf{x}_\alpha \neq 0$, $|\mathbf{k}\,\alpha\rangle$ is not periodic in the Brillouin zone

$$|\mathbf{k} + \mathbf{G}\,\alpha\rangle = e^{i\mathbf{G}\cdot\mathbf{x}_\alpha}|\mathbf{k}\,\alpha\rangle = |\mathbf{k}\,\beta\rangle V(\mathbf{G})_{\beta\alpha}^{-1}, \qquad \text{(H3)}$$

where $V(\mathbf{k})_{\alpha\beta} = e^{-i\mathbf{k}\cdot\mathbf{x}_\alpha}\delta_{\alpha\beta}$ (note that we take a convention different from the one in Ref. [67]). Diagonalizing $H(\mathbf{k})_{\alpha\beta}$, we obtain energy eigenstates $|n, \mathbf{k}\rangle_\alpha$, where

$$H(\mathbf{k})_{\alpha\beta}|n, \mathbf{k}\rangle_\beta = E_n(\mathbf{k})|n, \mathbf{k}\rangle_\alpha. \qquad \text{(H4)}$$

The energy eigenstates $|n, \mathbf{k}\rangle$ satisfy

$$\langle n, \mathbf{k}|m, \mathbf{k}\rangle = \delta_{nm}, \quad \sum_{n=1}^{n_{\mathrm{tot}}}|n, \mathbf{k}\rangle_\alpha\langle n, \mathbf{k}|_\beta = \delta_{\alpha\beta}, \qquad \text{(H5)}$$

where n_{tot} is the rank of Hamiltonian $H(\mathbf{k})_{\alpha\beta}$, which is also the number of orbitals: $\sum_\alpha 1 = n_{\mathrm{tot}}$. Since $H(\mathbf{k} + \mathbf{G}) = V(\mathbf{G})H(\mathbf{k})V(\mathbf{G})^{-1}$, the "periodic gauge" is defined by

$$|n, \mathbf{k} + \mathbf{G}\rangle = V(\mathbf{G})|n, \mathbf{k}\rangle. \qquad \text{(H6)}$$

2. Symmetry transformation

Consider a symmetry operation $\hat{\sigma}\colon \mathbf{r} \to D_\sigma\mathbf{r} + \mathbf{d}$. D_σ is representation of the point-group part of $\hat{\sigma}$, which is an element of orthogonal group $O(d)$. It acts on the basis $|\mathbf{R}\,\alpha\rangle$ as follows:

$$\hat{\sigma}|\mathbf{R}\,\alpha\rangle = |\tilde{\mathbf{R}}\,\tilde{\alpha}\rangle U(\sigma)_{\tilde{\alpha}\alpha}, \qquad \text{(H7)}$$

where $\tilde{\mathbf{R}} = D_\sigma(\mathbf{R} + \mathbf{x}_\alpha) + \mathbf{d} - \mathbf{x}_{\tilde{\alpha}}$. Since $U(\sigma)$ acts on sublattice degrees of freedom, $U(\sigma)$ is bijective and independent of $\mathbf{R}$. Using the fact that $\mathbf{k} \cdot \mathbf{x} = D_\sigma\mathbf{k} \cdot D_\sigma\mathbf{x}$ which follows from $D_\sigma \in O(d)$, we obtain the symmetry transformation of $|\mathbf{k}, \alpha\rangle$

under $\hat{\sigma}$:

$$\hat{\sigma}\,|\boldsymbol{k}\,\alpha\rangle = \frac{1}{\sqrt{N_{\text{cell}}}}\sum_{\boldsymbol{R}} e^{i\boldsymbol{k}\cdot(\boldsymbol{R}+\boldsymbol{x}_\alpha)}\,\hat{\sigma}\,|\boldsymbol{R}\,\alpha\rangle$$

$$= \frac{1}{\sqrt{N_{\text{cell}}}}\sum_{\boldsymbol{R}} e^{iD_\sigma \boldsymbol{k}\cdot D_\sigma(\boldsymbol{R}+\boldsymbol{x}_\alpha)}\,|\tilde{\boldsymbol{R}}\,\beta\rangle\,U(\sigma)_{\beta\alpha}$$

$$= e^{-iD_\sigma \boldsymbol{k}\cdot\boldsymbol{d}}\frac{1}{\sqrt{N_{\text{cell}}}}\sum_{\tilde{\boldsymbol{R}}} e^{iD_\sigma \boldsymbol{k}\cdot(\tilde{\boldsymbol{R}}+\boldsymbol{x}_\beta)}\,|\tilde{\boldsymbol{R}}\,\beta\rangle\,U(\sigma)_{\beta\alpha}$$

$$= e^{-iD_\sigma \boldsymbol{k}\cdot\boldsymbol{d}}\,|D_\sigma \boldsymbol{k}\,\beta\rangle\,U(\sigma)_{\beta\alpha}$$

$$\equiv |D_\sigma \boldsymbol{k}\,\beta\rangle\,U_\sigma(\boldsymbol{k})_{\beta\alpha}, \tag{H8}$$

where we define $U_\sigma(\boldsymbol{k}) = e^{-iD_\sigma \boldsymbol{k}\cdot\boldsymbol{d}}\,U(\sigma)$. From the condition that $\hat{H}$ is symmetric under $\hat{\sigma}$, $\hat{H} = \hat{\sigma}\hat{H}\hat{\sigma}^{-1}$, we obtain

$$H(D_\sigma \boldsymbol{k}) = U_\sigma(\boldsymbol{k})\,H(\boldsymbol{k})\,U_\sigma(\boldsymbol{k})^{-1}. \tag{H9}$$

At high-symmetry momenta $\boldsymbol{k}_\sigma^{\text{inv}} = D_\sigma \boldsymbol{k}_\sigma^{\text{inv}} + \boldsymbol{G}(\boldsymbol{k}_\sigma^{\text{inv}})$, $H(\boldsymbol{k}_\sigma^{\text{inv}})$ and $V(\boldsymbol{G}(\boldsymbol{k}_\sigma^{\text{inv}}))\,U(\boldsymbol{k}_\sigma^{\text{inv}})$ commute,

$$\left[H(\boldsymbol{k}_\sigma^{\text{inv}}), V\left(\boldsymbol{G}(\boldsymbol{k}_\sigma^{\text{inv}})\right) U(\boldsymbol{k}_\sigma^{\text{inv}})\right] = 0. \tag{H10}$$

For inversion symmetry, the inversion-invariant momenta are given by $\boldsymbol{k}^{\text{inv}} = -\boldsymbol{k}^{\text{inv}}$ (mod $\boldsymbol{G}$).

From Eq. (H9), we can find an energy eigenstate at $D_\sigma \boldsymbol{k}$, $|n, D_\sigma \boldsymbol{k}\rangle$, as a symmetry partner of $|n, \boldsymbol{k}\rangle$ up to unitary transformation B_σ, the sewing matrix:

$$|n, D_\sigma \boldsymbol{k}\rangle = U_\sigma(\boldsymbol{k})\,|m, \boldsymbol{k}\rangle\,B_\sigma(\boldsymbol{k})_{mn}. \tag{H11}$$

B_σ appears here because a symmetry transformation can lead to a linear combination of energy eigenstates when they are degenerate. It is straightforward to show that the sewing matrix $B_\sigma(\boldsymbol{k})$,

$$B_\sigma(\boldsymbol{k})_{nm} = \langle n, \boldsymbol{k}|U_\sigma(\boldsymbol{k})^\dagger|m, D_\sigma \boldsymbol{k}\rangle, \tag{H12}$$

is a unitary matrix, $B_\sigma(\boldsymbol{k}) \in U(n_{\text{occ}})$, and is periodic in the Brillouin zone:

$$\sum_{p=1}^{n_{\text{occ}}} B_\sigma(\boldsymbol{k})_{np}[B_\sigma(\boldsymbol{k})^\dagger]_{pm} = \delta_{nm}, \tag{H13}$$

$$B_\sigma(\boldsymbol{k}+\boldsymbol{G}) = B_\sigma(\boldsymbol{k}). \tag{H14}$$

Now, we investigate the transformation of the non-Abelian Berry connection $[a_i(\boldsymbol{k})]_{nm}$ defined by the occupied states $|n, \boldsymbol{k}\rangle$:

$$[a_i(\boldsymbol{k})]_{nm} = \langle n, \boldsymbol{k}|\,i\nabla_i\,|m, \boldsymbol{k}\rangle, \tag{H15}$$

where ∇_i denotes $\frac{\partial}{\partial k_i}$. Note that $a_i(\boldsymbol{k})$ is Hermitian:

$$[a_i(\boldsymbol{k})]_{nm} = [a_i(\boldsymbol{k})]_{mn}^*. \tag{H16}$$

The Berry connection transforms under the gauge transformation $|n, \boldsymbol{k}\rangle \rightarrow |n, \boldsymbol{k}\rangle_G = |m, \boldsymbol{k}\rangle\,G(\boldsymbol{k})_{mn}$ of the occupied states as

$$a_i^G(\boldsymbol{k}) = G^\dagger(\boldsymbol{k})\,a_i(\boldsymbol{k})\,G(\boldsymbol{k}) + iG^\dagger(\boldsymbol{k})\,\nabla_i G(\boldsymbol{k}). \tag{H17}$$

From Eqs. (H11) and (H15), we obtain the symmetry transformation of $a_i(\boldsymbol{k})$ under $\hat{\sigma}$,

$$\left[D_\sigma^{-1}\right]_{ij}\left[a_j(D_\sigma \boldsymbol{k}) - \boldsymbol{d}_j\mathbb{1}\right]$$

$$= [B_\sigma(\boldsymbol{k})]^\dagger\,a_i(\boldsymbol{k})\,B_\sigma(\boldsymbol{k}) + i[B_\sigma(\boldsymbol{k})]^\dagger\,\nabla_i B_\sigma(\boldsymbol{k}), \tag{H18}$$

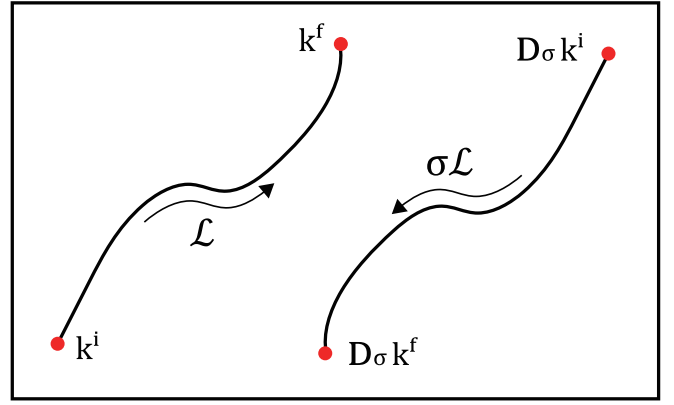

FIG. 15. Paths $\mathcal{L}$ and $\sigma\mathcal{L}$ in which the Wilson lines $W_\mathcal{L}$ and $W_{\sigma\mathcal{L}}$ are defined, respectively. $\boldsymbol{k}^i$ ($\boldsymbol{k}^f$) is the start (end) point of $\mathcal{L}$. $\sigma\mathcal{L}$ is given by the symmetry transformation of $\mathcal{L}$ under $\hat{\sigma}$.

where $\mathbb{1}$ denotes an identity matrix in the occupied subspace. The results (H17) and (H18) are used to derive the symmetry transformations of the Wilson loop.

3. Wilson line

Let us consider a line $\mathcal{L} : \boldsymbol{k}^i \rightarrow \boldsymbol{k}^f$ which is parametrized by λ. Start and end points $\boldsymbol{k}^{i,f}$ are given by $\boldsymbol{k}^i = \boldsymbol{k}(\lambda = 0)$ and $\boldsymbol{k}^f = \boldsymbol{k}(\lambda = 1)$ as shown in Fig. 15. Then, the Wilson line $[W_\mathcal{L}]_{nm}$ is defined by the path-ordered exponential of the Berry connection $[a_i(\boldsymbol{k})]_{nm}$ along the line $\mathcal{L}$:

$$[W_\mathcal{L}]_{nm} = \left[P\,e^{i\int_\mathcal{L} dk^i a_i(\boldsymbol{k})}\right]_{nm}. \tag{H19}$$

For convenience, we choose a smooth gauge along $\mathcal{L}$. Along the line $\mathcal{L}$, the covariant derivative D_λ is defined as

$$D_\lambda = \frac{d}{d\lambda} - i\frac{dk_i(\lambda)}{d\lambda}\,a_i(\boldsymbol{k}(\lambda))$$

$$= \frac{d}{d\lambda} - i\dot{k}_i(\lambda)\,a_i(\boldsymbol{k}(\lambda))$$

$$= \dot{k}_i(\lambda)\left[\nabla_i - ia_i(\boldsymbol{k}(\lambda))\right]. \tag{H20}$$

The Wilson line $W_{\mathcal{L}_\lambda}$ is the solution of

$$D_\lambda W_{\mathcal{L}_\lambda} = 0, \tag{H21}$$

with the boundary conditions $W_{\mathcal{L}_{\lambda=0}} = \mathbb{1}$ and $W_{\mathcal{L}_{\lambda=1}} = W_\mathcal{L}$. Here, $\mathcal{L}_\lambda : \boldsymbol{k}^i \rightarrow \boldsymbol{k}(\lambda)$ and $\mathcal{L}_{\lambda=1} = \mathcal{L}$. With the help of Eqs. (H20) and (H21), various properties of the Wilson line are derived.

First, $W_\mathcal{L}$ is unitary: $W_\mathcal{L}^\dagger = W_\mathcal{L}^{-1}$. Also note that $W_\mathcal{L}^\dagger = W_{\mathcal{L}_R}$ where $W_{\mathcal{L}_R}$ is the "reversed" Wilson loop which is defined along the path-reversed line $\mathcal{L}_R : \boldsymbol{k}^f \rightarrow \boldsymbol{k}^i$.

Second, the gauge transformation of the Wilson line $W_{\mathcal{L}_\lambda}^G$ is derived from Eq. (H17). From Eq. (H21) for $W_{\mathcal{L}_\lambda}^G$,

$$\frac{d}{d\lambda}W_{\mathcal{L}_\lambda}^G = i\dot{k}_i(\lambda)\,a_i^G(\boldsymbol{k}(\lambda))\,W_{\mathcal{L}_\lambda}^G$$

$$= i\dot{k}_i(\lambda)\left[G^\dagger(\boldsymbol{k}(\lambda))\,a_i(\boldsymbol{k}(\lambda))\,G(\boldsymbol{k}(\lambda))\right.$$

$$\left. + iG^\dagger(\boldsymbol{k}(\lambda))\,\nabla_i G(\boldsymbol{k}(\lambda))\right]W_{\mathcal{L}_\lambda}^G. \tag{H22}$$

Hence,

$$\frac{d}{d\lambda}\left[G(\boldsymbol{k}_\lambda)\,W_{\mathcal{L}_\lambda}^G\right] = i\dot{k}_\lambda^\mu\, a_\mu(\boldsymbol{k}_\lambda)\left[G(\boldsymbol{k}_\lambda)\,W_{\mathcal{L}_\lambda}^G\right]. \tag{H23}$$

The solution of the above equation is given by

$$W_{\mathcal{L}_\lambda}^G = G^\dagger(\boldsymbol{k}(\lambda))\,W_{\mathcal{L}_\lambda}\,G(\boldsymbol{k}_1), \tag{H24}$$

with the boundary condition $W_{\mathcal{L}_{\lambda=0}} = \mathbb{1}$.

Finally, we obtain the Wilson line $W_{\sigma\mathcal{L}_\lambda}$, which is the symmetry transformation of $W_{\mathcal{L}_\lambda}$ under $\hat{\sigma}$, where $\sigma\mathcal{L}_\lambda : D_\sigma\boldsymbol{k}^i \rightarrow D_\sigma\boldsymbol{k}^f$ as shown in Fig. 15. From Eqs. (H18) and (H21), we derive

$$W_{\sigma\mathcal{L}_\lambda} = e^{i\int_{\mathcal{L}_\lambda} dk_i\,[D_\sigma^{-1}\boldsymbol{d}]_i}\,[B_\sigma(\boldsymbol{k}(\lambda))]^\dagger\,W_{\mathcal{L}_\lambda}\,B_\sigma(\boldsymbol{k}_1), \tag{H25}$$

in a similar manner to the one used for deriving the gauge transformation. For completeness, we derive the Wilson line $W_{\Theta\mathcal{L}}$, which is the symmetry transformation of the Wilson line $W_{\mathcal{L}_\lambda}$ under antiunitary symmetry $\hat{\Theta} = \hat{\sigma}\mathcal{K}$, where $\mathcal{K}$ denotes the complex-conjugation operator. $\hat{\Theta}$ acts on $\boldsymbol{r}$ and $\boldsymbol{k}$ as $\hat{\Theta} : \boldsymbol{r} \rightarrow D_\sigma\boldsymbol{r} + \boldsymbol{d}$ and $\boldsymbol{k} \rightarrow -D_\sigma\boldsymbol{k}$. Thus, $\Theta\mathcal{L} : -D_\sigma\boldsymbol{k}^i \rightarrow -D_\sigma\boldsymbol{k}^f$ is a line with a start point $-D_\sigma\boldsymbol{k}^i$ and an end point $-D_\sigma\boldsymbol{k}^f$. The Wilson line $W_{\Theta\mathcal{L}}$ is given by

$$W_{\Theta\mathcal{L}_\lambda} = e^{-i\int_{\mathcal{L}_\lambda} dk_i\,[D_\sigma^{-1}\boldsymbol{d}]_i}\,[B_\Theta(\boldsymbol{k}(\lambda))]^\dagger\,W_{\mathcal{L}_\lambda}^*\,B_\Theta(\boldsymbol{k}_1), \tag{H26}$$

where $B_\Theta(\boldsymbol{k})$ is sewing matrix for $\hat{\Theta}$:

$$[B_\Theta(\boldsymbol{k})]_{nm}^\dagger = \langle n, -D_\sigma\boldsymbol{k}|\Theta(\boldsymbol{k})|m, \boldsymbol{k}\rangle\,\mathcal{K}, \tag{H27}$$

and $\hat{\Theta}|\boldsymbol{k}\,\alpha\rangle = |-D_\sigma\boldsymbol{k}\,\beta\rangle\,\Theta(\boldsymbol{k})_{\beta\alpha}$.

4. Wilson Loop

From Eq. (H24), we conclude that the spectrum of $W_{\mathcal{L}}$ is gauge invariant when $\boldsymbol{k}^i = \boldsymbol{k}^f$ (mod $\boldsymbol{G}$). In the Brillouin zone, consider a noncontractible loop $\mathcal{L} : \boldsymbol{k}_0 \rightarrow \boldsymbol{k}_0 + \boldsymbol{G}$. For numerical calculations, we implement the discretized form

$$\left[W_{\boldsymbol{k}_0+\boldsymbol{G}\leftarrow\boldsymbol{k}_0}\right]_{nm} = \lim_{N\rightarrow\infty}\langle n, \boldsymbol{k}_0 + \boldsymbol{G}|\left[\prod_{i=1}^{N-1} P(\boldsymbol{k}_i)\right]|m, \boldsymbol{k}_0\rangle, \tag{H28}$$

where $\boldsymbol{k}_i = \boldsymbol{k}_0 + \frac{i}{N}\boldsymbol{G}$ and $P(\boldsymbol{k}) = \sum_{n=1}^{n_{\text{occ}}} |n, \boldsymbol{k}\rangle\langle n, \boldsymbol{k}|$ is the projector for the occupied states. However, we stick to formulate the Wilson loop in the continuum form

$$[W_{\mathcal{L}}]_{nm} = \left[P\,e^{i\int_{\mathcal{L}} dk^i a_i(\boldsymbol{k})}\right]_{nm} \tag{H29}$$

to exploit the covariant derivative D_λ and symmetry transformation of the Berry connection $a(\boldsymbol{k})$. The eigenstates $|\theta(\boldsymbol{k}_0)\rangle$ of the Wilson loop $W_{\boldsymbol{k}_0+\boldsymbol{G}\leftarrow\boldsymbol{k}_0}$ are given by $W_{\boldsymbol{k}_0+\boldsymbol{G}\leftarrow\boldsymbol{k}_0}|\theta(\boldsymbol{k}_0)\rangle = e^{i\theta(\boldsymbol{k}_0)}|\theta(\boldsymbol{k}_0)\rangle$. Because of the periodic gauge, the Wilson loop is periodic

$$W_{\boldsymbol{k}_0+\boldsymbol{G}+\boldsymbol{G}'\leftarrow\boldsymbol{k}_0+\boldsymbol{G}'} = W_{\boldsymbol{k}_0+\boldsymbol{G}\leftarrow\boldsymbol{k}_0} \tag{H30}$$

for any reciprocal vector $\boldsymbol{G}'$. Also, the Wilson loop spectrum $\{\theta(\boldsymbol{k}_0)\}$ is independent of the start point $\boldsymbol{k}_0$,

$$\begin{aligned}W_{\boldsymbol{k}_0'+\boldsymbol{G}\leftarrow\boldsymbol{k}_0'} &= W_{\boldsymbol{k}_0'+\boldsymbol{G}\leftarrow\boldsymbol{k}_0+\boldsymbol{G}}W_{\boldsymbol{k}_0+\boldsymbol{G}\leftarrow\boldsymbol{k}_0}W_{\boldsymbol{k}_0'\leftarrow\boldsymbol{k}_0}^\dagger \\ &= W_{\boldsymbol{k}_0'\leftarrow\boldsymbol{k}_0}W_{\boldsymbol{k}_0+\boldsymbol{G}\leftarrow\boldsymbol{k}_0}W_{\boldsymbol{k}_0'\leftarrow\boldsymbol{k}_0}^\dagger,\end{aligned} \tag{H31}$$

where $\boldsymbol{k}_0, \boldsymbol{k}_0' \in \mathcal{L} : \boldsymbol{k}_0 \rightarrow \boldsymbol{k}_0 + \boldsymbol{G}$.
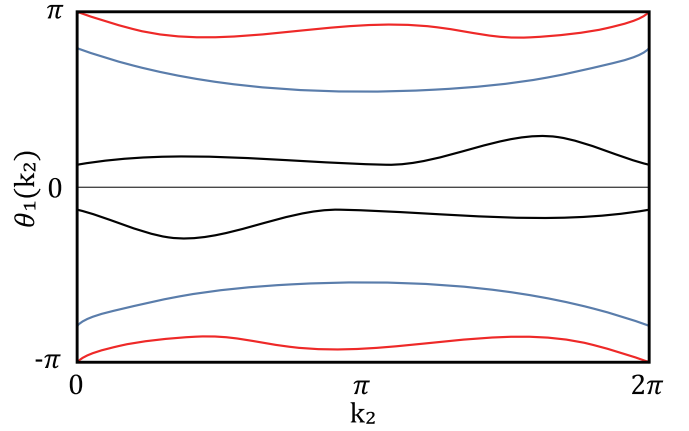

FIG. 16. Inversion-symmetric Wilson loop spectrum. The spectrum is particle-hole symmetric, i.e., $\{\theta_1(-\boldsymbol{k}_0^{(1)})\} = \{-\theta_1(\boldsymbol{k}_0^{(1)})\}$. Hence, the projector $\tilde{P}^{(1)}$ for the nested Wilson loop must include pairs of particle-hole symmetric Wilson bands marked by the same colors.

Now, let us discuss a consequence of symmetry $\hat{\sigma}$ on the Wilson loop. Although Eqs. (H25) and (H26) apply to arbitrary symmetries and lines, we restrict our attention to inversion I and k_1-directed loop $\mathcal{L}_1$ in three dimensions $\mathcal{L}_1 : (k_{1,0}, k_2, k_3) \rightarrow (k_{1,0} + 2\pi, k_2, k_3)$ for the discussion relevant to this paper. Since inversion symmetry is symmorphic, one can find a coordinate system with $\boldsymbol{d} = 0$. Applying Eq. (H25),

$$W_{I\mathcal{L}_1} = \left[B_I(\boldsymbol{k}_0^{(1)})\right]^\dagger\,W_{\mathcal{L}_1}\,B_I(\boldsymbol{k}_0^{(1)}), \tag{H32}$$

where $\boldsymbol{k}_0^{(1)} = (k_{1,0}, k_2, k_3)$. With help of Eqs. (H30) and (H31), $W_{I\mathcal{L}_1}$ satisfies $W_{I\mathcal{L}_1} = W_{\mathcal{L}_1}^{-1}$ and its spectrum is $\{-\theta_1^a(-\boldsymbol{k}_0^{(1)})\}$. Also, Eq. (H32) means that the spectrum of $W_{I\mathcal{L}_1}$, $\{-\theta_1^a(-\boldsymbol{k}_0^{(1)})\}$, is identical to that of $W_{\mathcal{L}_1}$, $\{\theta_1^a(\boldsymbol{k}_0^{(1)})\}$. Thus, $|\theta_1^a(\boldsymbol{k}_0^{(1)})\rangle$ and $|-\theta_1^{a'}(-\boldsymbol{k}_0^{(1)})\rangle$ are paired by inversion symmetry, where $|\theta_1^a(\boldsymbol{k}_0^{(1)})\rangle$ is an eigenstate of $W_{\mathcal{L}_1}$ with an eigenvalue $e^{i\theta_1^a(\boldsymbol{k}_0^{(1)})}$:

$$\left|-\theta_1^{a'}\big(-\boldsymbol{k}_0^{(1)}\big)\right\rangle = \left[B_I(\boldsymbol{k}_0^{(1)})\right]^\dagger\left|\theta_1^a(\boldsymbol{k}_0^{(1)})\right\rangle. \tag{H33}$$

This can be viewed as a unitary analogy of particle-hole symmetry. We define the sewing matrix $B_I^{(1)}(\boldsymbol{k}_0^{(1)})$ as

$$B_I^{(1)}\big(\boldsymbol{k}_0^{(1)}\big)_{ab} = \left\langle-\theta_1^a\big(-\boldsymbol{k}_0^{(1)}\big)\left|\left[B_I(\boldsymbol{k}_0^{(1)})\right]^\dagger\right|\theta_1^b(\boldsymbol{k}_0^{(1)})\right\rangle. \tag{H34}$$

Now, we define eigenstates $|u_1^a(\boldsymbol{k}_0^{(1)})\rangle$ of $\hat{W}_{\mathcal{L}_1} = |n, \boldsymbol{k}_0^{(1)}\rangle W_{\mathcal{L}_1}\langle n, \boldsymbol{k}_0^{(1)}|$ with eigenvalue $e^{i\theta_1^a(\boldsymbol{k}_0^{(1)})}$, where

$$\left|u_1^a\big(\boldsymbol{k}_0^{(1)}\big)\right\rangle = \sum_{n=1}^{n_{\text{occ}}}\left|\theta_1^a(\boldsymbol{k}_0^{(1)})\right\rangle_n\left|n, \boldsymbol{k}_0^{(1)}\right\rangle. \tag{H35}$$

5. Nested Wilson loop

When the Wilson bands are gapped, a nested Wilson loop can be defined [36,37]. We first choose an inversion-symmetric subset of the Wilson bands by defining a projector $\tilde{P}^{(1)}$ preserving inversion symmetry as shown in Fig. 16. The Wilson bands $|\theta_1^a(\boldsymbol{k}_0^{(1)})\rangle$ selected by $\tilde{P}^{(1)}$ are labeled by $a = 1, \ldots, n_{\tilde{P}^{(1)}}$. To define the nested Wilson

loop, we choose the loop $\mathcal{L}_2$ along the k_2 direction: $\mathcal{L}_2 : (k_{1,0}, k_{2,0}, k_3) \rightarrow (k_{1,0}, k_{2,0} + 2\pi, k_3)$. In terms of the Berry connection $[a_i^{(1)}(\boldsymbol{k})]_{ab}$,

$$\left[a_i^{(1)}(\boldsymbol{k})\right]_{ab} = \langle u_1^a(\boldsymbol{k})| \, i\boldsymbol{\nabla}_i \, |u_1^b(\boldsymbol{k})\rangle, \tag{H36}$$

the nested Wilson loop is defined by

$$\left[W_{\mathcal{L}_2}^{(1)}\right]_{ab} = \left[P \, e^{i \int_{\mathcal{L}_2} dk^i a_i^{(1)}(\boldsymbol{k})}\right]_{ab}. \tag{H37}$$

Repeating the derivation of the symmetry transformation of the Wilson loop, we obtain

$$W_{I\mathcal{L}_2}^{(1)} = \left[B_I^{(1)}(\boldsymbol{k}_0^{(2)})\right]^\dagger W_{\mathcal{L}_2}^{(1)} B_I^{(1)}(\boldsymbol{k}_0^{(2)}), \tag{H38}$$

where $\boldsymbol{k}_0^{(2)} = (k_{1,0}, k_{2,0}, k_3)$. Thus, $|\theta_{2\leftarrow 1}^A(\boldsymbol{k}_0^{(2)})\rangle$ and $|-\theta_{2\leftarrow 1}^{A'}(-\boldsymbol{k}_0^{(2)})\rangle$ are paired by inversion symmetry where $|\theta_{2\leftarrow 1}^A(\boldsymbol{k}_0^{(2)})\rangle$ is eigenstate of $W_{\mathcal{L}_2}^{(1)}$ with eigenvalue $e^{i\theta_{2\leftarrow 1}^A(\boldsymbol{k}_0^{(2)})}$:

$$\left|-\theta_{2\leftarrow 1}^{A'}\left(-\boldsymbol{k}_0^{(2)}\right)\right\rangle = \left[B_I^{(2)}(\boldsymbol{k}_0^{(2)})\right]^\dagger |\theta_{2\leftarrow 1}^A(\boldsymbol{k}_0^{(2)})\rangle. \tag{H39}$$

Thus, sewing matrix is defined as

$$B_I^{(2)}(\boldsymbol{k}_0^{(2)})_{AB} = \langle -\theta_{2\leftarrow 1}^A(-\boldsymbol{k}_0^{(2)})|\left[B_I^{(1)}(\boldsymbol{k}_0^{(2)})\right]^\dagger|\theta_{2\leftarrow 1}^B(\boldsymbol{k}_0^{(2)})\rangle. \tag{H40}$$

As for the nested Wilson loop, we define eigenstates $|u_{2\leftarrow 1}^A(\boldsymbol{k}_0^{(2)})\rangle$ of $\hat{W}_{\mathcal{L}_2}^{(1)} = |n, \boldsymbol{k}_0^{(2)}\rangle W_{\mathcal{L}_2}^{(1)} \langle n, \boldsymbol{k}_0^{(2)}|$ with eigenvalue $e^{i\theta_{2\leftarrow 1}^A(\boldsymbol{k}_0^{(2)})}$, where

$$\left|u_{2\leftarrow 1}^A(\boldsymbol{k}_0^{(2)})\right\rangle = \sum_{n=1}^{n_{\text{occ}}} \sum_{a=1}^{n_{\tilde{P}^{(1)}}} \left|\theta_{2\leftarrow 1}^A(\boldsymbol{k}_0^{(2)})\right\rangle_a \left|\theta_1^a(\boldsymbol{k}_0^{(1)})\right\rangle_n |n, \boldsymbol{k}_0^{(2)}\rangle. \tag{H41}$$

When the nested Wilson bands are gapped, the doubly nested Wilson loop can be defined after we project the nested Wilson bands with an inversion-symmetric projector $\tilde{P}^{(2)}$. The nested Wilson bands $|\theta_{2\leftarrow 1}^A(\boldsymbol{k}_0^{(2)})\rangle$ selected by $\tilde{P}^{(2)}$ are labeled by $A = 1, \ldots, n_{\tilde{P}^{(2)}}$. For the doubly nested Wilson loop, the loop $\mathcal{L}_3$ is chosen to be k_3-directed line $\mathcal{L}_3 : (k_{1,0}, k_{2,0}, k_{3,0}) \rightarrow (k_{1,0}, k_{2,0}, k_{3,0} + 2\pi)$. If we define a Berry connection $[a_i^{(2)}(\boldsymbol{k}_0^{(2)})]_{AB}$,

$$\left[a_i^{(2)}(\boldsymbol{k}_0^{(2)})\right]_{AB} = \langle u_{2\leftarrow 1}^A(\boldsymbol{k}_0^{(2)})| \, i\boldsymbol{\nabla}_i \, |u_{2\leftarrow 1}^B(\boldsymbol{k}_0^{(2)})\rangle, \tag{H42}$$

the doubly nested Wilson loop can be defined by

$$\left[W_{\mathcal{L}_3}^{(2)}\right]_{AB} = \left[P \, e^{i \int_{\mathcal{L}_3} dk^i a_i^{(2)}(\boldsymbol{k}^{(2)})}\right]_{AB}. \tag{H43}$$

Repeating this procedure, the lth nested Wilson loop $W_{\mathcal{L}}^{(l)}$ can be defined for an integer.

6. Mapping between inversion parities and Wilson loop spectrum

Here, we review the mapping between parity configuration of the occupied states and the Wilson loop spectrum. We recommend to refer [66] for the comprehensive study of the mapping. The mapping takes two steps.

a. Step 1. Mapping from parity configuration to Wilson loop spectrum. Without loss of generality, we can focus on the (k_1, k_2) plane in dD Brillouin zone. In this plane, inversion symmetry in two dimensions, $(k_1, k_2) \rightarrow (-k_1, -k_2)$, is induced by inversion symmetry in d dimensions. Then,

we can define the number of occupied states at $(\bar{k}_1, \bar{k}_2) = -(\bar{k}_1, \bar{k}_2)$ with parity ξ, $n_\xi(\bar{k}_1, \bar{k}_2)$. At $\bar{k}_2 = 0$ or π, one can define the fewest number $n_s(\bar{k}_2)$ among $\{n_\xi(0, \bar{k}_2), n_\xi(\pi, \bar{k}_2)\}$. When $n_s(k_s) = n_{\xi_s}(k_s, \bar{k}_2)$, the mapping from $\{n_\xi(\bar{k}_1, \bar{k}_2)\}$ to the Wilson loop spectrum $\{\theta_1(\bar{k}_2)\}$ is given by the following rules:

$$n_{\frac{\pi}{2}(1+\xi_s)}^W(\bar{k}_2) = n_+(k_s + \pi, \bar{k}_2) - n_s(\bar{k}_2),$$
$$n_{\frac{\pi}{2}(1-\xi_s)}^W(\bar{k}_2) = n_-(k_s + \pi, \bar{k}_2) - n_s(\bar{k}_2), \tag{H44}$$
$$n_c^W(\bar{k}_2) = 2n_s(\bar{k}_2),$$

where $n_0^W(\bar{k}_2)$, $n_\pi^W(\bar{k}_2)$, and $n_c^W(\bar{k}_2)$ are the number of Wilson loop spectrum $\{\theta_1(\bar{k}_2)\}$ with eigenvalues $\theta_1(\bar{k}_2) = 0$, π, and $(-\theta_0, \theta_0)$, respectively. Here, we denote θ_0 as a generic value not equal to 0 or π.

b. Step 2. Mapping from Wilson loop spectrum to relative winding number. With $\{n_\theta^W(\bar{k}_2)\} = (n_{\xi_s}^W(\bar{k}_2), n_{-\xi_s}^W(\bar{k}_2), n_c^W(\bar{k}_2))$ for a given Wilson loop spectrum, N_d is defined as

$$N_d = \max\left(n_\pi^W(0) - n_\pi^W(\pi) - n_c^W(\pi),\right.$$
$$\left. n_\pi^W(\pi) - n_\pi^W(0) - n_c^W(0)\right). \tag{H45}$$

When $|C| < N_d$ where C is the Chern number defined in the (k_1, k_2) plane, N_d is given by $N_d = 2N_W + |C|$. If $|C| \geqslant N_d$, the relative winding number N_W is zero. Also note that the Chern number C and N_d satisfies

$$C = N_d = n_\pi^W(\pi) - n_\pi^W(0) \pmod 2. \tag{H46}$$

Since a nonzero Chern number implies the stable band topology, let us assume that $C = 0$. Then, the Wilson loop is unwound if $N_d \leqslant 0$. Otherwise, $N_d > 0$, the relative winding number N_W is given by $N_W = \frac{1}{2}N_d$.

APPENDIX I: CHARACTERIZATION OF FRAGILE BAND TOPOLOGY IN THE NESTED WILSON LOOP SPECTRUM

In this Appendix, we provide the proof for the claim that the nested Wilson loop spectrum characterized by a positive even integer $N_{d,\text{nest}}$, which is defined as

$$N_{d,\text{nest}} = \max\left(n_\pi^{W_\text{nest}}(0) - n_\pi^{W_\text{nest}}(\pi) - n_c^{W_\text{nest}}(\pi),\right.$$
$$\left. n_\pi^{W_\text{nest}}(\pi) - n_\pi^{W_\text{nest}}(0) - n_c^{W_\text{nest}}(0)\right) \tag{I1}$$

implies the fragile band topology. Here, $n_\pi^{W_\text{nest}}(\bar{k}_3)$ and $n_c^{W_\text{nest}}(\bar{k}_3)$ are the number of eigenvalues $\theta_{2\leftarrow 1}(\bar{k}_3)$, which is equal to π and takes a generic value, respectively, in the nested Wilson loop spectrum at $\bar{k}_3 = 0$ and π.

Before proving the claim, we note that the nested Wilson loop spectrum satisfies similar relations discussed in Appendix H 6 since the Wilson loop and the nested Wilson loop spectra are constrained by the inversion symmetry in the same way. First, we can assign an inversion parity to each Wilson loop eigenstate at inversion-invariant momenta $\boldsymbol{k}^\text{inv}$. At $\boldsymbol{k}^\text{inv}$, $|\theta_1(\boldsymbol{k}^\text{inv})\rangle$ is an inversion eigenstate with definite parity when $\theta_1(\boldsymbol{k}^\text{inv}) = 0$ and π. On the other hand, $|\theta_1(\boldsymbol{k}^\text{inv})\rangle$ and $|-\theta_1(\boldsymbol{k}^\text{inv})\rangle$ are paired by inversion symmetry when $\theta_1(\boldsymbol{k}^\text{inv})$ is a generic value. This pair forms inversion eigenstates with even and odd parities. The parities of the Wilson loop eigenstates at $\boldsymbol{k}^\text{inv}$ are encoded in the sewing matrix $B_I^{(1)}(\boldsymbol{k}^\text{inv})$ in Eq. (H34). By repeating step 1 in Appendix H 6, we obtain an
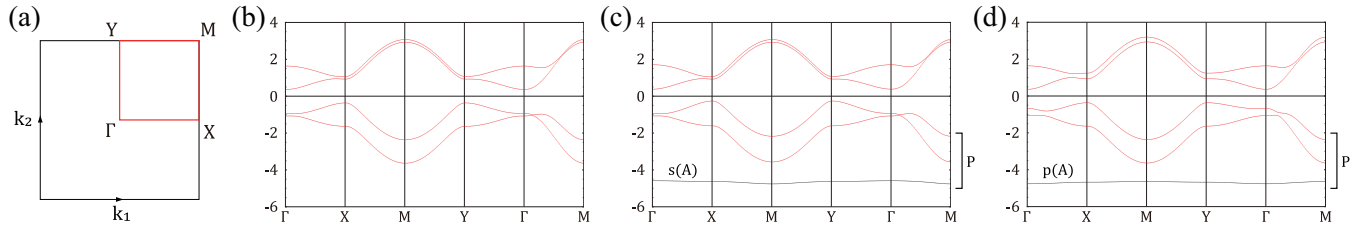
FIG. 17. Band structure of the tight-binding model in Eq. (J1). (a) 2D Brillouin zone. High-symmetry lines are shown as red lines. (b) Energy bands along the high-symmetry lines. (c) Energy bands after adding a $s(A)$ orbital. (d) Energy bands after adding a $p(A)$ orbital.

eigenvalue configuration in the nested Wilson loop spectrum $\{n_\theta^{W_{\text{nest}}}(\bar{k}_3)\} = (n_0^{W_{\text{nest}}}(\bar{k}_3), n_\pi^{W_{\text{nest}}}(\bar{k}_3), n_c^{W_{\text{nest}}}(\bar{k}_3))$ at $\bar{k}_3 = 0$ and π. This configuration uniquely determines $N_{d,\text{nest}}$ in Eq. (I1). Second, the nested Chern number C_{nest}, the nested relative winding number $N_{W,\text{nest}}$ and $N_{d,\text{nest}}$ satisfy relations similar to ones for the Chern number C, the relative winding number N_W and N_d presented in step 2 in Appendix H 6.

We begin our proof by showing that a band crossing between the Wilson bands does not change $N_{d,\text{nest}}$ while it changes the nested Chern number C_{nest} only by an even integer. When a gap closing and reopening in the Wilson loop spectrum happens at a generic momentum, it does not change the parity configuration of the Wilson loop eigenstates. As the parity configuration determines an eigenvalue configuration in the nested Wilson loop spectrum, $N_{d,\text{nest}}$ is invariant. If the Wilson bands are inverted at an inversion-invariant momentum $\boldsymbol{k}^{\text{inv}}$, only pairs of Wilson bands $|\theta_1(\boldsymbol{k}^{\text{inv}})\rangle$ and $|-\theta_1(\boldsymbol{k}^{\text{inv}})\rangle$ are involved in the Wilson band inversion. Thus, there is no net exchange of inversion parities, and $N_{d,\text{nest}}$ is invariant. Consequently, the Wilson band crossing does not change $N_{d,\text{nest}}$. On the other hand, the Wilson band crossing can change C_{nest} by an even integer since it always happens pairwise due to inversion symmetry [20].

For an integer valued $N_{d,\text{nest}}$, there are three cases to be considered: $N_{d,\text{nest}}$ is equal to (i) an odd integer, (ii) a positive even integer, and (iii) a negative even integer or 0.

(i) When $N_{d,\text{nest}}$ is an odd integer, Eq. (H46) implies that C_{nest} is also an odd integer. Since a Wilson band crossing cannot change an odd C_{nest} to zero, the nested Wilson loop spectrum indicates the stable band topology.

(ii) When $N_{d,\text{nest}}$ is a positive even integer, Eq. (H46) implies that C_{nest} is also an even integer. For even C_{nest}, a Wilson band crossing can change C_{nest} to zero. However, the nested Wilson loop spectrum cannot be gapped and it shows the relative winding since $N_{d,\text{nest}} = 2N_{W,\text{nest}} + |C_{\text{nest}}|$ holds when $|C_{\text{nest}}| < N_{d,\text{nest}}$.

(iii) When $N_{d,\text{nest}}$ is a negative even integer or zero, the nested relative winding number $N_{W,\text{nest}}$ is always zero. This is because the relative winding exists only when $|C_{\text{nest}}| < N_{d,\text{nest}}$. Thus, the nested Wilson loop spectrum can be gapped when a Wilson band crossing happens.

APPENDIX J: NUMERICAL DETAILS OF THE WILSON LOOP CALCULATION

In this Appendix, we summarized the numerical details in Sec. VI.

1. 2D third-order TI

The tight-binding Hamiltonian of 2D third-order TI is given by

$$H_{A(2,3)}(\boldsymbol{k}) = \sum_{i=1}^{2} \sin k_i \Gamma_i - \left(2 - \lambda - \sum_{i=1}^{2} \cos k_i\right)\Gamma_5$$
$$+ i\sum_{i=1}^{2}\sum_{a=3}^{4} \Delta_{i,a} \Gamma_i \Gamma_a \Gamma_5, \tag{J1}$$

where $\{\Gamma_1, \ldots, \Gamma_5\} = \{\tau_x\sigma_x, \tau_x\sigma_y, \tau_x\sigma_z, \tau_y\sigma_0, \tau_z\sigma_0\}$ and $\Gamma_5 = -\Gamma_1 \ldots \Gamma_4$. For numerical calculations, $\Delta_{1,3} = 0.240$, $\Delta_{1,4} = -0.196$, $\Delta_{2,3} = -0.259$, and $\Delta_{2,4} = -0.204$ are used. $H_{A(2,3)}(\boldsymbol{k})$ is inversion symmetric, i.e., $I_0 H_{A(2,3)}(\boldsymbol{k}) I_0^{-1} = H_{A(2,3)}(-\boldsymbol{k})$, with inversion-symmetry operator I_0:

$$I_0 = \tau_z\sigma_0 = \begin{pmatrix} \mathbb{1}_2 & \\ & -\mathbb{1}_2 \end{pmatrix}. \tag{J2}$$

The energy bands of $H_{A(2,3)}(\boldsymbol{k})$ are shown in Fig. 17(b).

a. 2D third-order TI + s(A)

Now, we add an s orbital localized at the Wyckoff position $A = (0, 0)$. Onsite energy h_1 and an interaction Hamiltonian between the original four bands and s orbital are chosen as

$$h_1 = -4.5, \quad h_2 = 0.1 \times (4, 6, 0, 0)^T. \tag{J3}$$

Thus, the perturbation Hamiltonian H_c is given by

$$H_c = \begin{pmatrix} 0_4 & h_2 \\ h_2^T & h_1 \end{pmatrix}, \tag{J4}$$

where 0_4 denotes 4×4 null matrix.

Hence, Hamiltonian $H_{+s(A)}$ and inversion-symmetry operator I for the five bands are given by

$$H_{+s(A)} = H_{A(2,3)} + H_c, \quad I = \begin{pmatrix} I_0 & 0 \\ 0 & 1 \end{pmatrix}, \tag{J5}$$

and $I H_{+s(A)}(\boldsymbol{k}) I^{-1} = H_{+s(A)}(-\boldsymbol{k})$. The energy bands of $H_{+s(A)}(\boldsymbol{k})$ are shown in Fig. 17(c).

b. 2D third-order TI + p(A)

We add a p orbital localized at the Wyckoff position $A = (0, 0)$. Onsite energy h_1 and an interaction Hamiltonian between the original four bands and p orbital are chosen as

$$h_1 = -4.5, \quad h_2 = 0.1 \times (0, 0, 6, -8)^T. \tag{J6}$$
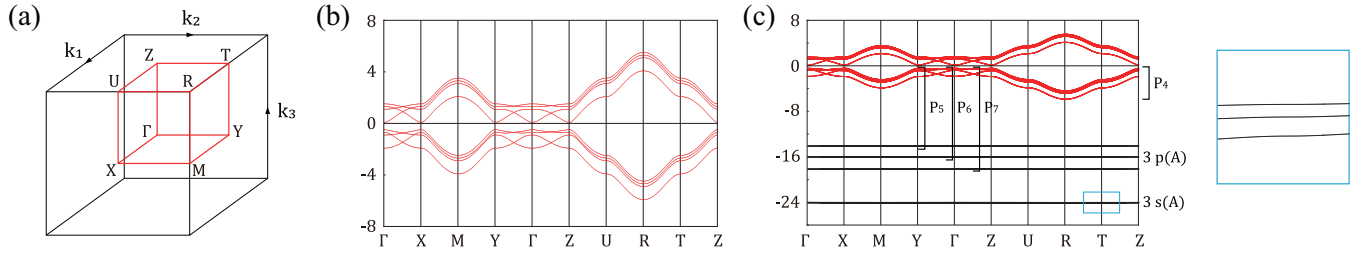
(a)

(b)

(c)

FIG. 18. Band structure of the tight-binding model in Eq. (J9). (a) 3D Brillouin zone. High-symmetry lines are shown as red lines. (b) Energy bands along the high-symmetry lines. (c) Energy bands after adding three $s(A)$ and three $p(A)$ orbitals. (c) $P_{4,5,6,7}$ denote the projector for the Wilson loop.

Thus, the perturbation Hamiltonian H_c is given by

$$H_c = \begin{pmatrix} 0_4 & h_2 \\ h_2^T & h_1 \end{pmatrix}. \tag{J7}$$

Hence, Hamiltonian $H_{+p(A)}$ and inversion-symmetry operator I for the five bands are given by

$$H_{+p(A)} = H_{A(2,3)} + H_c, \quad I = \begin{pmatrix} I_0 & 0 \\ 0 & -1 \end{pmatrix}, \tag{J8}$$

and $I H_{+p(A)}(\boldsymbol{k}) I^{-1} = H_{+p(A)}(-\boldsymbol{k})$. The energy bands of $H_{+p(A)}(\boldsymbol{k})$ are shown in Fig. 17(d).

2. 3D fourth-order TI

The tight-binding Hamiltonian of 3D fourth-order TI is given by

$$H_{A(3,4)}(\boldsymbol{k}) = \sum_{i=1}^{3} \sin k_i \check{\Gamma}_i - \left(3 - \lambda - \sum_{i=1}^{3} \cos k_i\right) \check{\Gamma}_7$$

$$+ i \sum_{i=1}^{3} \sum_{a=4}^{6} \check{\Delta}_{i,a} \check{\Gamma}_i \check{\Gamma}_a \check{\Gamma}_7. \tag{J9}$$

where $\{\check{\Gamma}_1, \dots, \check{\Gamma}_7\} = \{\mu_x \tau_x \sigma_x, \mu_x \tau_x \sigma_y, \mu_x \tau_x \sigma_z, \mu_x \tau_y \sigma_0, \mu_x \tau_z \sigma_0, \mu_y \tau_0 \sigma_0, \mu_z \tau_0 \sigma_0\}$ and $\check{\Gamma}_7 = i\check{\Gamma}_1 \dots \check{\Gamma}_6$. For numerical calculations, $\check{\Delta}_{1,4} = -0.25$, $\check{\Delta}_{1,5} = 0.05$, $\check{\Delta}_{1,6} = 0.10$, $\check{\Delta}_{2,4} = -0.05$, $\check{\Delta}_{2,5} = 0.30$, $\check{\Delta}_{2,6} = -0.10$, $\check{\Delta}_{3,4} = 0.05$, $\check{\Delta}_{3,5} = -0.05$, and $\check{\Delta}_{3,6} = 0.35$ are used. $H_{A(3,4)}(\boldsymbol{k})$ is inversion symmetric, i.e., $I_0 H_{A(3,4)}(\boldsymbol{k}) I_0^{-1} = H_{A(3,4)}(-\boldsymbol{k})$, with inversion-symmetry operator I_0:

$$I_0 = \mu_z \tau_0 \sigma_0 = \begin{pmatrix} \mathbb{1}_4 & \\ & -\mathbb{1}_4 \end{pmatrix}. \tag{J10}$$

Energy bands of $H_{A(3,4)}(\boldsymbol{k})$ are shown in Fig. 18(b).

a. 3D fourth-order TI + 3p(A)

Now, we add three p orbitals localized at the Wyckoff position $A = (0, 0, 0)$. For this, we add six orbitals at generic Wyckoff positions $\boldsymbol{x}_{9,\dots,14}$:

$$\boldsymbol{x}_9 = -\boldsymbol{x}_{10} = (-0.4, -0.4, -0.4),$$
$$\boldsymbol{x}_{11} = -\boldsymbol{x}_{12} = (-0.2, -0.2, -0.2), \tag{J11}$$
$$\boldsymbol{x}_{13} = -\boldsymbol{x}_{14} = (-0.1, 0.1, -0.1).$$

Note that the original eight orbitals are localized at $\boldsymbol{x}_{1,\dots,8} = (0, 0, 0)$. The Hamiltonian for the additional six bands is

chosen to be

$$h_1 = \begin{pmatrix} -19 & -5 & 0 & 0 & 0 & 0 \\ -5 & -19 & 0 & 0 & 0 & 0 \\ 0 & 0 & -20 & -4 & 0 & 0 \\ 0 & 0 & -4 & -20 & 0 & 0 \\ 0 & 0 & 0 & 0 & -21 & -3 \\ 0 & 0 & 0 & 0 & -3 & -21 \end{pmatrix}, \tag{J12}$$

and it is invariant under the inversion-symmetry operator I_c:

$$I_c = \begin{pmatrix} 0 & 1 & 0 & 0 & 0 & 0 \\ 1 & 0 & 0 & 0 & 0 & 0 \\ 0 & 0 & 0 & 1 & 0 & 0 \\ 0 & 0 & 1 & 0 & 0 & 0 \\ 0 & 0 & 0 & 0 & 0 & 1 \\ 0 & 0 & 0 & 0 & 1 & 0 \end{pmatrix}. \tag{J13}$$

Diagonalizing h_1 we obtain three s and three p orbitals localized at A. Three s orbitals are degenerate with an energy eigenvalue -24, and three p orbitals have energy eigenvalues -14, -16, and -18, respectively. Now, we couple the additional six bands to the original eight bands according to h_c:

$$h_2 = 0.05 \times \begin{pmatrix} 11 & 11 & -7 & -7 & -2 & -2 \\ -3 & -3 & -1 & -1 & -1 & -1 \\ -9 & -9 & -10 & -10 & 7 & 7 \\ 2 & 2 & 10 & 10 & 17 & 17 \\ -1 & 1 & -9 & 9 & 7 & -7 \\ -3 & 3 & -2 & 2 & -17 & 17 \\ -8 & 8 & 4 & -4 & -5 & 5 \\ -15 & 15 & 3 & -3 & 13 & -13 \end{pmatrix}. \tag{J14}$$

Thus, the perturbation Hamiltonian H_{c1} is given by

$$H_{c1} = \begin{pmatrix} 0_8 & h_2 \\ h_2^T & h_1 \end{pmatrix}. \tag{J15}$$

To sum up, the Hamiltonian H and inversion-symmetry operator I for the 14 bands are given by

$$H = H_{A(3,4)} + H_{c1}, \quad I = \begin{pmatrix} I_0 & 0 \\ 0 & I_c \end{pmatrix}, \tag{J16}$$

and $I H(\boldsymbol{k}) I^{-1} = H(-\boldsymbol{k})$. The energy bands of $H(\boldsymbol{k})$ are shown in Fig. 18(c). In order to study the effect of adding p orbitals, we define projectors P_5, P_6, and P_7 as the projections to the occupied states with an additional $p(A)$ orbital, additional two $p(A)$ orbitals, and additional three $p(A)$ orbitals, respectively [see Fig. 18(c) for the definition of $P_{5,6,7}$].
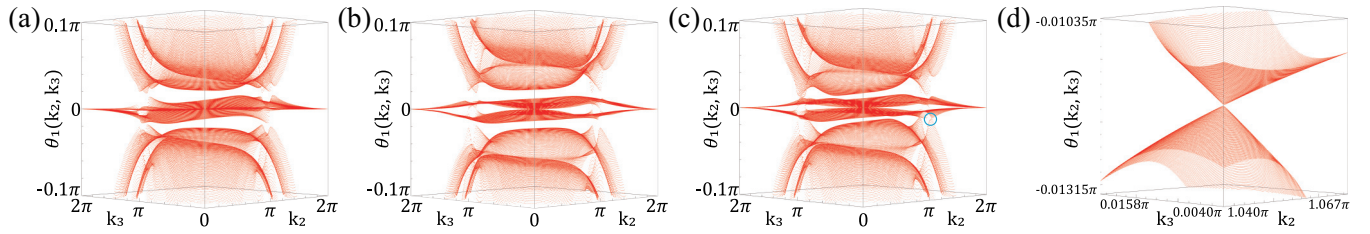
FIG. 19. Wilson bands with a projector P_6 for (a) $H_{c1} = H_c(q = 1)$. (b) $H_{c2} = H_c(q = 0)$. (c) $H_c(q = 0.49)$. The Wilson band transition occurs at $(k_2, k_3, \theta_1(k_2, k_3)) = (1.054\pi, 0.0099\pi, -0.0117\pi)$ (blue circle) and $-(1.054\pi, 0.0099\pi, -0.0117\pi)$. (d) The band crossing between Wilson bands at $(1.054\pi, 0.0099\pi, -0.0117\pi)$ [blue circle in (c)].

b. Wilson band transition

The nested Wilson loop spectrum depends on the topology of Wilson bands. Thus, a bulk-gap-preserving perturbation can change the topology of the nested Wilson loop through a band crossing between Wilson bands, which we call a Wilson band transition. To investigate how the nested Wilson loop spectrum changes after Wilson band transition systematically, we choose a new coupling Hamiltonian h_2' as

$$
h_2' = 0.05 \times \begin{pmatrix}
18 & 18 & 4 & 4 & 19 & 19 \\
-5 & -5 & -1 & -1 & 5 & 5 \\
-10 & -10 & 6 & 6 & 4 & 4 \\
6 & 6 & 15 & 15 & -4 & -4 \\
-8 & 8 & -15 & 15 & -4 & 4 \\
-9 & 9 & 3 & -3 & -1 & 1 \\
-4 & 4 & 6 & -6 & 3 & -3 \\
-2 & 2 & 4 & -4 & 5 & -5
\end{pmatrix}.
$$
(J17)

Thus, new perturbation Hamiltonian H_{c2} is given by

$$
H_{c2} = \begin{pmatrix} 0_8 & h_2' \\ (h_2')^T & h_1 \end{pmatrix}.
$$
(J18)

Now, we define an interpolating Hamiltonian $H_c(q)$ and $H(\mathbf{k}, q)$ as

$$
H_c(q) = qH_{c1} + (1 - q)H_{c2},
$$
$$
H(\mathbf{k}, q) = H_{A(3,4)} + H_c(q),
$$
(J19)

and find critical values q_c where the Wilson bands close the gap. The Wilson bands with the projector P_6 close the gap at $q_c = 0.49$ and the band-crossing points are $(k_2, k_3, \theta_1(k_2, k_3)) \simeq \pm(1.054\pi, 0.0099\pi, -0.0117\pi)$ as shown in Figs. 19(c) and 19(d). For Wilson bands with the projector P_7, the Wilson band transition occurs at $q_c = 0.52$ and the gap closes at $(k_2, k_3, \theta_1(k_2, k_3)) \simeq \pm(1.040\pi, 0.0083\pi, -0.0114\pi)$. After the Wilson band transition, the nested Chern number changes from ± 2 to 0 as shown in Fig. 13.

[1] C. L. Kane and E. J. Mele, $\mathbb{Z}_2$ Topological Order and the Quantum Spin Hall Effect, Phys. Rev. Lett. **95**, 146802 (2005).

[2] M. Z. Hasan and C. L. Kane, Colloquium: topological insulators, Rev. Mod. Phys. **82**, 3045 (2010).

[3] A. Altland and M. R. Zirnbauer, Nonstandard symmetry classes in mesoscopic normal-superconducting hybrid structures, Phys. Rev. B **55**, 1142 (1997).

[4] A. P. Schnyder, S. Ryu, A. Furusaki, and A. W. W. Ludwig, Classification of topological insulators and superconductors in three spatial dimensions, Phys. Rev. B **78**, 195125 (2008).

[5] A. Kitaev, *Periodic Table for Topological Insulators and Superconductors* (AIP, Melville, NY, 2009), pp. 22–30.

[6] S. Ryu, A. P. Schnyder, A. Furusaki, and A. W. W. Ludwig, Topological insulators and superconductors: Tenfold way and dimensional hierarchy, New J. Phys. **12**, 065010 (2010).

[7] L. Fu, Topological Crystalline Insulators, Phys. Rev. Lett. **106**, 106802 (2011).

[8] T. H. Hsieh, H. Lin, J. Liu, W. Duan, A. Bansil, and L. Fu, Topological crystalline insulators in the snte material class, Nat. Commun. **3**, 982 (2012).

[9] J. Kruthoff, J. de Boer, J. van Wezel, C. L. Kane, and R.-J. Slager, Topological Classification of Crystalline Insulators Through Band Structure Combinatorics, Phys. Rev. X **7**, 041069 (2017).

[10] B. Bradlyn, L. Elcoro, J. Cano, M. G. Vergniory, Z. Wang, C. Felser, M. I. Aroyo, and B. A. Bernevig, Topological quantum chemistry, Nature (London) **547**, 298 (2017).

[11] H. C. Po, A. Vishwanath, and H. Watanabe, Symmetry-based indicators of band topology in the 230 space groups, Nat. Commun. **8**, 50 (2017).

[12] H. Watanabe, H. C. Po, and A. Vishwanath, Structure and topology of band structures in the 1651 magnetic space groups, Sci. Adv. **4**, eaat8685 (2018).

[13] Z. Song, T. Zhang, Z. Fang, and C. Fang, Quantitative mappings between symmetry and topology in solids, Nat. Commun. **9**, 3530 (2018).

[14] R. Thorngren and D. V. Else, Gauging Spatial Symmetries and the Classification of Topological Crystalline Phases, Phys. Rev. X **8**, 011040 (2018).

[15] K. Shiozaki, M. Sato, and K. Gomi, Atiyah-Hirzebruch spectral sequence in band topology: General formalism and topological invariants for 230 space groups, arXiv:1802.06694.

[16] H. C. Po, H. Watanabe, and A. Vishwanath, Fragile Topology and Wannier Obstructions, Phys. Rev. Lett. **121**, 126402 (2018).

[17] J. Cano, B. Bradlyn, Z. Wang, L. Elcoro, M. G. Vergniory, C. Felser, M. I. Aroyo, and B. A. Bernevig, Topology of Disconnected Elementary Band Representations, Phys. Rev. Lett. **120**, 266401 (2018).

[18] B. Bradlyn, Z. Wang, J. Cano, and B. A. Bernevig, Disconnected elementary band representations, fragile topology, and wilson loops as topological indices: An example on the triangular lattice, Phys. Rev. B **99**, 045140 (2019).

[19] A. Bouhon, A. M. Black-Schaffer, and R.-J. Slager, Wilson loop approach to topological crystalline insulators with time reversal symmetry, arXiv:1804.09719.

[20] B. J. Wieder and B. A. Bernevig, The axion insulator as a pump of fragile topology, arXiv:1810.02373.

[21] H. C. Po, L. Zou, T. Senthil, and A. Vishwanath, Faithful tight-binding models and fragile topology of magic-angle bilayer graphene, Phys. Rev. B **99**, 195455 (2019).

[22] D. V. Else, H. C. Po, and H. Watanabe, Fragile topological phases in interacting systems, Phys. Rev. B **99**, 125122 (2019).

[23] J. Ahn, S. Park, and B.-J. Yang, Failure of Nielsen-Ninomiya Theorem and Fragile Topology in Two-Dimensional Systems with Space-Time Inversion Symmetry: Application to Twisted Bilayer Graphene at Magic Angle, Phys. Rev. X **9**, 021013 (2019).

[24] S. Liu, A. Vishwanath, and E. Khalaf, Shift Insulators: Rotation-Protected Two-Dimensional Topological Crystalline Insulators, Phys. Rev. X **9**, 031003 (2019).

[25] Z. Song, L. Elcoro, N. Regnault, and B. A. Bernevig, Fragile phases as affine monoids: Full classification and material examples, arXiv:1905.03262.

[26] S. H. Kooi, G. van Miert, and C. Ortix, Classification of crystalline insulators without symmetry indicators: Atomic and fragile topological phases in twofold rotation symmetric systems, Phys. Rev. B **100**, 115160 (2019).

[27] B. J. Wieder, Z. Wang, J. Cano, X. Dai, L. M. Schoop, B. Bradlyn, and B. A. Bernevig, Strong and "fragile" topological Dirac semimetals with higher-order fermi arcs, arXiv:1908.00016.

[28] T. Thonhauser and D. Vanderbilt, Insulator/Chern-insulator transition in the Haldane model, Phys. Rev. B **74**, 235111 (2006).

[29] A. A. Soluyanov and D. Vanderbilt, Wannier representation of $\mathbf{Z}_2$ topological insulators, Phys. Rev. B **83**, 035108 (2011).

[30] N. Marzari, A. A. Mostofi, J. R. Yates, I. Souza, and D. Vanderbilt, Maximally localized Wannier functions: Theory and applications, Rev. Mod. Phys. **84**, 1419 (2012).

[31] D. S. Freed and G. W. Moore, *Twisted Equivariant Matter* (Springer, Switzerland, 2013), pp. 1927–2023.

[32] K. Shiozaki and M. Sato, Topology of crystalline insulators and superconductors, Phys. Rev. B **90**, 165114 (2014).

[33] K. Shiozaki, M. Sato, and K. Gomi, Topology of nonsymmorphic crystalline insulators and superconductors, Phys. Rev. B **93**, 195413 (2016).

[34] K. Shiozaki, M. Sato, and K. Gomi, Topological crystalline materials: General formulation, module structure, and wallpaper groups, Phys. Rev. B **95**, 235425 (2017).

[35] L. Stehouwer, J. de Boer, J. Kruthoff, and H. Posthuma, Classification of crystalline topological insulators through K-theory, arXiv:1811.02592.

[36] W. A. Benalcazar, B. A. Bernevig, and T. L. Hughes, Quantized electric multipole insulators, Science **357**, 61 (2017).

[37] W. A. Benalcazar, B. A. Bernevig, and T. L. Hughes, Electric multipole moments, topological multipole moment pumping, and chiral hinge states in crystalline insulators, Phys. Rev. B **96**, 245115 (2017).

[38] F. Schindler, A. M. Cook, M. G. Vergniory, Z. Wang, S. S. P. Parkin, B. A. Bernevig, and T. Neupert, Higher-order topological insulators, Sci. Adv. **4**, eaat0346 (2018).

[39] J. Langbehn, Y. Peng, L. Trifunovic, F. von Oppen, and P. W. Brouwer, Reflection-Symmetric Second-Order Topological Insulators and Superconductors, Phys. Rev. Lett. **119**, 246401 (2017).

[40] Z. Song, Z. Fang, and C. Fang, $(d − 2)$-Dimensional Edge States of Rotation Symmetry Protected Topological States, Phys. Rev. Lett. **119**, 246402 (2017).

[41] C. Fang and L. Fu, Rotation anomaly and topological crystalline insulators, arXiv:1709.01929.

[42] M. Ezawa, Higher-Order Topological Insulators and Semimetals on the Breathing Kagome and Pyrochlore Lattices, Phys. Rev. Lett. **120**, 026801 (2018).

[43] E. Khalaf, H. C. Po, A. Vishwanath, and H. Watanabe, Symmetry Indicators and Anomalous Surface States of Topological Crystalline Insulators, Phys. Rev. X **8**, 031070 (2018).

[44] E. Khalaf, Higher-order topological insulators and superconductors protected by inversion symmetry, Phys. Rev. B **97**, 205136 (2018).

[45] G. van Miert and C. Ortix, Higher-order topological insulators protected by inversion and rotoinversion symmetries, Phys. Rev. B **98**, 081110(R) (2018).

[46] M. Geier, L. Trifunovic, M. Hoskam, and P. W. Brouwer, Second-order topological insulators and superconductors with an order-two crystalline symmetry, Phys. Rev. B **97**, 205135 (2018).

[47] A. Matsugatani and H. Watanabe, Connecting higher-order topological insulators to lower-dimensional topological insulators, Phys. Rev. B **98**, 205129 (2018).

[48] Z. Wang, B. J. Wieder, J. Li, B. Yan, and B. A. Bernevig, Higher-Order Topology, Monopole Nodal Lines, and the Origin of Large Fermi Arcs in Transition Metal Dichalcogenides XTe$_2$ ($X =$ Mo, W), Phys. Rev. Lett. **123**, 186401 (2019).

[49] F. Schindler, Z. Wang, M. G. Vergniory, A. M. Cook, A. Murani, S. Sengupta, A. Y. Kasumov, R. Deblock, S. Jeon, I. Drozdov, H. Bouchiat, S. Guéron, A. Yazdani, B. A Bernevig, and T. Neupert, Higher-order topology in bismuth, Nat. Phys. **14**, 918 (2018).

[50] J. Ahn and B.-J. Yang, Symmetry representation approach to topological invariants in $C_{2z}T$-symmetric systems, Phys. Rev. B **99**, 235125 (2019).

[51] D. Călugăru, V. Juričić, and B. Roy, Higher-order topological phases: A general principle of construction, Phys. Rev. B **99**, 041301(R) (2019).

[52] L. Trifunovic and P. W. Brouwer, Higher-Order Bulk-Boundary Correspondence for Topological Crystalline Phases, Phys. Rev. X **9**, 011012 (2019).

[53] F. Liu and K. Wakabayashi, Novel Topological Phase with A Zero Berry Curvature, Phys. Rev. Lett. **118**, 076803 (2017).

[54] F. Liu, H.-Y. Deng, and K. Wakabayashi, Helical Topological Edge States in A Quadrupole Phase, Phys. Rev. Lett. **122**, 086804 (2019).

[55] E. Cornfeld and A. Chapman, Classification of crystalline topological insulators and superconductors with point group symmetries, Phys. Rev. B **99**, 075105 (2019).

[56] Z. Song, S.-J. Huang, Y. Qi, C. Fang, and M. Hermele, Topological states from topological crystals, arXiv:1810.02330.

[57] N. Okuma, M. Sato, and K. Shiozaki, Topological classification under nonmagnetic and magnetic point group symmetry: Application of real-space Atiyah-Hirzebruch spectral sequence to higher-order topology, Phys. Rev. B **99**, 085127 (2019).

[58] K. Shiozaki, C. Z. Xiong, and K. Gomi, Generalized homology and Atiyah-Hirzebruch spectral sequence in crystalline symmetry protected topological phenomena, arXiv:1810.00801.

[59] K. Shiozaki, The classification of surface states of topological insulators and superconductors with magnetic point group symmetry, arXiv:1907.09354.

[60] W. A. Benalcazar, T. Li, and T. L. Hughes, Quantization of fractional corner charge in C_n-symmetric higher-order topological crystalline insulators, Phys. Rev. B **99**, 245151 (2019).

[61] F. Schindler, M. Brzezińska, W. A. Benalcazar, M. Iraola, A. Bouhon, S. S. Tsirkin, M. G. Vergniory, and T. Neupert, Fractional corner charges in spin-orbit coupled crystals, Phys. Rev. Research **1**, 033074 (2019).

[62] J. Goldstone and F. Wilczek, Fractional Quantum Numbers on Solitons, Phys. Rev. Lett. **47**, 986 (1981).

[63] H. Song, S.-J. Huang, L. Fu, and M. Hermele, Topological Phases Protected by Point Group Symmetry, Phys. Rev. X **7**, 011020 (2017).

[64] S.-J. Huang, H. Song, Y.-P. Huang, and M. Hermele, Building crystalline topological phases from lower-dimensional states, Phys. Rev. B **96**, 205106 (2017).

[65] R. Yu, X. L. Qi, A. Bernevig, Z. Fang, and X. Dai, Equivalent expression of $\mathbb{Z}_2$ topological invariant for band insulators using the non-Abelian berry connection, Phys. Rev. B **84**, 075119 (2011).

[66] A. Alexandradinata, X. Dai, and B. A. Bernevig, Wilson-loop characterization of inversion-symmetric topological insulators, Phys. Rev. B **89**, 155114 (2014).

[67] A. Alexandradinata, Z. Wang, and B. A. Bernevig, Topological Insulators from Group Cohomology, Phys. Rev. X **6**, 021008 (2016).

[68] N. Read, Compactly supported Wannier functions and algebraic K-theory, Phys. Rev. B **95**, 115309 (2017).

[69] A. Alexandradinata *et al.*, Crystallographic splitting theorem for band representationsand fragile topological photonic crystals, arXiv:1908.08541

[70] W. P. Su, J. R. Schrieffer, and A. J. Heeger, Solitons in Polyacetylene, Phys. Rev. Lett. **42**, 1698 (1979).

[71] E. Outerelo *et al.*, *Mapping Degree Theory*, Vol. 108 (American Mathematical Society, Providence, RI, 2009).

[72] A. G. Abanov and P. B. Wiegmann, Theta-terms in nonlinear sigma-models, Nucl. Phys. B **570**, 685 (2000).

[73] C. Chamon, C.-Y. Hou, R. Jackiw, C. Mudry, S.-Y. Pi, and G. Semenoff, Electron fractionalization for two-dimensional Dirac fermions, Phys. Rev. B **77**, 235431 (2008).

[74] C. Chamon, C.-Y. Hou, R. Jackiw, C. Mudry, S.-Y. Pi, and A. P. Schnyder, Irrational Versus Rational Charge and Statistics in Two-Dimensional Quantum Systems, Phys. Rev. Lett. **100**, 110405 (2008).

[75] S. Ryu, C. Mudry, C.-Y. Hou, and C. Chamon, Masses in graphenelike two-dimensional electronic systems: Topological defects in order parameters and their fractional exchange statistics, Phys. Rev. B **80**, 205319 (2009).

[76] H. Yao and D.-H. Lee, Topological insulators and topological nonlinear σ models, Phys. Rev. B **82**, 245117 (2010).

[77] T. Fukui, Dirac fermion model associated with a second-order topological insulator, Phys. Rev. B **99**, 165129 (2019).

[78] C. Fang, M. J. Gilbert, and B. A. Bernevig, Bulk topological invariants in noninteracting point group symmetric insulators, Phys. Rev. B **86**, 115112 (2012).

[79] A. M. Turner, Y. Zhang, R. S. K. Mong, and A. Vishwanath, Quantized response and topology of magnetic insulators with inversion symmetry, Phys. Rev. B **85**, 165120 (2012).

[80] T. L. Hughes, E. Prodan, and B. A. Bernevig, Inversion-symmetric topological insulators, Phys. Rev. B **83**, 245132 (2011).

[81] A. Alexandradinata and J. Höller, No-go theorem for topological insulators and high-throughput identification of Chern insulators, Phys. Rev. B **98**, 184305 (2018).

[82] L. Fidkowski, T. S. Jackson, and I. Klich, Model Characterization of Gapless Edge Modes of Topological Insulators Using Intermediate Brillouin-Zone Functions, Phys. Rev. Lett. **107**, 036601 (2011).

[83] T. Morimoto and A. Furusaki, Weyl and Dirac semimetals with $\mathbb{Z}_2$ topological charge, Phys. Rev. B **89**, 235127 (2014).

[84] C. Fang, Y. Chen, H.-Y. Kee, and L. Fu, Topological nodal line semimetals with and without spin-orbital coupling, Phys. Rev. B **92**, 081201(R) (2015).

[85] Y. X. Zhao, A. P. Schnyder, and Z. D. Wang, Unified Theory of PT and CP Invariant Topological Metals and Nodal Superconductors, Phys. Rev. Lett. **116**, 156402 (2016).

[86] Y. X. Zhao and Y. Lu, PT-Symmetric Real Dirac Fermions and Semimetals, Phys. Rev. Lett. **118**, 056401 (2017).

[87] T. Bzdušek and M. Sigrist, Robust doubly charged nodal lines and nodal surfaces in centrosymmetric systems, Phys. Rev. B **96**, 155105 (2017).

[88] Z. Song, T. Zhang, and C. Fang, Diagnosis for Nonmagnetic Topological Semimetals in the Absence of Spin-Orbital Coupling, Phys. Rev. X **8**, 031069 (2018).

[89] J. Ahn, D. Kim, Y. Kim, and B.-J. Yang, Band Topology and Linking Structure of Nodal Line Semimetals with $\mathbb{Z}_2$ Monopole Charges, Phys. Rev. Lett. **121**, 106403 (2018).

[90] L. Trifunovic, S. Ono, and H. Watanabe, Geometric orbital magnetization in adiabatic processes, Phys. Rev. B **100**, 054408 (2019).

[91] E. Lee, A. Furusaki, and B.-J. Yang, Fractional charge bound to a vortex in two dimensional topological crystalline insulators, arXiv:1903.02737.

[92] L. Fu and C. L. Kane, Topological insulators with inversion symmetry, Phys. Rev. B **76**, 045302 (2007).

[93] S. Midorikawa, Fractional fermion number and its thermal effect, Phys. Rev. D **31**, 1499 (1985).